Universidade de Aveiro Departamento de Física,
2018

Nuno Gonçalo
Ferreira Cordeiro

Estudo numérico e observacional de processos da circulação na Margem Ibérica Noroeste

Numerical and observational processes study of Northwestern Iberian margin circulation

Nuno Gonçalo
Ferreira Cordeiro

Estudo numérico e observacional de processos da circulação na Margem Ibérica Noroeste

Numerical and observational processes study of Northwestern Iberian margin circulation

Dissertação apresentada à Universidade de Aveiro para cumprimento dos requisitos necessários à obtenção do grau de Doutor em Ciência, Tecnologia e Gestão do Mar, realizada sob a orientação científica do Doutor Jesús Dubert, Professor Auxiliar do Departamento de Física da Universidade de Aveiro, do Doutor Eric Desmond Barton, Profesor de Investigación do Instituto de Investigaciones Marinas, e da Doutora Rita Nolasco, Investigadora do Departamento de Física da Universidade de Aveiro

Apoio financeiro da Fundação para a Ciência e Tecnologia (FCT) através da bolsa de doutoramento SFRH/BD/101070/2014, no âmbito do Quadro de Referência Estratégico Nacional (QREN) e do Programa Operacional de Potêncial Humano (POPH), comparticipado pelo Fundo Europeu e por fundos nacionais do Ministério da Ciência, Tecnologia e Ensino Superior (MCTES). Este trabalho foi realizado no âmbito do projecto "Canaries-Iberian Marine Ecosystem Exchanges (CAIBEX)" (CTM2007-66408-C02-01/MAR, Ministerio de Educación y Ciencia) e é uma contribuição para o projectos IMPROVE (PTDC/MAR/110796/2009) financiado pela FCT; HABwave (LISBOA-01-0145-FEDER-031265) financiado pela FCT/MEC através de fundos nacionais e co-financiado pelo Fundo Europeu de Desenvolvimento Regional FEDER, dentro do acordo de parceria PT2020 e Compete 2020; e MarRISK (0262_MARRISK_1_E), cofinanciado pelo FEDER no âmbito do programa Interreg V-A Espanha - Portugal (POCTEP).

Tens potêncial, aproveita-o!

Mário Talaia, 2006

o júri / the jury

presidente / president	**Prof. Doutor Vitor Brás de Sequeira Amaral** Professor Catedrático da Universidade de Aveiro
vogais / examiners committee	**Prof. Doutor Gabriel Rosón Porto** Professor Catedrático da Universidade de Vigo
	Prof. Doutor Paulo José Relvas de Almeida Professor Auxiliar da Universidade do Algarve
	Prof. Doutor João Miguel Sequeira Silva Dias Professor Associado com Agregação da Universidade de Aveiro
	Prof. Doutor Jesús Manuel Pedreira Dubert Professor Auxiliar da Universidade de Aveiro (Orientador)

acknowledgements

Thanks are due to the many people who supported me through the long years of my PhD studentship.

First and foremost, I owe my supervisors a special acknowledgment. I don't know if they were expecting this kind of result, but from the first moment to today I was pessimistic and demoralized with my work, and they always had a word to lift me up and put me back on track. Thank you Jesus Dubert for believing in me and for patiently guiding me, Rita Nolasco for all the support and Des Barton for his joyfull welcome in the Vigo stays and insightfull contributions.

Thanks are due to Tiago Luna and Alfredo Rocha from the Group of Climatology and Meteorology of Aveiro University for providing the WRF data, which was critical for the elaboration of this thesis.

Thanks are also due to Puertos del Estado, Spain, for the Silleiro buoy data, to Confederación hidrográfica Miño-Sil for the river Minho Flow data and to CMEMS and IBI-MFC for providing the data used as boundary and initial conditions.

To all my colleagues in University of Aveiro, in particular to Krzystoff Pilsinsky with whom I've become great friends.

To my friends and family for helping me realize that a fulfilled life can be achieved without thinking about the PhD.

Palavras-chave Margem Oeste Ibérica, afloramento costeiro, plataforma continental, modelação oceânica regional, ROMS-AGRIF, dinâmica costeira, hidrografia, mesoescala, variabilidade sazonal.

Resumo

A Margem Ibérica Ocidental (WIM) caracteriza-se pelo afloramento durante o verão e convergência no inverno, alternando entre estas condições em curtas escalas temporais ao longo do ano. Durante o verão, com afloramento, podem-se desenvolver focos de correntes na direção ao largo que dão lugar a filamentos longos e estreitos que se estendem para longe da costa. Esta tese tem como objetivo o estudo da hidrografia e circulação na WIM, através do processamento de dados observacionais *in situ* e de detecção remota, e do desenvolvimento de configurações regionais de modelação a alta resolução, com o sistema ROMS-AGRIF. Três abordagens distintas foram levadas a cabo para avaliar processos a diferentes escalas espaciais e temporais: (1) Análise do campo de filamentos de mesoescala no verão de 2001 a 2010 na WIM, utilizando a temperatura de superfície do mar a partir de imagens de satélite e de modelação oceânica; (2) A resposta do oceano na plataforma continental aos ciclos de *upwelling* e *downwelling* através de uma campanha oceanográfica na região Noroeste da Península Ibérica em julho de 2009; (3) A circulação e a hidrografia na plataforma continental durante um ciclo anual (novembro 2008-dezembro 2009) através de campanhas mensais e de uma configuração regional de alta resolução.

Os filamentos encontraram-se geralmente ancorados às principais protuberâncias batimétricas e costeiras, mas onde a linha de costa é mais retilínea na região norte da WIM, as suas localizações foram mais variáveis. Observou-se uma clara relação entre a intensidade de ventos favoráveis ao afloramento e o número e comprimento dos filamentos a sul, sendo esta menos clara a norte. Foi também encontrada uma relação entre os filamentos e vórtices de mesoescala em períodos de ventos fracos. A norte, ao longo da costa mais retilínea, em julho de 2009 sob ventos de norte, um centro de afloramento estendeu-se desde o cabo Silleiro até ao Porto onde a temperatura era inferior à região circundante. Resultante do relaxamento dos ventos de norte, desenvolveu-se uma corrente em direção ao polo na plataforma interna com advecção de águas mais quentes com origem a sul do centro de afloramento. O estudo do ciclo anual, realizado no período de novembro 2008 a dezembro 2009 na região do cabo Silleiro, revelou a importância dos ciclos de afloramento/convergência na circulação e hidrografia na plataforma continental. Nas estações de outono/inverno, correntes para o polo ocorrem na plataforma continental associadas a períodos de convergência com ventos variáveis, e são formadas plumas de água doce provenientes do aumento do caudal dos rios. Esta situação ocorreu no outono de 2009 mas não no outono de 2008, quando foi observado afloramento intenso, adiando o período de convergência para o inverno (janeiro-fevereiro 2009). Em 2009 o afloramento foi predominante na primavera e no verão, no entanto a frente de afloramento só se desenvolveu completamente em agosto e setembro. Em junho e julho, advecção de águas quentes de sul, associada a eventos de convergência, atrasaram o desenvolvimento da frente. A configuração do modelo numérico desenvolvido neste trabalho foi validada com o conjunto de dados observacionais, o que demonstra a sua aplicabilidade a estudos multidisciplinares regionais.

Keywords Western Iberian Margin, coastal upwelling, shelf, regional ocean modeling, ROMS-AGRIF, coastal dynamics, hydrography, mesoscale, seasonal variability.

Abstract The Western Iberian Margin (WIM) is characterized by summer upwelling and winter downwelling, with alternating conditions at short time scales throughout the year. During summer upwelling, offshore-flowing jets may develop on the shelf and give rise to long, narrow upwelling filaments extending far from coast. The aim of this thesis is to study the WIM hydrography and circulation, using both an ensemble of observations consisting of *in situ* cruises and remote sensing on one hand, and state-of-the-art model configurations using ROMS-AGRIF on the other hand. Three distinct approaches were carried out to assess different time and spatial scales: (1) Assessment of the mesoscale filaments field in the summer for the years 2001-2010 using sea surface temperature from satellite and modeling; (2) The shelf response to upwelling/relaxation cycles on the Northwestern Iberian Margin (NWIM) in July 2009 from an extensive oceanographic cruise; (3) The shelf circulation and hydrography during an annual cycle (November 2008-December 2009) through monthly cruises and a high resolution modeling configuration.

Filaments were generally found anchored to the main bathymetric and coastal features but off the smoother northern coast of the WIM, their locations were more variable. There was a clear relation between upwelling-favorable wind strength and the number and length of filaments in the southern region, although the relation was weaker in the northern region. Filaments were also related to eddies during periods of weak winds. Along the smoother northern coast in July 2009, under upwelling favorable winds, an upwelling center was found from cape Silleiro to Porto, where the surface temperature was colder than the neighboring regions. As these winds relaxed, persistent poleward flow developed, with an origin south of the upwelling center and consisting in an inner-shelf tongue of warm waters. Furthermore, study of the full annual cycle for the NWIM around cape Silleiro, between November 2008 to December 2009, revealed the importance of the upwelling/downwelling cycles on the shelf circulation and hydrography. In autumn/winter seasons, poleward flows occur on the shelf due to periods of downwelling favorable highly variable winds, and is formed the Western Iberian Buoyant Plume (WIBP) originated by the higher river flows. This situation occurred in autumn 2009 but not in autumn 2008, when unusually intense upwelling was found, delaying the downwelling favorable period to the winter season (January-February 2009). Upwelling prevailed in spring and summer 2009, although the upwelling front was fully developed only in August and September 2009. This was because in June and July downwelling events were associated with the generation of an inner shelf poleward flow, transporting warm waters. The numerical model configuration used in this work was validated with the set of observations and hence, its applicability to regional multidisciplinary studies was demonstrated.

Contents

List of Figures

List of Acronyms

AVHRR	Advanced Very High Resolution Radiometer
ADCP	Acoustic Doppler Current Profiler
AGRIF	Adaptive Grid Refinement In Fortran
ECMWF	European Center for Medium range Weather Forecasting
ENACW	Eastern North Atlantic Central Waters
ENACWsp	Eastern North Atlantic Central Waters with subpolar origin
ENACWst	Eastern North Atlantic Central Waters with subtropical origin
CESAM	Centro de Estudos do Ambiente e do Mar
CMEMS	Copernicus Marine Environment Monitoring Service
CTD	Conductivity, Temperature and Depth
EOF	Empirical Orthogonal Function
GPS	Global Positioning System
HAB	Harmful Algal Bloom
IBI-MFC	Iberia–Biscay–Ireland Monitoring and Forecasting Center
IPC	Iberian Poleward Current
lADCP	Lowered Acoustic Doppler Current Profiler
mab	meters above bottom
mADCP	Moored Acoustic Doppler Current Profiler
NAO	North Atlantic Oscilation
NWIc	Northwestern Iberian configuration
NWIM	Northwestern Iberian Margin
PC	Principal Component
RMSD	Centered Root Mean Square Difference
ROMS	Regional Ocean Modeling System

RV	Research Vessel
rvEOF	Real Vector Empirical Orthogonal Function
SST	Sea Surface Temperature
vmADCP	Vessel Mounted Acoustic Doppler Current Profiler
WIBP	Western Iberian Buoyant Plume
WIc	Western Iberian configuration
WIM	Western Iberian Margin
WRF	Weather Research and Forecasting Model

Chapter 1

Introduction

1.1 Overview, Motivation and Objectives

In the Eastern Boundary of the Atlantic Ocean, the Western Iberian region has been increasingly studied since the 70's of the last century, from the point of view of physical oceanography. The knowledge of the oceanic circulation in coastal areas had since evolved jointly with the marine biogeochemistry, larval and pollutants transport and its ecological and environmental implications. Several projects have contributed to develop the knowledge of the regional oceanography and its role within multi-disciplinary studies (such as SEFOS, OMEX I and II, ARCANE, MORENA, CAIBEX, Hydroprestige, Dybaga).

On the other hand, several PhD theses were devoted to the oceanography of the region with *Fiuza* (1984) pioneering study of the Western Iberian upwelling season. To name a few of the PhD that followed, *Haynes* (1993), *Sousa* (1995) and *Relvas* (1999) studied filaments with various observational methodologies, *Mazé* (1995) was dedicated to the volume budget transport. The Iberian Poleward current was extensively studied by *Dubert* (1998), *Coelho* (2001), *Peliz* (2002), *Teles-Machado* (2014). *Serra* (2004) was devoted to the study of the Mediterranean outflow. *Rossi* (2010) expanded on the upwelling interactions with the shelf in central Western Iberia. An observational study of the deep water hydrography on the Finisterre region was done by *Prieto* (2014). The circulation on the Western Iberian Margin was studied by *Pires* (2013) and assessed for the predicted climate change scenario.

More local studies by *Otero* (2008), *Sousa* (2013) and *Mendes* (2016) focused on the coastal fresh water plume dynamics, and *Herrera* (2008) analyzed a seasonal cycle of the shelf circulation near Rias Baixas.

The present PhD thesis aims to continue the works referred above by providing new content to the understanding of circulation processes on the Western Iberian Margin (WIM).

This work started on a study of the filaments and other mesoscale features at the scale of the full WIM to update on the previous works by *Haynes et al.* (1993a) and include a modeling component. The results and some ideas about these features spatial and temporal distributions are discussed in Chapter 2. The results of this study motivated a focus on the northern region of the WIM (NWIM), specifically between the latitudes of Porto and Finisterre, a region with intensified upwelling centers. The data set from the CAIBEX project was used to further explore the circulation and variability in the NWIM. The initial stages of the upwelling season of 2009 were analyzed in Chapter 3, profiting from the data availability of a 3-week cruise on board of the RV *Sarmiento de Gamboa*. From the analysis of the upwelling season of that year, the time span of the study was extended to a full seasonal cycle in Chapter 4 (November 2008 to December 2009), based on monthly cruises across the shelf near cape Silleiro (42.1°N) and two moorings at the same latitude. Another challenge was the implementation of a realistic model configuration designed to solve the seasonal cycle and to understand the processes underlying the available observations, which was also explored in Chapter 4.

In the following sections of this chapter, an introduction to the WIM regional oceanography related to the subject of this thesis is presented. Additionally, the observational data and numerical model configurations are described.

1.2 The Western Iberian Margin

1.2.1 Shelf and Coastal Morphology

The Western Iberian coastal region (Fig. 1.1) contains several canyons (e.g. Porto, Aveiro, Nazaré and Setúbal), a major promontory (Estremadura) and capes. The most important include 90° angled capes (Cape São Vicente, Cape Roca and Cape Finisterre) and other coastal protuberances such as Cape Sines, Cape Carvoeiro and Cape Mondego.

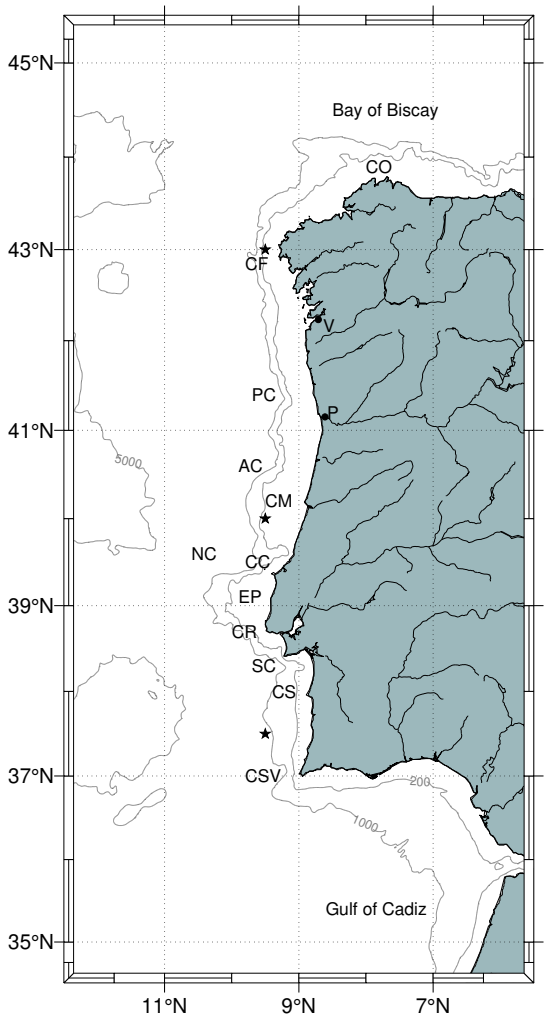

Figure 1.1: Map of the Western Iberian Margin, bounded to the north by Bay of Biscay and to the south by Gulf of Cádiz. The main topographic features marked on the map are: Cape Ortegal (CO), Cape Finisterre (CF), Porto Canyon (PC), Aveiro Canyon (AC), Cape Mondego (CM), Nazaré Canyon (NC), Cape Carveiro (CC), Estremadura Promontory (EP), Cape Roca (CR), Setubal Canyon (SC), Cape Sines (CS) and Cape São Vicente. Points in land represent the cities of Vigo (V) and Porto (P). The *stars* mark the locations of wind data detailed in Section 2.2.4. Gray contours represent the isobaths 200m, 1000m and 5000m

The Northwestern Iberian Margin (NWIM) stretches from Cape Mondego to Cape Finisterre (40°N to 43°N in Fig 1.2). North of Cape Silleiro (42°06'N), the coastline is made up of a series of embayments, the Rías Baixas; to the south, it is relatively smooth and oriented approximately NNW as far as Porto (41°06'N). The shelf deepens gently to the shelf edge at the 200-m isobath, and is bounded by a steep slope that plunges to 2000-

4000 m. To the south of Porto Canyon (41°20'N) the shelf is around 50-60 km wide, while to the north it narrows. South of Beiral de Viana (41°40'N) the inner shelf (inshore of 100-m isobath) is wider.

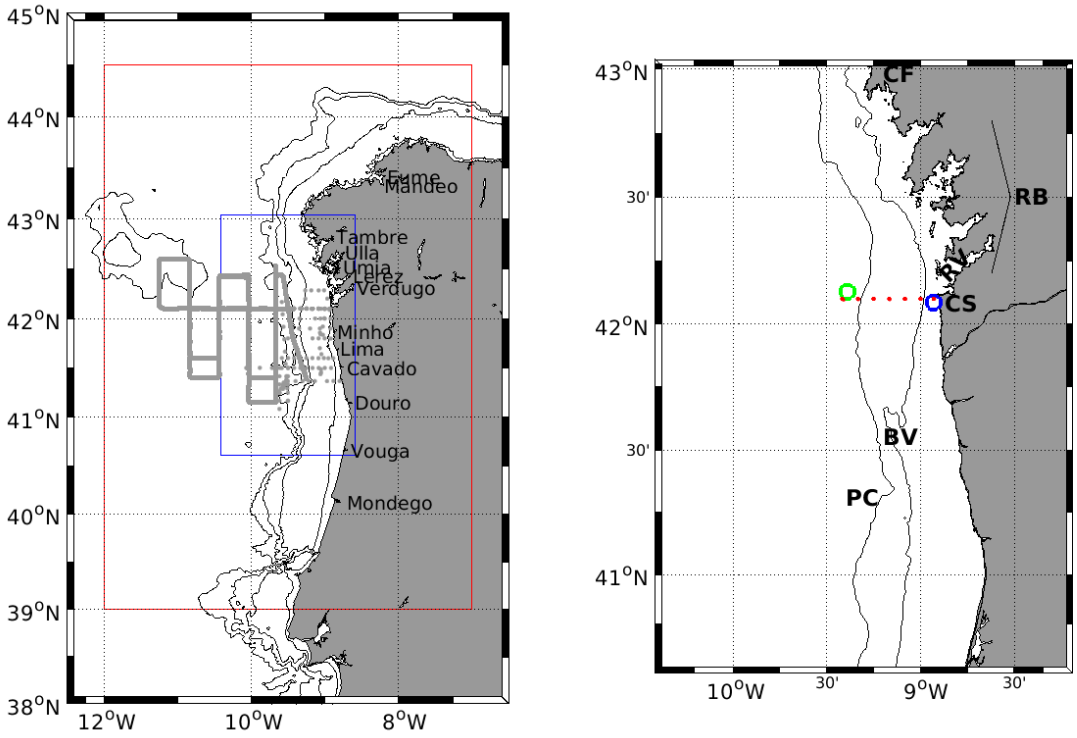

Figure 1.2: a) Map of the Northwestern Iberian Margin with the limits of the model domains (red - NWIc, blue - NWIc-1) and the path of the RV *Sarmiento de Gamboa* during the July 2009 cruise in gray. b) Zoom to the NWIc-1 domain depicting the position of the observational data (blue - moored ADCP, green - Silleiro Buoy, red - CTD stations from monthly cruises) and initials represent the location of coastal features: Cape Finisterre (CF), Rías Baixas (RB), Cape Silleiro (CS) and bathymetric features: Beiral de Viana (BV) and Porto Canyon (PC).

1.2.2 Atmospheric Considerations

The Western Iberian Margin (WIM) is part of the North Atlantic eastern boundary (*Relvas et al.*, 2007). Like other Eastern Boundary Upwelling Systems, atmospheric high-pressure systems are located in the mid-latitudes and in the proximity of the western coasts. In particular for the Eastern North Atlantic, the wind regime is dictated by the relative location of the anticyclonic system of the Azores High and the cyclonic System of the Iceland Low. The position of the Azores High oscillates between northern locations

off the Iberian Peninsula during summer and a southern position during winter, while the Iceland low intensifies, leaving room to the eastward passage of low pressure systems. As consequence, the circulation at the Iberian Peninsula increases its variability during wintertime (*Vitorino et al.*, 2002). The moisture carried onto the Iberian Peninsula results in higher precipitation in winter with a strong link to the North Atlantic Oscilation (NAO) (*Miranda et al.*, 2002).

Associated with the atmospheric conditions, the exposure of the ocean surface layers to shortwave radiation increases in spring and is the highest in summer. In autumn, with receding length of daytime and increasing cloud coverage the shortwave exposure diminishes until its minimum in winter.

1.2.3 The Water Column

The atmospheric factors influence the physical properties of the surface waters, in terms of advection by the resulting circulation or in terms of local heat and mass fluxes between atmosphere and the ocean surface. The temperature of the WIM surface layer waters has a clear annual cycle, being colder and homogeneous in the winter (January-March), with typical values of 12.5°C-13°C. This surface layer, where stratification is minimal, is typically restricted to the top 100 m, although in winters with strong wind events, the surface mixed layer can become as deep as 200 m (*Reboreda et al.*, 2014). The salinity at this surface layer is also homogeneous, being regulated by mixing at the bottom of the buoyant plumes formed above by continental runoff of fresh waters and local precipitation.

With the onset of spring, with weaker wind events and increasing light availability, the surface becomes warmer (up to 21°C-22°C offshore) and stratification increases, forming a thermocline at shallower depths, which remains until the end of summer season.

During autumn, with the onset of strong storms, the surface waters lose heat due to higher mixing from wind blowing on the ocean surface. The result is a return to the colder temperatures of winter, although a poleward flowing current (Iberian Poleward Current - IPC), intensified at the slope, is responsible for the advection of warm waters from the southern region, slowing down the cooling at the NWIM.

The Eastern North Atlantic Central Waters (ENACW) occupy depths below the surface mixed layer. Two different sources of ENACW exist (*Rios et al.*, 1992), one with a colder and fresher signature originated on subpolar latitudes north of the WIM (ENACWp) and other with warmer and saltier signature originated on subtropical latitudes and transported northward through branches of the Azores Current (ENACWt). The standard definitions of the ENACW branches were originally proposed by *Fiuza* (1984) and correspond to lines

in a Temperature/Salinity space. The ENACWt connects the points with coordinates [T = 10°C; S = 35.4] to [T = 12.20°C; S = 35.66] and the ENACWp conects the points with coordinates ENACWt connects the points with coordinates [T = 13.13°C; S = 35.8] to [T = 18.5°C; S = 36.75]. Under 400 m - 500 m depth, there is a region of transition between the central waters and the influence of the Mediterranean waters flow, in which the salinity increases to values in the interval [35.9-36.3], depending on the distance to the Strait of Gibraltar (*Nolasco et al.*, 2013a). The influence of the Mediterranean waters is maximum around 800 m depth and 1200 m depth, where two cores of the Mediterranean undercurrent exist.

1.2.4 The Iberian Poleward Current

As with other Eastern Boundary Systems, the large scale circulation is dominated by an offshore slow equatorward flow, the Portugal Current, forming part of the subtropical gyre recirculation (*Saunders*, 1982). This flow co-exists with the counter flow of the IPC over the slope region, driven mainly by a meridional density gradient and the wind (*Frouin et al.*, 1990; *Peliz et al.*, 2003a). It is linked to the branch of the Azores Current shifting poleward by its interaction with the western Iberian slope, and continues flowing along the slope as far as Celtic banks (*Garcia-Soto*, 2002).

In the wake of the upwelling season, around September and October, downwelling pulses become more prevalent, which results in the intensification of the IPC at the surface until becoming a surface intensified jet around December and January (*Teles-Machado et al.*, 2016). The IPC is thought to be present all year round, although it weakens and spreads offshore in spring and is confined to the subsurface during summer, below the upwelling jet (*Huthnance et al.*, 2002). During the early upwelling season, the offshore IPC has been observed to coexist with shelf and slope equatorward flows (*Torres and Barton*, 2007).

The ENACWt transported by a stronger IPC reach higher latitudes, so the front between ENACWt and ENACWp, on the shelf, moves northward during the winter and southward in the summer (*Castro*, 1996; *Herrera et al.*, 2008). The position of the front in the winter can be substantially different each year, typically remaining around the latitude of cape Finisterre.

1.2.5 Western Iberian Buoyant Plume

The passage of atmospheric low pressure frontal systems, is responsible for higher precipitation rates on the Iberian Peninsula, which results in increased continental flow into

the ocean. Due to buoyancy, the fresh waters exported from rivers or estuaries are restricted to the surface layers with a clear halocline (commonly defined at 35.7) over the denser oceanic waters. In this region several river plumes overlap into one denominated generically as the Western Iberian Buoyant Plume (WIBP) by *Peliz et al.* (2002), and studied in detail by *Otero et al.* (2008) and *Mendes et al.* (2016).

In the absence of other forcing mechanisms, waters exported at the mouth of rivers and estuaries are deflected in the direction of the coastally trapped waves (*Chao and Boicourt*, 1986). On the western Iberian shelf, the plumes generated by the exported waters bulb in front the river mouths and a poleward flow forms adjacent to the coast (*Horner-Devine et al.*, 2015). When forced by southerly winds, Ekman transport forces the surface layers coastward constraining the plumes against the coast. As a result, the halocline of the plumes deepens nearshore, to the point where it can reach the bottom, and become vertical in situations of strong southerly winds.

Under northerly winds, westward Ekman transport spreads the plume across shelf and thins at the surface, and the plume waters are transported southwestwards by equatorward flows until disappearing by mixing with oceanic waters.

During periods of high continental runoff, the resulting buoyant plumes contribute to the coastal poleward flow (*Otero et al.*, 2008). Under downwelling conditions, the plume waters from the rivers to the south may reach and enter the Rías Baixas, as surface fresh waters accumulate inside and warm through shortwave radiation (*Barton et al.*, 2015). In subsequent upwelling events, these waters are exported to the shelf, with lower salinity and higher temperature than the locally upwelled waters (*Álvarez-Salgado et al.*, 2000; *Torres and Barton*, 2007).

1.2.6 Upwelling Season

With the onset of the spring transition in the Western Iberian Margin (WIM), surface stratification develops and strengthens, as insulation increases. Associated with the stratification, a thermocline is formed in the subsurface ($<$100 m), separating the warm surface mixed layer from the colder central waters. The upwelling season starts in response to the northerly winds, resulting from the build-up of the Azores high (*Wooster et al.*, 1976). The continental shelf circulation is typically set up on a scale of an inertial period in response to the atmospheric forcing, and reach the situation of equilibrium after 3 or more days (*McClain et al.*, 1986). When northerly winds blow along the Western Iberian meridional coast, surface coastal waters are transported offshore through an Ekman layer, and are replaced by rising of subsurface cold central waters (*Rossi et al.*, 2013). As a

consequence, the sea level falls close to the coast and an equatorward flow develops in geostrophic balance, parallel to the front between coastal cold upwelled waters and the offshore warmer waters (*Ambar and Fiuza*, 1994). The front typically moves offshore with prevailing upwelling-favorable winds (*Austin and Lentz*, 2002) and becomes constricted to the shelf edge vicinity (*Rossi et al.*, 2010).

The upwelling favorable season in the Western Iberian Margin (WIM) typicaly occurs between June and September (*Wooster et al.*, 1976; *Nykjær and Van Camp*, 1994), when the northward shift of the Azores high pressure system produces northerly winds in the region. In spite of the predominance of upwelling during summer, downwelling interludes are frequently observed during wind relaxations associated with the rapid passage of low pressure systems (*Torres and Barton*, 2007), which occur in cycles of 14 days or less (*Álvarez-Salgado et al.*, 1993). Generally, coastal upwelling cycles are asymmetric (*Send et al.*, 1987). When upwelling-favorable winds relax, coastal temperatures become warmer, not only by a return of the water previously displaced offshore, but also as a result of poleward advection in a coastal current. Poleward flows of warm waters have been reported on the western Iberian inner shelf during relaxations in spring (*Torres and Barton*, 2007) and summer (*Sordo et al.*, 2001; *Peliz et al.*, 2002). These transient poleward shelf flows are distinct from the offshore IPC and have a variety of causes. In the summer, coastal poleward flows may be forced by alongshore density gradients, alongshore differences in wind forcing and by interaction of the flow with topographic features (*Gan and Allen*, 2002; *Relvas and Barton*, 2005; *Pringle and Dever*, 2009; *Washburn et al.*, 2011).

The neighborhood of Cape Finisterre and the region between Cape Silleiro and Porto (Fig 1.3), are known to present centers of intensified upwelling (*Relvas et al.*, 2007), in which coastal upwelled waters are colder than elsewhere. Causes for the existence of intensified local upwelling include the spatial variability of the wind (*Pringle and Dever*, 2009) and the shelf width (*Pringle*, 2002). The upwelling center near Cape Finisterre could also be related with the 90°change in orientation of the coast and the related wind stress curl (*Torres et al.*, 2003).

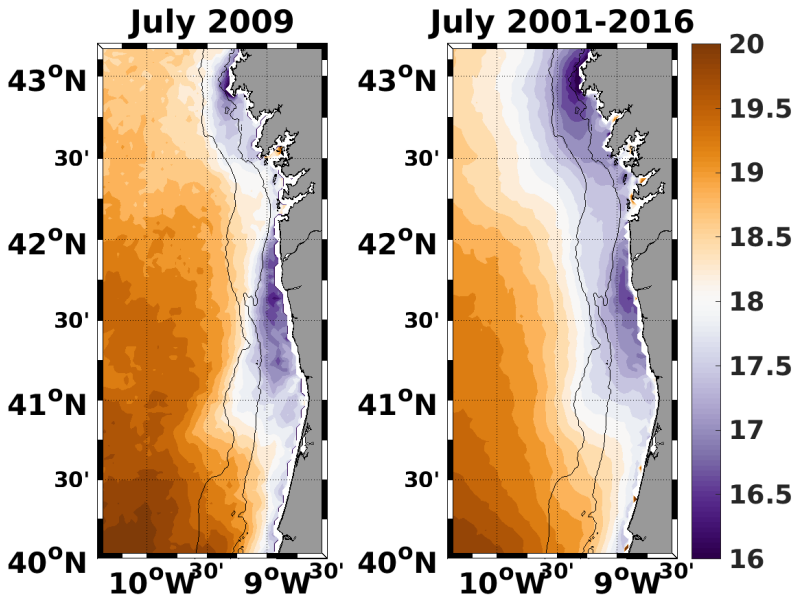

Figure 1.3: Average SST maps of July 2009 (left) and July of 2001-2016 (right) from AVHRR satellite data. The 100-m and 200-m bathymetric depths are represented in dark lines.

Filament Formation

Associated with the summer upwelling, an alongshore thermal front is generated, separating the surface warmer waters offshore from near-shore upwelled colder central waters. The typical temperature gradients across the front are between 0.1 to 0.2 °C/km. This thermal upwelling front becomes subject to frontal instabilities consisting of baroclinic waves of short wavelength (O(20) km) (*Barth*, 1994). With a succession of upwelling-favorable (northerly) wind events, the thermal front typically moves intermittently offshore until about mid-August, and longer baroclinic frontal instabilities develop (*Narimousa and Maxworthy*, 1989; *Røed and Shi*, 1999) with scales of wavelength about $2\pi \cdot R$ with $R \approx \frac{\sqrt{g'h}}{f}$ being the Rossby deformation radius where g' is reduced gravity, h is surface layer depth and f is the Coriolis parameter.

In upwelling systems the instabilities associated with the equatorward jet typically develop into meanders, eddies and the so-called filaments. The latter are prominent, contorted tongues of upwelled water that extend dozens to hundreds of kilometers offshore and whose width is O(10) km (*Haynes et al.*, 1993a).

Haynes et al. (1993a) considered several filament formation processes along the WIM, originally proposed by *Strub et al.* (1991). One is filament generation arising from dy-

namical instabilities on the upwelling-associated equatorward jet. Another is the effect of coastline and continental shelf irregularities (capes, canyons and promontories) on the separation of alongshore currents and consequently formation of strong offshore fluxes. A third is interaction of pre-existing mesoscale field with the upwelling fronts and jets, to generate localized cross-shelf fluxes. In the case of the WIM, the influence of the Iberian Poleward Current and Mediterranean Water vein on the water column can condition the mesoscale field with the presence of meddies and the Mediterranean undercurrent (*Serra et al.*, 2010; *Nolasco et al.*, 2013a). *Røed and Shi* (1999) performed numerical simulations for the western Iberian coast with a 1 1/2 layers model, supporting the idea that filament generation is initialized by dynamical instabilities of the equatorward jet that can be intensified or diminished by topographic features.

These formation mechanisms are not mutually exclusive, particularly on the Atlantic coast of the Iberian Peninsula, with its complex bathymetry and coastline (Fig. 1.1). As was found off Iberia by *Haynes et al.* (1993a), filaments are usually anchored to and downstream of the topographic features responsible for the generation of the instability, namely capes and submarine ridges (*Narimousa and Maxworthy*, 1989). However, in the study of *Røed and Shi* (1999) filaments were found even with straight coastline and bathymetry.

The filaments of cold upwelled water contribute to exchange processes between productive coastal waters and oligotrophic open ocean waters, e.g, the transport of nutrients and chlorophyll to the open ocean (*Cravo et al.*, 2010; *Rossi et al.*, 2010). Characterizing the frequency, localization and dimensions of filaments is important for a better knowledge of the exchanges between coast and ocean. This characterization can be based on observational data (*Flament et al.*, 1985) or numerical modeling (*Troupin et al.*, 2012).

1.3 Observational Data Set

1.3.1 CAIBEX Data

The project "Shelf–ocean exchanges in the Canaries–Iberian Large Marine Ecosystem", CAIBEX, ref. CTM2007-66408-C02, consisted partly on the hydrographic, hydrodynamic and biogeochemical characterization of the coastal upwelling system of the NW Iberian Peninsula in the vicinity of Cape Silleiro. Starting in November 2008 and through 2009, a set of surveys named CAIBEX-LOCO was performed aboard the Research Vessel (RV) *Mytilus*, monitoring several parameters in the LOCO station (42.1°N, 8.95°W). On a quasi-monthly frequency, measurements of temperature, salinity, fluorescence, transmittance, oxygen and turbidity were performed in two transects crossing the LOCO station, one per-

pendicular and the other parallel to the coast. At each cruise, the perpendicular transect was performed twice, in which the offshore moving part was made in 7 equally spaced conductivity-temperature-depth (CTD) stations, and the onshore moving part was continuously performed with a towed CTD (Minibat). Continuous current measurements were performed with the vessel mounted Acoustic Doppler Current Profiler (vmADCP). The operations of installing and recovering the mooring at the LOCO station, necessary for the data retrieval as well as instrument maintenance, were performed on board of the RV *Mytilus* in 9 other cruises of approximately 8 hours. Also included in the CAIBEX project, the coastal upwelling system of the NW Iberian Peninsula was surveyed in an intensive cruise on board of the RV *Sarmiento de Gamboa* between 6 and 24 of July 2009.

Moored ADCP

An upward looking 500 KHz SonTek Acoustic Doppler Current Profiler (hereafter named mADCP) was moored at 72 m depth (blue star in Fig. 1.2, -8.93°W; 42.08°N) starting in November 2008 until December 2009 (with 3 interruptions for maintenance). After excluding outliers and anomalous values, the alongshore currents measured by the mADCP were obtained in 3 m bins and at each depth low-pass filtered with half-power at 33h.

Monthly Surveys

Between November 2008 and November 2009, 11 hydrographic surveys were performed aboard RV *Mytilus* along a 42.1°N cross shore section. Each survey consisted of seven equally spaced stations starting at 8.93°W until 9.44°W (Fig. 4.1), monitoring quasi-monthly the temperature and salinity by lowering a CTD seabird 25. Only the downcast of the CTD profile was used and averaged in 0.5 m sized bins. Treatment of the salinity profiles consisted on the removal of values outside of an expected range ($25<\text{salinity}<37$) and replacing them with linear interpolation of the nearest points. For both temperature and salinity profiles a 5-point running median filter was applied, in which the median of the 5 bins above and below each bin was calculated. The value of the bin would be replaced by the 5-point median if their difference was higher than a certain threshold (temperature >0.3°C and salinity >0.1). Lastly a 3-point running mean was applied to filter small scale fluctuations, replacing all bins by the mean of the 3 bins above and below.

An RDI broadband 300 kHz vmADCP registered, to a maximum of 150 m, depth current profiles along the transect, averaged in 15 min intervals.

On the way back of each cross-shore transect an undulating minibat, carrying a seabird

CTD, was towed at 7 m/s and produced continuous profiles of temperature and salinity. The spacing of each profile varied between 0.01 and 0.1 ° in longitude. An objective analysis gaussian interpolation, named Barnes Objective Analysis Scheme (*Barnes*, 1994), was applied to transform the data into a regular 2-D grid, with horizontal resolution of 0.005° and vertical resolution of 1 m between -105 m and 0 m. The parameters used consisted on smoothing length scales XR = 0.06° and YR = 6 m performed in 2 iterations and a scale zoom factor of 0.8 between the first and the second iteration. The results of these measurements were only used in the confirmation of the CTD observations (its plots are shown in the Appendix B). Its high resolution reveals submesoscale features which are not in the scope of this study.

Near the mADCP location, between November 2008 and December 2009, 19 CTD stations were performed on the process of mounting and recovering the mooring of the LOCO station, during the 9 shorter cruises.

Intensive Survey - July 2009

From 7 to 23 July 2009, a cruise took place off the NW Iberian margin (Fig 1.1) on board the RV *Sarmiento de Gamboa*. Two hydrographic surveys were performed offshore of the 500 m isobath (gray line in Fig 1.2) with continuous tows of a *Seabird 911+* CTD probe on an undulating vehicle (SeaSoar) during the days 7-9 July and 21-23 July. The undulator was towed at 8 knots and cycled from near the surface down to 450 m depth providing a horizontal resolution of 3-4 km. Barnes Objective Analysis Scheme was applied to a grid with resolution of 2.5 km in the horizontal and 2 m vertical axis. The smoothing length scales were XR = 14 km and YR = 10 m made in 2 iterations with a gamma of 0.8.

At the CTD stations, a General Oceanics rosette equipped with a *Seabird 911+* CTD and both upward and downward looking 300 kHz lowered acoustic doppler current profilers (lADCP), was lowered to a maximum of 600 m depth. The lADCP data was processed with a publicly available software[1], consisting on the implementation of the velocity inversion method, developed at the Lamont-Doherty Earth Observatory (LDEO - Columbia University) (*Fischer and Visbeck*, 1993; *Visbeck*, 2002). With this software, the resulting currents are constrained to the near surface vmADCP data and to the lADCP bottom-track, when available. The software also uses the time and depth measured by the corresponding attached CTD cast.

At 9:00 on 17 July a drifter buoy was launched around the position of the 100 m isobath at 42°N, and was recovered at 6:00 of 21 July (blue line in Fig 3.2b). The buoy, equipped

[1]see ftp://ftp.ldeo.columbia.edu/pub/LADCP

with GPS and Iridium communications, was drogued at approximately 10 m depth.

An RDI 75 kHz Broadband ADCP mounted on the hull of the RV (vmADCP) registered the current from 24 m to a maximum depth of 750 m from 15:00 of 8 July to the end of the cruise. The vmADCP data was processed with the Common Oceanographic Data Access System (CODAS), developed at the University of Hawaii (*Firing et al.*, 1995). Alongshore and cross-shore currents were retrieved in 8-m vertical bins below 24 m depth, and over 15 minutes intervals in time.

Underway data were logged on board the vessel with an Aanderaa meteorological station at 10 m height, a Seabird thermosalinometer sampling water pumped from 5 m depth and the GPS system for navigation. Noisy spikes were removed from all underway data with a 1-h window running mean.

1.3.2 Satellite Imagery

Advanced Very High Resolution Radiometer (AVHRR) data of the NOAA, were made available by the EUMETSAT Ocean & Sea Ice Satellite Application Facility [2]. The regional SST is available at an approximate resolution of 2 km (*M-F/CMS*, 2009) and was retrieved for the months of May to October of years 2001 to 2010, for the night satellite pass. The SST climatology of July (Fig 1.3) was calculated using the same data set from years 2001 to 2016.

1.3.3 Silleiro Buoy

Observations from the Seawatch buoy off cape Silleiro (42°7.8'N, 9°23.4'W; green star in Fig. 1.2) were provided by Puertos del Estado (www.puertos.es). Hydrographic data consisted of currents, salinity and temperature at 3 m depth, measured with an RDI/UCM-60DL currentmeter and an AANDERAA 2994S. Wind direction and speed were obtained at 3 m high with a YOUNG/AANDERA 2740 and YOUNG/AANDERAA 3590.

1.4 Regional Modeling

1.4.1 Modeling the WIM

The synoptic view of the surveys is often ruled by small scale features that mask the seasonal cycle and large scale circulation. Realistic 3D modeling helps to fill-in those gaps,

[2] http://www.osi-saf.org

as their temporal resolution allow the visualization of transient processes in full cycles.

The numerical study of the circulation in the WIM is a challenge for modelers, with its narrow shelf and a steep slope, as well as the presence of numerous canyons and promontories, requiring high resolution to properly resolve the shelf/slope circulation, as well as the influence of the open ocean circulation (the Azores Current system and meridional pressure gradients) on the coastal transition zone, that forces the circulation in this region, and the Mediterranean undercurrent below, at around 1000 m depth. The development of high-resolution studies to deal with the different scales that influence the circulation of the WIM is crucial, and for that purpose a simulation based on nesting techniques was performed.

Previous numerical modeling studies have contributed to the knowledge of some aspects of the circulation at the full scale of the Iberian Upwelling System (*Nolasco et al.*, 2013a). Idealized studies provided clues to the behaviours of the main circulation regimes of the region, including the coastal upwelling and filament formation (*Røed and Shi*, 1999; *Meunier et al.*, 2010; *Rossi et al.*, 2010) and poleward slope currents (*Peliz et al.*, 2003b).

Serra et al. (2010) focused on the study of the influence of the Mediterranean water undercurrent on the surface circulation, with emphasis on the mesoscale phenomena. On the other hand, from the point of view of operational oceanography of the Western Iberian Margin, *Mateus et al.* (2012) and *Marta-Almeida et al.* (2012) focused on the application of operational configurations to discuss their potential in supporting scientific and coastal management activities. The application of numerical modeling to biological problems is also becoming fairly widespread, such as coupling with biogeochemichal modules (*Reboreda et al.*, 2014) or ecosystem interactions (*Nolasco et al.*, 2013b; *García-García et al.*, 2016; *Tanner et al.*, 2017; *Santos et al.*, 2018).

At the level of the NWIM, other models successfully simulated the coastal circulation (*Teles-Machado et al.*, 2016). At the event scale, some focused on the typical winter conditions with plume dynamics and its interaction with the Rias Baixas (*Otero et al.*, 2008, 2013; *Sousa et al.*, 2014; *Mendes et al.*, 2016). Operational applications to ecosystem problematics have also been developed, such as Harmful Algal Blooms (HAB) risk assessment (*Ruiz-Villarreal et al.*, 2016) or prediction of oil spill trajectories (*Marta-Almeida et al.*, 2013).

1.4.2 The Model (Regional Ocean Modeling System)

The Regional Ocean Modeling Systems (ROMS) is a split-explicit, free-surface, topography following coordinate model, designed to resolve regional problems (*Shchepetkin*,

2003; *Shchepetkin and McWilliams*, 2005). ROMS solves the incompressible primitive equations based on the Boussinesq and hydrostatic approximations, and is coupled with advection/diffusion schemes for potential temperature and salinity as well as a nonlinear equation of state.

Expressed in Cartesian coordinates *x, y, z*, the conservation equations take the form:

$$\frac{\partial T}{\partial t} = -u\frac{\partial T}{\partial x} - v\frac{\partial T}{\partial y} - w\frac{\partial T}{\partial z} + \mathfrak{F}_{\mathfrak{T}} + \mathfrak{D}_{\mathfrak{T}} \tag{1.1}$$

$$\frac{\partial S}{\partial t} = -u\frac{\partial S}{\partial x} - v\frac{\partial S}{\partial y} - w\frac{\partial S}{\partial z} + \mathfrak{F}_{\mathfrak{S}} + \mathfrak{D}_{\mathfrak{S}} \tag{1.2}$$

$$\frac{\partial u}{\partial t} = -u\frac{\partial u}{\partial x} - v\frac{\partial u}{\partial y} - w\frac{\partial u}{\partial z} + fv - \frac{\partial \phi}{\partial x} + \mathfrak{F}_{\mathfrak{u}} + \mathfrak{D}_{\mathfrak{u}} \tag{1.3}$$

$$\frac{\partial v}{\partial t} = -u\frac{\partial v}{\partial x} - v\frac{\partial v}{\partial y} - w\frac{\partial v}{\partial z} - fu - \frac{\partial \phi}{\partial y} + \mathfrak{F}_{\mathfrak{v}} + \mathfrak{D}_{\mathfrak{v}} \tag{1.4}$$

$$\frac{\partial \phi}{\partial z} = -\frac{\rho g}{\rho_0} \tag{1.5}$$

$$0 = \frac{\partial u}{\partial x} + \frac{\partial v}{\partial y} + \frac{\partial w}{\partial z} \tag{1.6}$$

The momentum balance in the x and y directions are expressed by equations (1.3) and (1.4), whilst equations (1.2) and (1.1) express the time evolution of temperature and salinity, where *u, v, w* are the velocity $\vec{u}$ Cartesian components; f is the Coriolis parameter; ϕ is the dynamic pressure, expressed by $\phi = (\frac{P}{\rho_o})$; $\rho = \rho_o + \rho'$ is the water density (ρ_o the average density and ρ' the perturbation); g the acceleration of gravity; $\mathfrak{F}$ and $\mathfrak{D}$ are the friction and dissipation. Equation (1.5) represents the hydrostatic approximation to the momentum balance in the vertical direction, limits to the balance between the pressure gradient and the buoyancy forces. Under the Boussinesq approximation, the density variations were taken into account for the vertical momentum equation (1.5), but neglected in the others momentum equations. The continuity equation is expressed at the equation (1.6).

The advection scheme is based on the work done by *Marchesiello et al.* (2009), in order to reduce spurious diapycnal mixing in S-coordinate models characteristic of higher-order diffusive advection schemes. This scheme involves the split of advection and diffusion, as a biharmonic operator. Lateral viscosity is set to zero, except in the sponge layers, where it increases linearly toward the boundaries of the model. Vertical mixing consists in the

KPP (K-profile parameterization) scheme (*Large et al.*, 1994).

The vertical boundary conditions are described as follow:

At the surface z=ζ

$$\mathrm{K}_M \frac{\partial u}{\partial z} = \tau_s^x \tag{1.7}$$

$$\mathrm{K}_M \frac{\partial v}{\partial z} = \tau_s^y \tag{1.8}$$

$$\mathrm{K}_T \frac{\partial T}{\partial z} = \frac{Q_T}{\rho_0 C_p} \tag{1.9}$$

$$\mathrm{K}_S \frac{\partial S}{\partial z} = \frac{(E-P)S}{\rho_0} \tag{1.10}$$

$$w = \frac{\partial \zeta}{\partial t} + u\frac{\partial \zeta}{\partial x} + v\frac{\partial \zeta}{\partial y} \tag{1.11}$$

At the bottom z=-h

$$\mathrm{K}_M \frac{\partial u}{\partial z} = \tau_b^x \tag{1.12}$$

$$\mathrm{K}_M \frac{\partial v}{\partial z} = \tau_b^y \tag{1.13}$$

$$\mathrm{K}_T \frac{\partial T}{\partial z} = 0 \tag{1.14}$$

$$\mathrm{K}_S \frac{\partial S}{\partial z} = 0 \tag{1.15}$$

$$w = -u\frac{\partial H}{\partial x} - v\frac{\partial H}{\partial y} \tag{1.16}$$

where ζ is the free surface elevation; $\mathrm{K}_M, \mathrm{K}_T, \mathrm{K}_S$ are the vertical turbulent mixing coefficients; τ_s^x, τ_s^y are the surface wind stress components; τ_b^x, τ_b^y are the bottom stress components (parameterized, quadratic drag coefficient of 5×10^{-3}); Q_T is the surface heat flux; C_p is the heat capacity of the ocean; *E-P* is the evaporation minus precipitation; H is the resting thickness of the water column. Equations 1.7 and 1.8 indicate wind stress at the surface and equations 1.12 and 1.13 at the bottom. Heat fluxes are represented by equations 1.9 (surface) and 1.14 (bottom), and salinities fluxes by equations 1.10 (surface)

and 1.15 (bottom). Equations 1.11 and 1.16 describe the vertical velocity at the surface and at the bottom, respectively.

One of the advantages of the ROMS is the terrain-following S-coordinates, which means that all the locations with different depths, from the coast to the higher depths, have the same number of levels. Consequently, a non-linear stretching factor is applied to the surface (θ_s) and to the bottom (θ_b), in order to generate a more uniform vertical resolution near the surface or the bottom, hence a better representation of the mixed layer and the thermocline is done. In the horizontal direction is adopted an Arakawa "C" grid, where u and v (components of the velocity vectors) are defined on the grid lines and all the other variables inside each grid cells (temperature, salinity, the resting thickness of the water column, the Coriolis parameter, the density, the free surface elevation and the vertical velocity).

The configurations developed for this work not only resolve the large-scale circulation patterns and their influence on the coastal transition zone of WIM, but also resolve explicitly unique local features, such as river plumes and current interactions with the topography. For the purpose of simulating different timescales, nesting is applied using the Adaptive Grid Refinement In Fortran (ROMS-AGRIF) (*Penven et al.*, 2006; *Shchepetkin and McWilliams*, 2005). The domains and resolutions are described in the next subsection.

1.4.3 Western Iberian Configuration - WIc

A configuration of ROMS-AGRIF was run for a domain covering the full Western Iberian Margin (named WIc) simulating years 2001 to 2010. The WIc domain has $1/27°$ horizontal resolution, covering the area presented in Fig. 1.1, also applied in *Reboreda et al.* (2014); *Nolasco et al.* (2013a). The vertical distribution consists of 60 vertical S-levels with $\theta_s = 4$ and $\theta_b = 0$ to enhance surface layers resolution. The topography by *Sibuet et al.* (2004) was used, which has a resolution of $\sim$ 1 km and was smoothed in order to fulfill the r-factor criteria ($r < 0.2$).

For the period 2001 to 2010, a large domain (comprising the Northeastern Atlantic Ocean) provided boundary and initial conditions for the WIc domain using an offline nesting procedure. The large domain was first initialized from rest using monthly temperature and salinity climatologies from World Ocean Atlas (WOA09) (*Locarnini et al.*, 2010; *Antonov et al.*, 2010) as its initial condition and at the boundaries. The large domain was forced with monthly surface fluxes from Comprehensive Ocean-Atmosphere Data Set (COADS), similar to the simulation in *Nolasco et al.* (2013a). After reaching equilibrium (5 years), realistic forcing was used at the surface as done in *Reboreda et al.* (2014). The

forcing of the large scale and WIc domains consisted of the NCEP-2 reanalysis of air-sea fluxes (www.ncep.noaa.gov) and QuikSCAT/ASCAT satellite winds from CERSAT (cersat.ifremer.fr) for the period 2001 to 2010. QuikSCAT winds were used from January 2001 to February 2009 with 0.5° resolution and ASCAT from March 2009 to December 2010 with 0.25° resolution (*Bentamy and Fillon*, 2012).

Open boundary conditions are provided as a nudging sponge layer in a band of 40 km, with a lateral viscosity coefficient ranging from 200 $m^2 s^{-1}$ at the boundary to zero at the interior. At the Strait of Gibraltar, at the southeastern boundary, the water exchange with the Mediterranean basin is explicitly represented in the domain, with the methodology of *Peliz et al.* (2007), consisting in the imposition of vertical profiles of temperature, salinity, and zonal velocity at the 5 grid points at the Strait. This condition is designed to setup a transport of 0.8 Sv leaving the domain through the surface layer, and 0.7 Sv entering the domain through the bottom layer. The process of entrainment of Atlantic Central Waters with the MU is also parameterized by increasing the viscosity and diffusivity coefficients in a region in which the MW is strongly mixed with the overlying Atlantic waters, until the MW vein forms along the northern slope of the Gulf of Cadiz.

1.4.4 NorthWestern Iberian Configuration - NWIc

A high-resolution ROMS-AGRIF configuration was made for the Northwestern Iberian margin (NWIM). A two-way nesting approach (*Debreu et al.*, 2012) was used, with a larger domain (NWIc) coupled with a higher resolution domain (NWIc-1), depicted as the red and blue bordered areas in Fig. 1.2, respectively. The NWIc domain comprised the region between 39°N-44.5°N and 12°W-7°W, and had horizontal resolution of 1/50° (∼1.65 km) and 45 vertical s-levels. The NWIc-1 was located between 40.5°N-43°N and 10.5°W-8.5°W, and had 1/150° (∼550 m) horizontal resolution and 45 vertical s-levels. For both domains, stretching factors of $\theta_S = 4$ and $\theta_B = 0$ were applied in the s-levels to enhance the surface resolution.

The bathymetry obtained through RAIA observatory[3] was used in the NWIc. This bathymetry has 1 arc-minute resolution and is based on ETOPO1 (*Amante and Eakins*, 2009) with corrections made by the Portuguese and French Hydrographic Offices (HIDROGRAFICO and SHOM). After interpolating to the grids of both the NWIc and NWIc-1 domains, a smoothing filter was applied to fulfill the $r = \delta h/2h < 0.2$ criteria (*Haidvogel and Beckmann*, 1999). Minimum depth was set to 5 m and the shoreline was manually adjusted to avoid channel rough edges and corners.

[3] http://www.marnaraia.org

Initial state of the physical variables (temperature, salinity, currents and sea surface height fields) was taken from a 1/12° resolution reanalysis, provided by the Iberia Biscay Ireland – Monitoring and Forecasting Center (IBI-MFC) within the Copernicus Marine Environment Monitoring Service (CMEMS) (*Levier et al.*, 2014). Although the resolution of this product is low compared to other regional products, due to its assimilation of in-situ temperature and salinity with Argo floats and sea surface temperature and sea level through remote sensing, it represents accuratelly the physical fields in the open ocean (*Aznar et al.*, 2016). This reanalysis also provided the boundary conditions, along nudging bands, to the larger domain, with the methodology by *Marchesiello et al.* (2001), with inflow (outflow) nudging timescales of 0.1 (36) days for tracers and 1 (36) day (s) for momentum. Sponge layers were applied in a band of 10 grid points, with the lateral viscosity coefficient of $180m^2/s$ at the boundary and linearly decreasing to zero at the interior, where the explicit diffusivity is also null.

The atmosphere-ocean fluxes were calculated from a WRF simulation of the Iberian region provided by Meteorology and Climatology Group of the University of Aveiro [4]. The configuration of the WRF simulation consisted on 3 nested domains, with 27-km, 9-km and 3-km resolution running in the period between 1 June 2008 and 31 December 2009. The larger domain was downscaled from the ECMWF reanalysis (ERA-INTERIM, *Simmons et al.* 2007) for the Eastern North Atlantic region and provided the boundaries for the nested higher resolution domains to encompass smaller scales in a cascade. The atmosphere-ocean fluxes of the smaller domain (3-km resolution roughly between latitudes 36°N and 45°N, and longitude 13.5°W and 5°W) were used in our study, through the surface fields of wind, temperature, radiation, precipitation and evaporation. An assessment of the wind data quality was performed for the Silleiro buoy location with comparison of the meridional and zonal wind components at 10 m high with the wind measured by the buoy anemometer (Fig.1.4). Pearson correlation coefficients between WRF and observed winds were calculated for the zonal component (r=0.89) and the meridional component (r=0.93). More information about this configuration can be obtained from *Carvalho et al.* (2012).

The rivers discharge was introduced at the mouth of the main regional rivers with measured flow and temperature when available. The rivers used in the study located in Spanish territory were the Eume, Mandeo, Tambre, Ulla, Umia, Lérez, Verdugo and Oitavén, in the Portuguese were the Lima, Cávado, Douro, Vouga and Mondego, and in the border between countries was the Minho (Fig.1.2). The Spanish rivers runoff was estimated from gauges available during the study period from MeteoGalicia (www.meteogalicia.es). Missing data

[4] http://climetua.fis.ua.pt

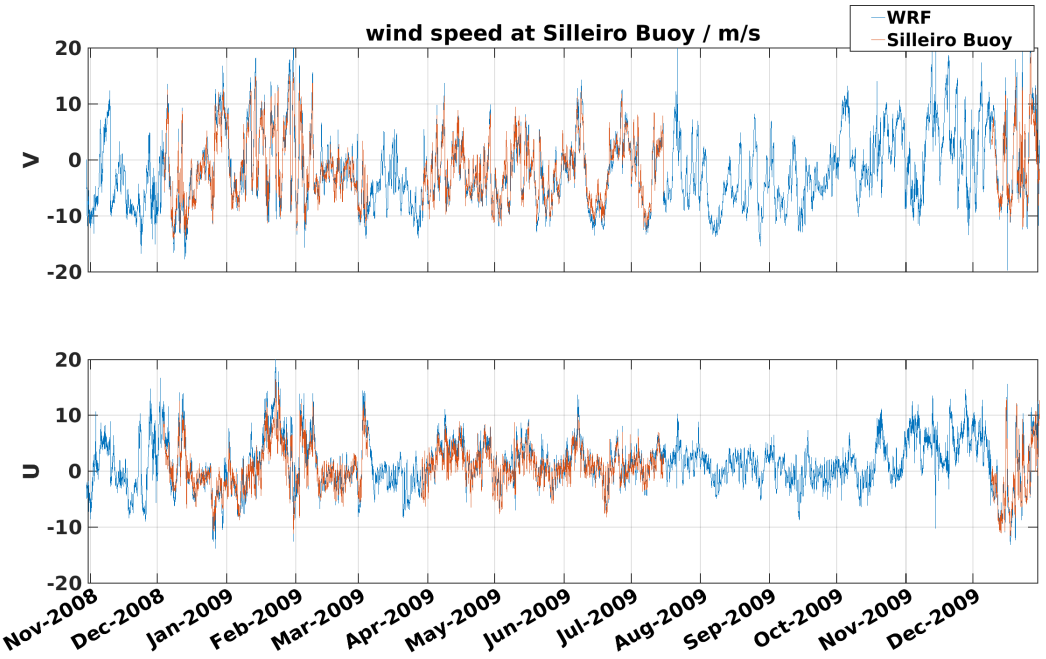

Figure 1.4: Timeseries of 10-m wind meridional (top) and zonal (bottom) components at the Silleiro Buoy (42°7.8'N, 9°23.4'W, from the WRF simulation (blue) and buoy anemometer (red). Negative (positive) values correspond to northerlies (southerlies) in the top panel and easterlies (westerlies) on the bottom panel.

was estimated based on runoff from available flow data of neighboring rivers. Estimates of river Minho discharge were taken from the mean daily flow at the Frieiras Dam, provided by Confederación Hidrografica Miño-Sil (www.chminosil.es). Flow and temperature of the Portuguese rivers were obtained from the SNIRH database (www.snirh.pt). Daily means were used for rivers Lima and Douro, while monthly climatologies were used for rivers Cávado, Vouga and Mondego. Constant salinity was applied at the surface cell at the river mouths considering that inside the estuaries, mixing occurs between the continental fresh waters and the oceanic waters. On Minho and the Spanish rivers, the salinity used were 10 and 7 on the NWIc and the NWIc-1 domains, respectively. The estuaries of the Portuguese rivers were not resolved by the model, so the salinity was set to 20 at their mouths on both domains.

Initialization of the NWIc domain was made for 1 June 2008 and run without nesting, allowing the adjustment from the lower resolution of the initial state (CMEMS reanalysis). On 20 August 2008, the NWIc-1 domain was introduced in a two-way nesting, starting the main simulation, which was run until 31 December 2009.

The simulations were performed using the High Performance Computing system, named

ARGUS, provided by CESAM, University of Aveiro. The main simulation, run from 20 August 2008 to 31 December 2009, took 164 hours to finish, completing 1 month of simulation in about 10h.

Chapter 2

Filaments in the WIM

The contents of this chapter have been published in *Cordeiro et al.* (2015).

2.1 Introduction

Satellite Sea Surface Temperature (SST) can help identify the surface mesoscale circulation, in which ocean frontal boundaries may be visible (*Bernstein et al.*, 1977). In Eastern Boundary Regions, SST products are commonly used for the identification of upwelling filaments (*Ikeda and Emery*, 1984; *Flament et al.*, 1985). The use of satellite SST products is limited by cloud cover, which interferes with continuous tracking of surface temperature structures. Given the continuity and the degree of realism of surface temperature from numerical modeling, modeled SST can be used to study the filament field along the WIM. To the authors' knowledge, no complete study has been made of filament distribution based on realistic modeling. The present work fills that gap by performing statistical analysis of filaments through modeled and satellite SST fields of the years 2001-2010 in the WIM. The inclusion of the modeling analysis is a major methodological advance from the work of *Haynes et al.* (1993a). Given the advances in observation and modeling of the WIM in the last decades, it is possible to provide more detailed interpretations of the filament behavior than previously, although the emphasis here is on their statistical properties.

The main objectives for this study are to identify the frequency and location of filaments on the WIM, to study the statistics of their occurrence, and to compare the results from analysis of satellite and model-derived SST. Emphasis is placed on determining the preferred formation sites and the temporal evolution of the filaments. Their relation to bathymetric and coastal features, the wind field and the mesoscale eddy field is investigated. Special focus of the year 2002 is made in this chapter, although to have some

perspective of the following chapters, the results of the year 2009 are contained in the Appendix A.

The data used, the filament detection method, and the wind estimation are described in Section 2.2. Results are presented in Section 2.3, where model and satellite filament distribution are compared. The discussion of the results and the conclusions are developed in Section 2.4.

2.2 Data and Methods

2.2.1 Model

The modeled SST fields in this study were extracted from the daily averaged outputs of the WIc for the period of May to October of the years 2001 to 2010.

Validation of the SST obtained by this model configuration was performed with satisfactory results at the monthly scale and the domain scale (*Cordeiro-Pires*, 2013). Negative bias of SST (i.e. model cooler than observed) was registered in the coastal region, as is common to modeling results of upwelling systems (*Veitch et al.*, 2010). This model configuration was designed to reproduce the mesoscale and is expected to replicate the statistical properties of structure, distribution and variability of filaments realistically, as was demonstrated by *Marchesiello et al.* (2003) for the California Current. However, it is not expected to reproduce the eddy and filament field in phase with the real one.

2.2.2 Satellite Data

The filament detection methodology was applied to SST images of the same period, from satellite AVHRR products (presented in Section 1.3.2) for comparison with model results. The grid was remapped to the same grid as the WIc domain.

A visual inspection of the images was performed to exclude any fully obscured by clouds or by physically improbable patterns, such as banding. Images that showed any apparently correct SST field were retained, even if part of the image presented suspect patterns.

2.2.3 Filament Detection

Pixels with an SST gradient higher than 0.075 °C/km were marked on each daily SST image, in order to highlight frontal regions. The gradient threshold of 0.075 °C/km was

reached empirically in order to be able to detect as much frontal regions as possible. Lower threshold values would show too much noise-generated gradients masking the fronts.

The methodology used for filament cataloging was based on the procedure described by *Haynes et al.* (1993a). Filaments were visually detected, manually marking and recording the longitude and latitude of the extremities. The origin of a filament was determined by the latitude of its coastal extremity, while direction and length were computed using coordinates of both extremities. Only filaments originating along the western coastline, between Cape Finisterre and Cape São Vicente, were taken into account.

The origin of a filament was defined as the intersection of the axis of a cold water tongue with the coast. The offshore limit of a filament was defined through the intersection of the northern and southern sides of the previously detected horizontal SST gradient lines. When the orientation of the axis was not clear, some uncertainty occurred in deciding the position of the extremities. This uncertainty was minimized with some practical methods highlighted in Fig. 2.1. (1) Filaments where horizontal SST gradient does not converge to a point were marked on an expected area visible on the temperature field (Fig. 2.1 central and right panels, northern filaments). (2) The offshore part of a filament could be visible but the origin would not be detectable due to strong near-shore gradients (Fig. 2.1 central panel, northern filament). The origin was marked on the intersection of the approximated bisector between filament sides and the coast. (3) Many of the longer filaments had a curved form (Fig. 2.1 central panel, at 39°N) and representing their true form with two points is impossible. In this case, the extremities were marked in such a way as to maintain, as much as possible, the straight line connecting them between the lateral boundaries. This way the direction of the filaments is not biased by the curvature and their length is underestimated with respect to most studies, such as *Haynes et al.* (1993a) always considering the offshore extremity as the most distant point from the coast.

This procedure was repeated for the images from May to October in the years 2001 to 2010. Filament identification was made independently in different images. A total of 5352 filaments in the model and 2115 in the satellite SST images counted for the so-called full set of filaments detected on the Western Iberian Margin. To compare visually the patterns of filaments resulting from the analysis of the model and observed by the satellite, a filter was applied to both full sets of filaments. For each daily image, using the satellite data, cloud coverage percentage was calculated in 50 zonal bands between 36°N and 45°N. The filter consisted in removing filaments observed in zonal bands with cloud coverage higher than 50%. This process was repeated for all images, retaining 1885 model filaments and 1681 satellite filaments, hereafter referred to as the filtered set of filaments. A time vs latitude grid was created to present the temporal development of filament properties in

Section 2.3.2. The temporal axis is divided in intervals of 5 days length between days 120 (30 April) and 305 (1 November), and the latitudinal axis is divided in 50 equally spaced intervals between 36°N and 45°N.

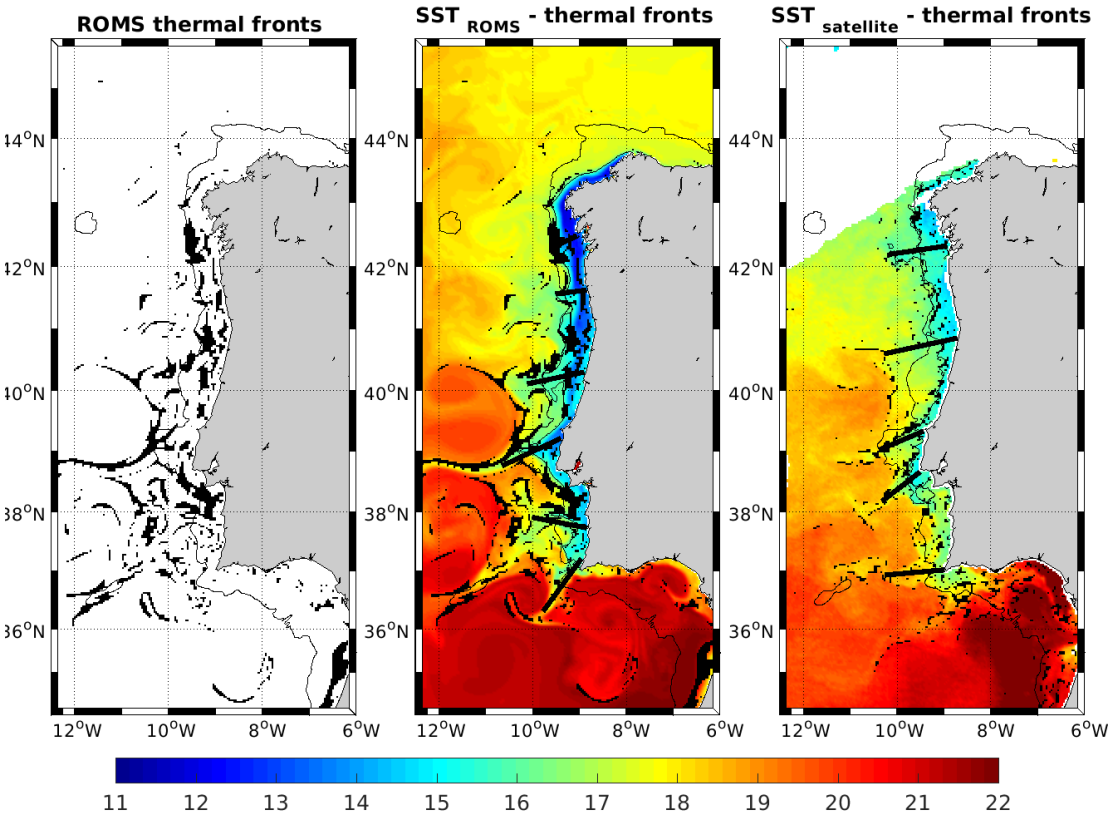

Figure 2.1: (left and central panel) Sea surface images on 17 July 2002 for the ROMS outputs and (right panel) satellite imagery. Black shading represents horizontal temperature gradients higher than 0.075 °C/km. On the central and right panels colored shading is the sea surface temperature and black thick lines extending from the coast are the filaments marked.

2.2.4 Wind Data

Surface winds, which drive the upwelling, were extracted from QuikSCAT and ASCAT databases (the same as the model winds forcing) for three 0.5° wide square coastal regions along the 9.5°W line, centered at 43°N, 40°N and 37.5°N, see Fig. 1.1.

Fig. 2.2 shows the 10 year mean of the daily meridional wind component on the 40°N square. The study period, in which the filament detection method was applied, is defined between days 121 and 304 (May 1^{st} to October 31^{st}), to include the summer upwelling

regime. The northerly wind intensity gradually increased until reaching ∼6 m/s around day 220 (early August), and decreased afterward until day 295 (22 October) turning southerly from day 290 (17 October). Superimposed on this mean pattern were 5 to 10 day fluctuations of mesoscale variability of the lower troposphere, generating anomalies such as two periods around days 126 (6 May) and 187 (6 July). The zonal wind component (not shown) was mostly directed eastward, decreasing from ∼2 m/s in May to ∼1 m/s in October with few oscillations.

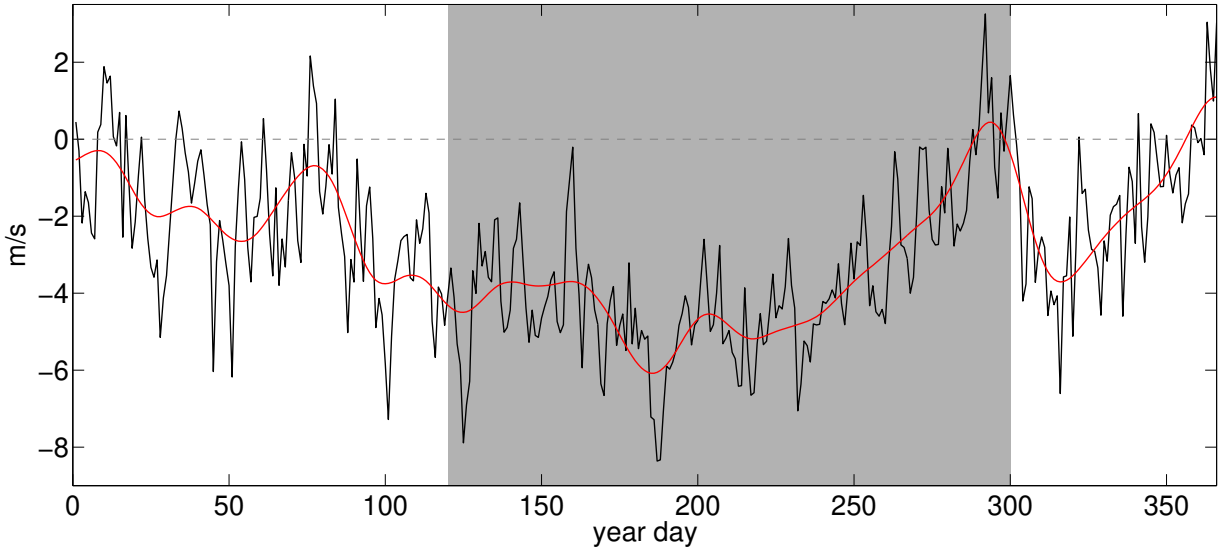

Figure 2.2: 10-year mean of the daily meridional wind component on the 40°N centered square starred in Fig. 1.1 (black line) and 30 days low-pass filtered (red line). Shaded area indicates the study period (days 121 to 304).

2.3 Results

2.3.1 Summer 2002

The distribution of filaments obtained from the satellite products and model output were analyzed for the years 2001-2010; as an example, the particular year of 2002 is examined. In order to perform a comparison between the satellite and the modeled filaments, both are filtered for the effect of clouds, and displayed in Fig. 2.3. The year 2002 was characterized by intense upwelling-favorable winds along the Western Iberian Margin. The upwelling-favorable periods frequently alternated with the passage of atmospheric fronts and cloudiness. The result was the intermittent availability of clear images with large

filaments. A low number of filament occurrences were registered in May and June, while during July and August filaments were detected along the entire western coast. From mid-September to late October images were mostly cloud covered, resulting in fewer observed filaments, except late-September north of 42°N. The filament patterns observed in the satellite and modeled images were similar, with two regions of distinct behavior separated by a latitude just north of Cape Carvoeiro (39.3°N). To the south, filaments were observed mostly near the capes and promontories that prevail in the region. To the north, the location of filaments was more variable. These filaments seemed to be shifting southward until early-August and northward afterwards.

The most evident differences between modeled and satellite filaments occur in June and July. One difference is the appearance of filaments in the 40°N region in the model field but not in satellite images. Additionally, filaments appeared near both Cape Roca (39°N) and Cape Carvoeiro (39.3°N) in satellite images but not in the model images. In this case, the model filaments in this latitude had a width similar to the length of the Estremadura Promontory between the two capes.

In spite of the differences, the modeling results permit a study of the filament field in the WIM using the full set of model filament occurrences. Results for the year 2002 (Fig. 2.4b) are compared with the temporal evolution of the coastal surface wind at the locations shown by stars in Fig. 1.1 (Fig. 2.4a). To find a connection between filaments and the underlying mesoscale eddies, the distribution of coastal eddies was represented over the filament distribution. The eddy field was obtained by applying an Eddy Detection Algorithm (*Nencioli et al.*, 2010) to the surface current field of the model outputs. Pairs of green and red lines in Fig. 2.4 bottom panel represent the eddies detected east of 11°W, in which green represents westward currents and red eastward currents.

During June and July, south of 40.5°N, filaments were associated with the main coastal features, around latitudes 37.2°N (Cape São Vicente), 38°N (Cape Sines), 39.2°N (Estremadura Promontory) and 40.2°N (Cape Mondego). North of 40.5°N filaments were initially located at 43°N, 42.5°N and 42°N, and gradually moved southward until the end of this period, merging into one filament on the 41°N to 42°N region as observed in the modeling study of *Røed and Shi* (1999). The wind was in general northerly, strengthening until late July, frequently interrupted by short periods of relaxation. This upwelling-favorable regime was responsible for the intensification of the surface equatorward flow. Since the northern coast and bathymetry are smoother, filaments initially generated north of 42°N were displaced southward in the sense of the equatorward flow without encountering major obstacles, again as found by *Røed and Shi* (1999). South of 40.5°N the interaction of the upwelling jet with the principal capes, promontories and canyons contributed to the

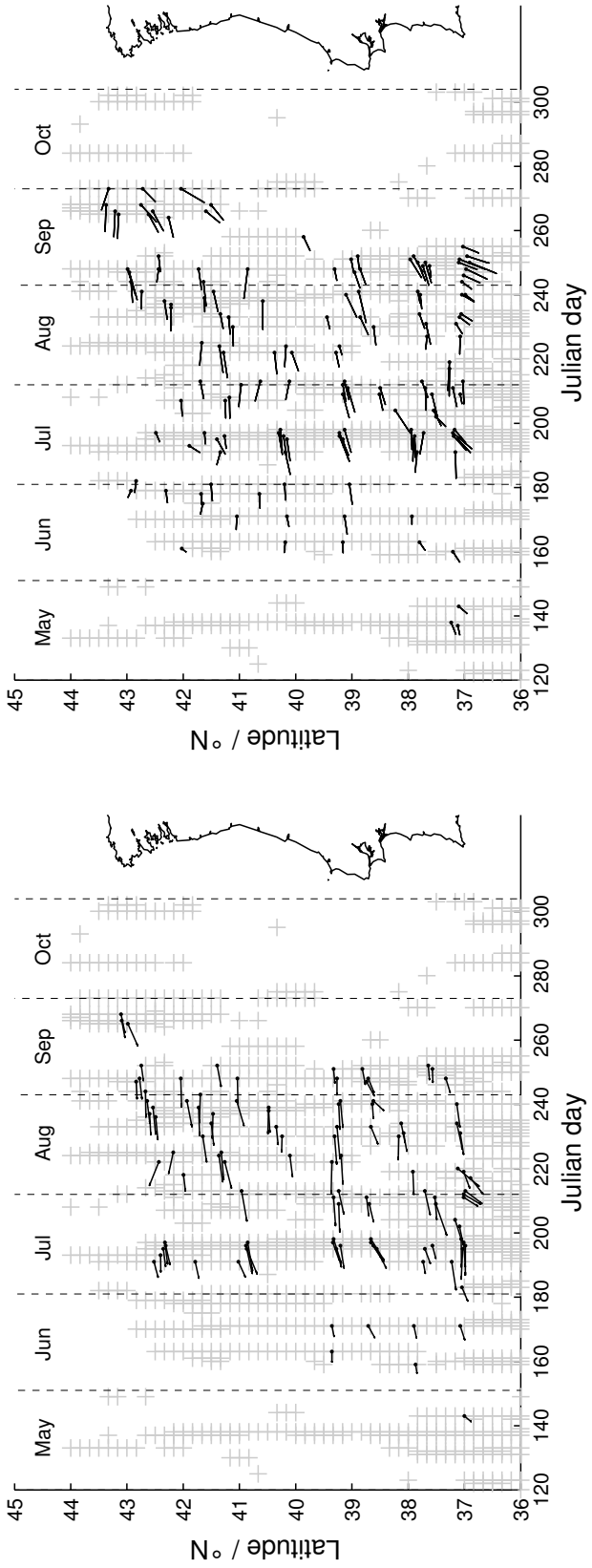

Figure 2.3: May to October 2002 time series of Filament length and direction (black lines) and latitude of their coastal origin (black dots), observed on zonal stripes with cloud coverage lower than 50% (gray plus signals), from (left) Satellite and (right) Model products.

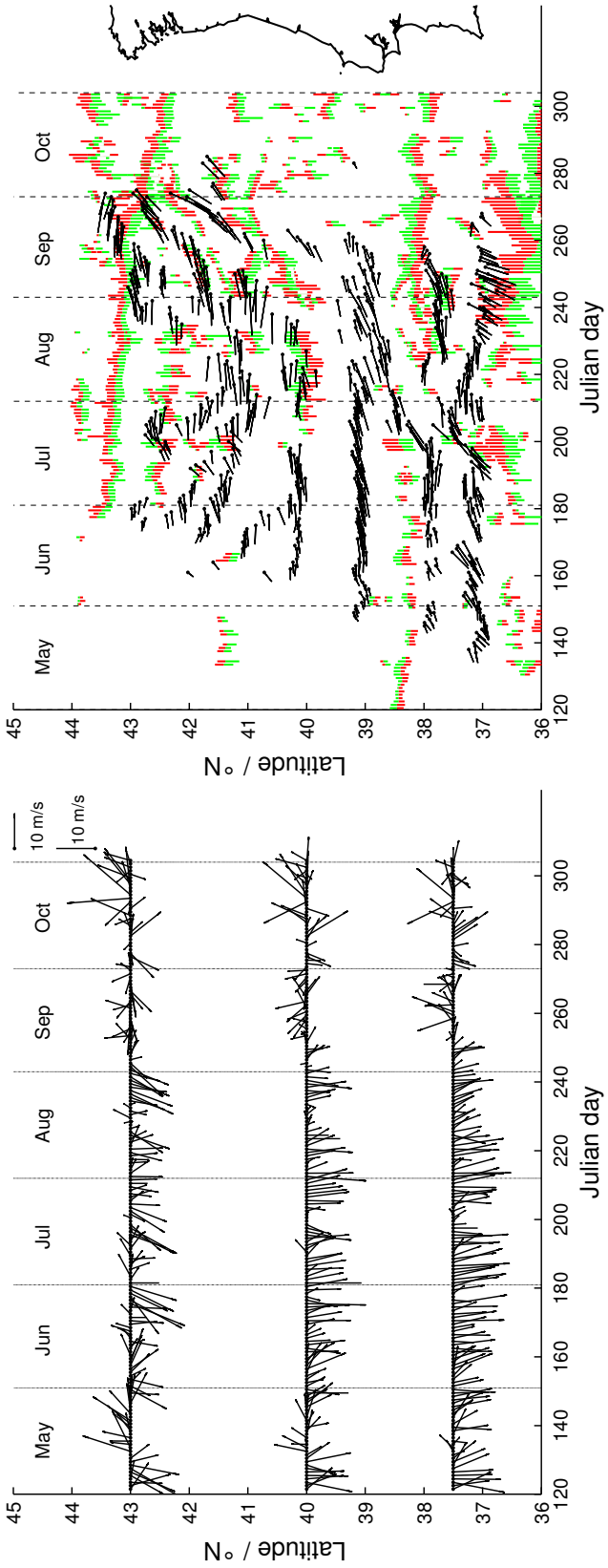

Figure 2.4: Time series from May to October 2002 of: (left) QuikSCAT wind speed and direction registered in three distinct latitudes at 9.5°W; (right) Filament length and direction (black lines) and latitude of their origin (black dots) on the coast, from the model product. Green (offshore current) and red (onshore current) colored lines show locations of eddies registered east of 11°W.

characteristic patterns near main bathymetric features.

Although a simple relationship between filament field and mesoscale eddy field is not always noticeable, it can be inferred by following the evolution of filaments and nearby eddies in Fig. 2.4. Generally the eddy field was not related with filament location and orientation in June and July. One exception was found near Cape Sines during a wind relaxation period around day 200 (19 July), in which the filament was located between an anticyclone at 38.5°N and a cyclone at 37.5°N. With the return of northerly winds, filaments previously situated at 37.2°N and 38°N moved northward to 37.5°N and 38.5°N respectively. In early August the southern filament gradually returned to its previous position, while the northern one migrated northward to merge with the 39°N filament in the Estremadura Promontory. Also during this relaxation period the filament located around 40.2°N disappeared. When the upwelling-favorable winds returned, this filament reappeared in association with a local coastal cyclone that developed during the relaxation period.

The August wind regime could be divided in three periods with approximately 10 day duration each. In the first period winds, were mostly strong northerlies that maintained the same filament patterns as in July; in the second, winds were relaxed; and in the third period, strong north-easterlies were found in the northern region while weaker northerlies occurred in the southern region. The relaxation period allowed stratification of the surface layers so that filaments weakened north of 40.5°N. To the south, filaments persisted in the vicinity of the Estremadura Promontory and Cape São Vicente. The formation of an anticyclone at 38°N was accompanied by a filament to the south. During the following upwelling-favorable period, after day 233 (21 of August), a new front was formed between coastal and offshore waters that quickly meandered and, after day 238 (26 August) evolved into two large filaments at 43°N and 41.8°N.

In September the wind weakened and its direction became mostly southerly, contributing to the onset of poleward flow over the slope typical of the time of year. After mid-September, south of 41°N, filaments were no longer observed while those further north were displaced northward under the influence of the poleward flow, until disappearing in early October. As the filaments were displaced in the northward direction, eddies were spun up as a result of instabilities between the warm offshore poleward flow and the cold near-shore equatorward flow. In late August/ early September between 36°N and 37°N a cyclone was situated east of 8.5°W inside the Gulf of Cádiz. Southward flow was generated at Cape São Vicente, coinciding with the southwestward direction of the filaments located at 37°N.

2.3.2 Annual Integrated Filament Distribution

The temporal and spatial distribution of the 10 year filament field was determined for the defined grid with 5 days spacing on the horizontal axis and 50 equally spaced intervals between 36°N and 44°N on the vertical axis. A comparison between filament distributions of satellite and model data sets is presented using the filaments filtered for clouds (Fig. 2.5). The filament occurrences in the model strongly resembled those in the satellite images and the patterns were similar to a typical year like 2002, as described above (Fig. 2.3). In both data sets, few occurrences were observed in May and June north of 39°N. From July until late September, filaments were more common along most of the coastline. Two regions where filaments were not observed by satellite and were seen rarely in the modeled fields were the neighborhoods of 39.7°N, and 38.3°N. Regions with more regular filament occurrences were located near Capes Finisterre, Carvoeiro, Sines and São Vicente. The differences between model and satellite results documented in the case of the year 2002 extend to the full study period. The model fields presented filaments in the 40°N to 40.5°N region all summer, while in the satellite images fewer filaments were observed and only in August and September. The presence of the Cape Sines filament was underestimated in the model, replicating the year 2002 situation, in which a wide filament extended along the Estremadura promontory.

Bearing in mind the performance of the filtered model in comparison with the observations, filament distribution, length and angle were further analyzed using the full set of filaments from the model. In Fig. 2.6 the distribution of the full set of model filaments is illustrated in the time-latitude grid presented previously. The number of filaments identified in the 10 year simulation for the study period (May-October) was integrated according to time (Fig. 2.6 top panel) and latitude (Fig. 2.6 right panel).

Filament occurrences gradually increased until reaching a constant level in early July that lasted until mid-September when occurrences decreased sharply. As expected, the central period accounted for as much as 75% of all filament occurrences, coinciding with the peak of the upwelling season.

The distribution with latitude was dominated by the presence of regions with peaks representing localized high number of occurrences. From north to south, the peaks were located near Cape Finisterre (42.9°N), Vigo (41.9°N), Porto (41°N), Cape Mondego (40.3°N), Estremadura Promontory (39°N), Cape Sines (37.8°N) and Cape São Vicente (37.1°N). The highest peak, at 39°N with almost 12% of occurrences, was associated with wide filaments frequently occupying the Estremadura Promontory, oscillating between Cape Carvoeiro and Cape Roca (*Oliveira et al.*, 2009). Occurrences of these filaments and the ones near

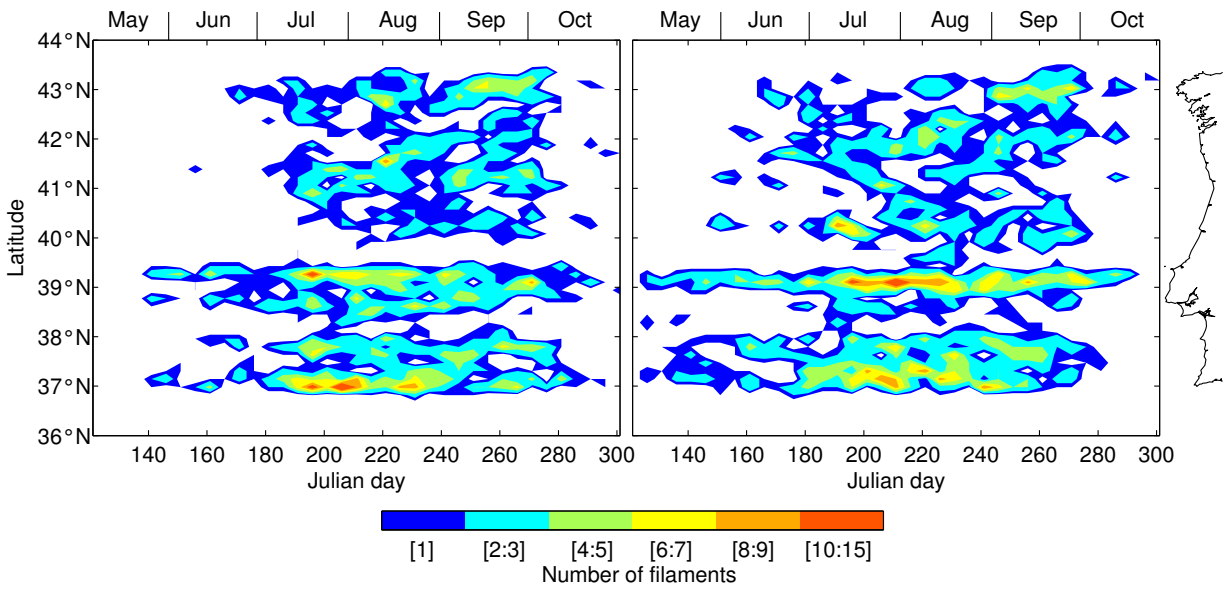

Figure 2.5: Distribution of the number of filaments observed in zonal stripes with cloud coverage under 50% in the study years, from (left) satellite and (right) model products. The data are divided in 5 days interval and equally spaced latitude intervals between 36°N and 44°N.

the southern capes were observed throughout most of the upwelling seasons, developing in May and extending to end of September with few interruptions. North of the Estremadura Promontory, in most summers filaments did not start to develop until June. The occurrences near Cape Finisterre are concentrated more in September, while near Cape Mondego occurrences remain roughly constant from June to September. The relative maximums near Vigo and Porto are the least localized, indicative of the high mobility of the filament occurrences in the 40.5°N to 42.5°N area.

The mean lengths of the filaments observed in the 10 year simulation (Fig. 2.7) increased through the summer, reaching a plateau at roughly the same period as the number of filaments. Integrated according to latitude (Fig. 2.7 right panel) the filament lengths varied between 70 km and 90 km. In regions where filament occurrences were frequent in May and October this value is biased by the shorter filaments, specifically at Estremadura Promontory, Cape Sines and Cape São Vicente. Also, regions with lengthy filaments were not associated with the peaks of high number of filament occurrences. In the central panel of Fig. 2.7 five regions of higher filament lengths are evident, namely between Cape Finisterre and Vigo, between Vigo and Porto, between Aveiro Canyon and Cape Carvoeiro, off Estremadura Promontory and between Cape Sines and Cape São Vicente. The filament number as function of the length was calculated (not shown). The filament length varies

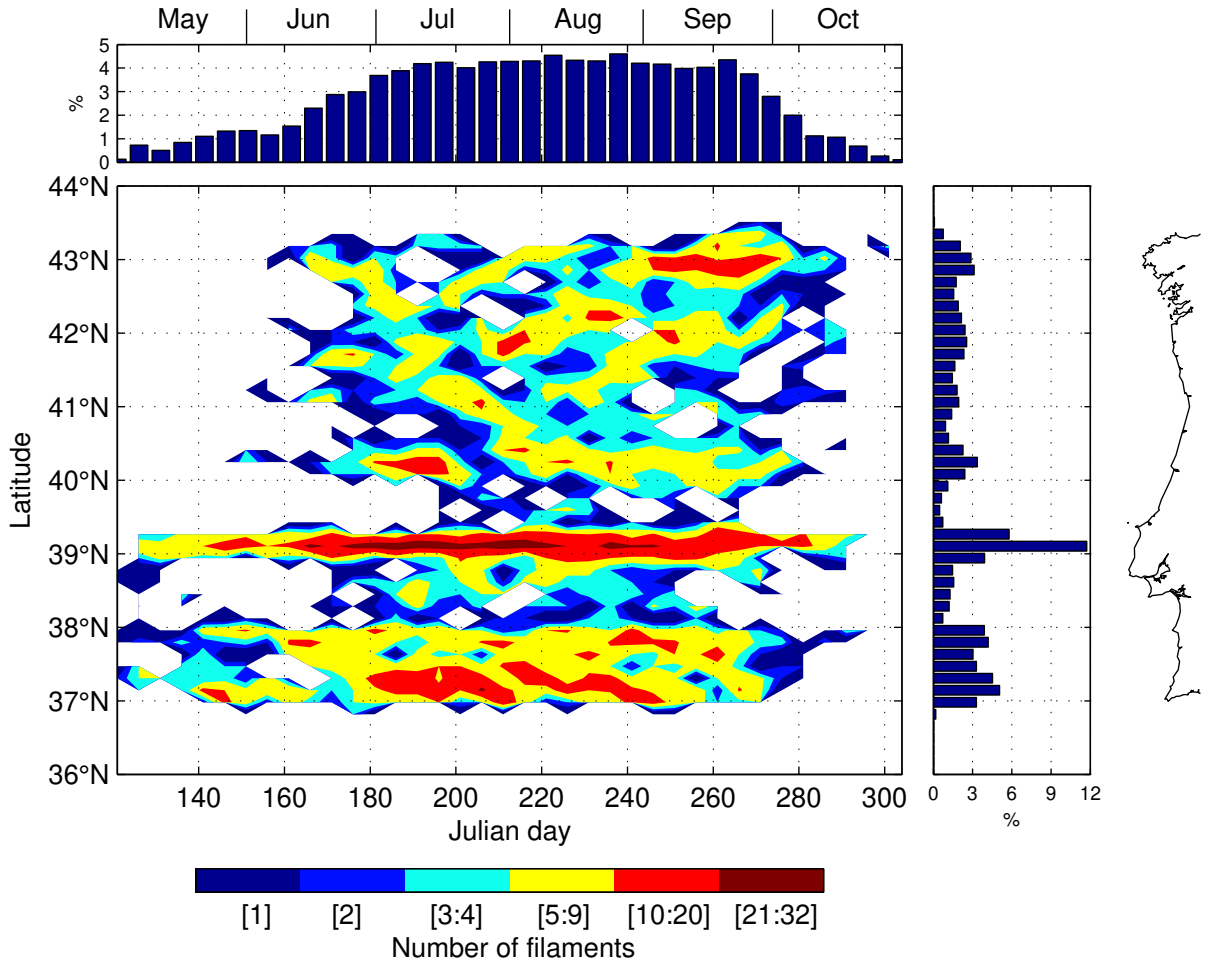

Figure 2.6: Number of filament observations each 5 days in 50 latitude boxes between 36°N and 44°N, for the 10 years model simulation. Bar graphs represent percentage of filaments integrated (top) for each 5 day interval and (right) for each latitude interval.

between 20 km and 200 km, with only a few filaments longer than (1.7%) 150 km. The most frequent length (27%) is between 60 and 80 km.

The angle between the axis of each filament and the east-west direction was determined, in order to evaluate the prevailing orientation of filaments (Fig. 2.8). Positive (negative) angles represent filaments oriented toward the NW (SW) quadrant; thus, an angle of zero represent a filament directed exactly westward.

Three regions of the WIM can be distinguished based on the angle distribution (Fig. 2.8 right panel): southern, central and northern. The angle of filaments in the southern region (south of 39.5°N) were mostly negative, directed southwestward, with two peaks immediately south of Cape Roca and Cape São Vicente of approximately -40°. In the central

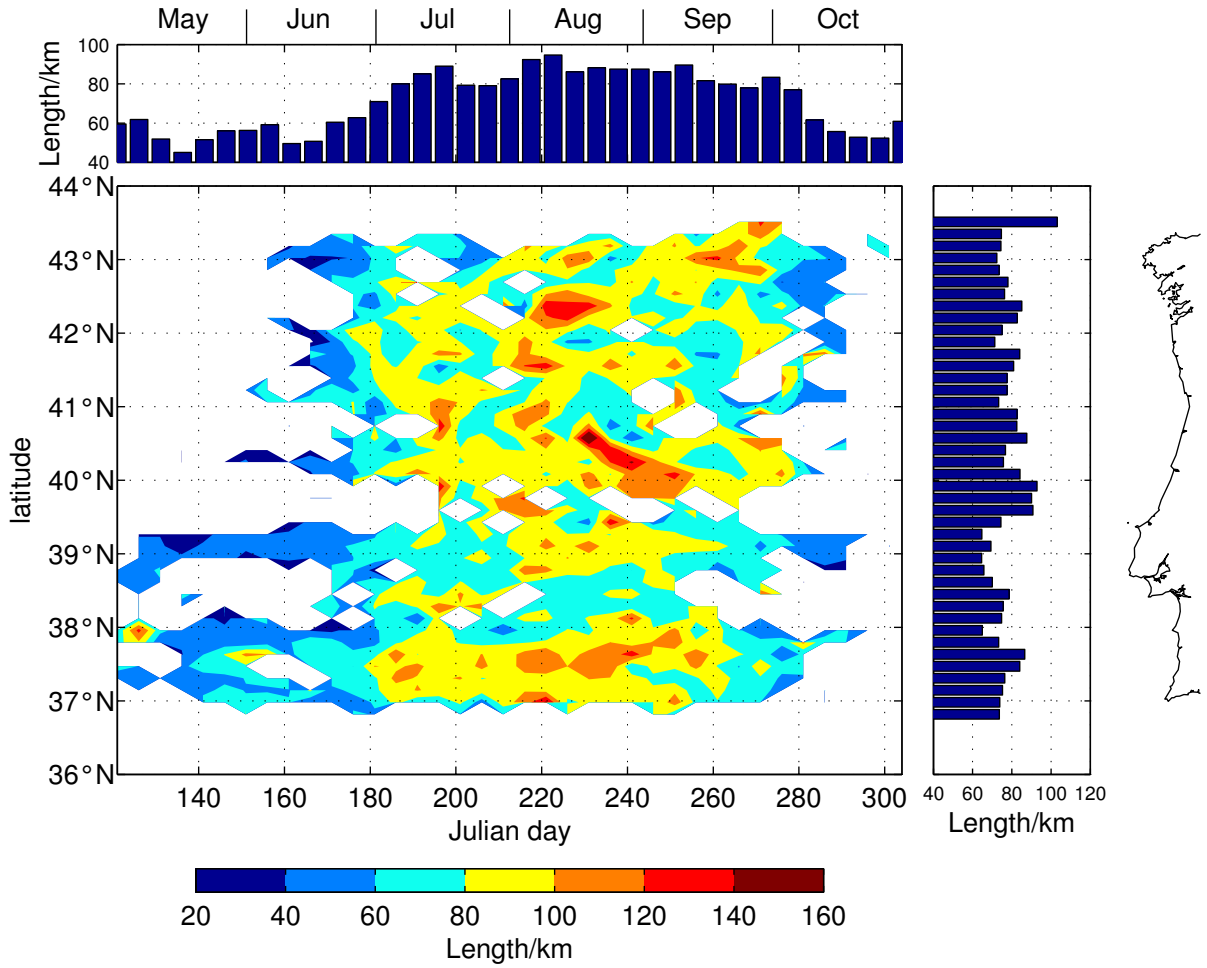

Figure 2.7: Mean length of filaments (km) observed each 5 days in 50 latitude boxes between 36°N and 44°N, for the 10 years model simulation. Bar graphs represent mean length of filaments integrated (top) for each 5 day interval and (right) for each latitude interval.

region (between 39.5°N and 43°N) the angles were also negative but closer to zero, since filaments were mostly directed southwestward and westward, with some directed northwestward. In the northern region (north of 43°N), where the orientation of the coastline shifts to a NE-SW direction, the filaments were mostly directed northwestward.

The angles were generally around -20° (Fig. 2.8 top panel) evidencing the tendency for southwestward directed filaments. With the exception of the months of May and June, which are dominated by filaments in the south region with few observations, the filaments turned increasingly southward until the beginning of October. After the upwelling period, in late October, filament occurrences were restricted to north of Cape Finisterre, where

their direction was mainly northwestward, hence the positive mean angle in the closing days of October.

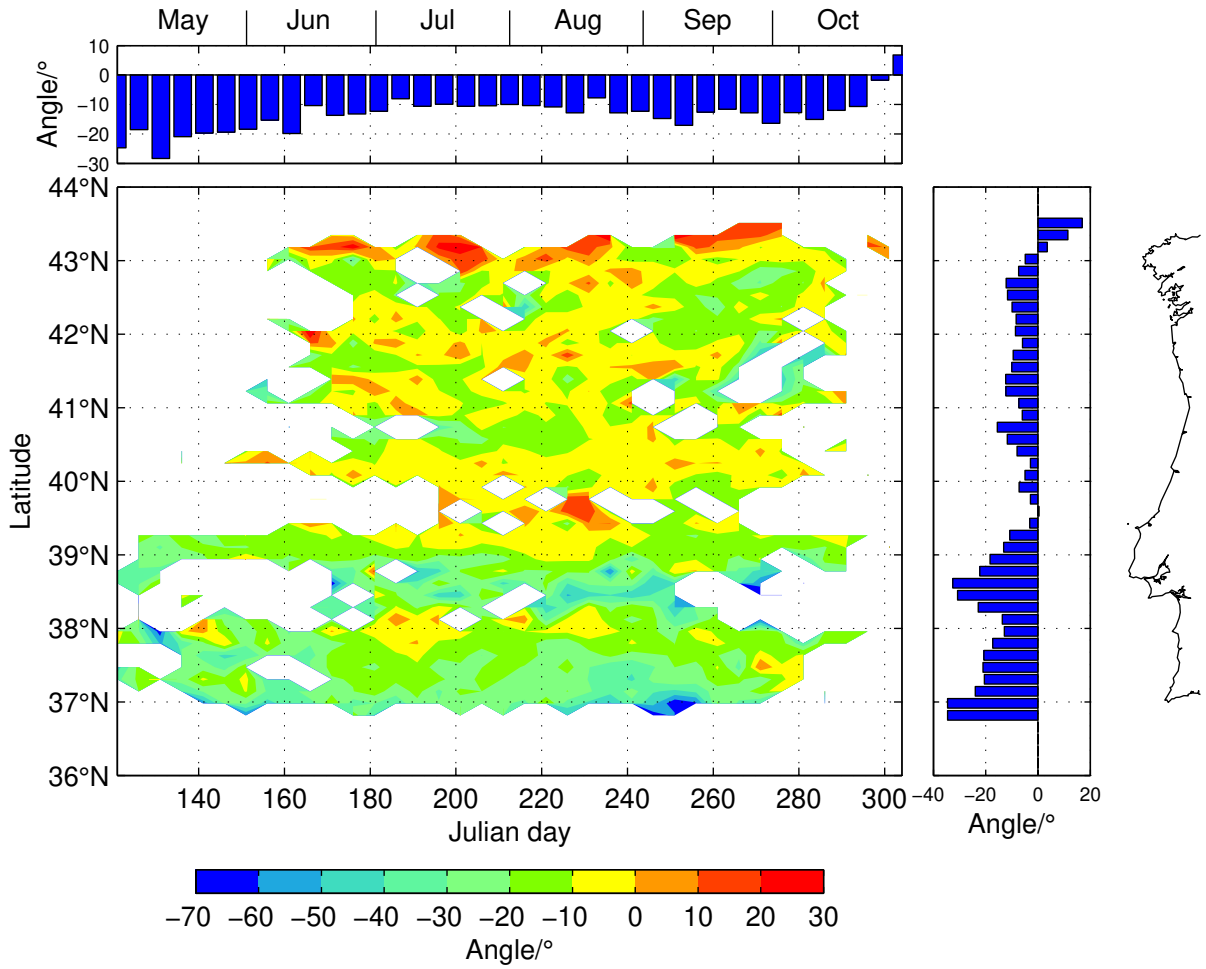

Figure 2.8: Mean angle filaments make with a westward line at the filament, observed each 5 days in 50 latitude boxes between 36°N and 44°N, for the 10 years model simulation. Bar graphs represent mean sine of the angles integrated (top) for each 5 day interval and (right) for each latitude interval. A negative angle indicates southwestward direction and positive is northwestward.

2.3.3 Interannual Variability of Filament Distribution

The interannual variability of filament distributions was examined by comparing the monthly number of filaments with the alongshore wind intensity Fig. 2.9. The monthly number of filaments was calculated for two regions with distinct filament patterns, separated at 40°N.

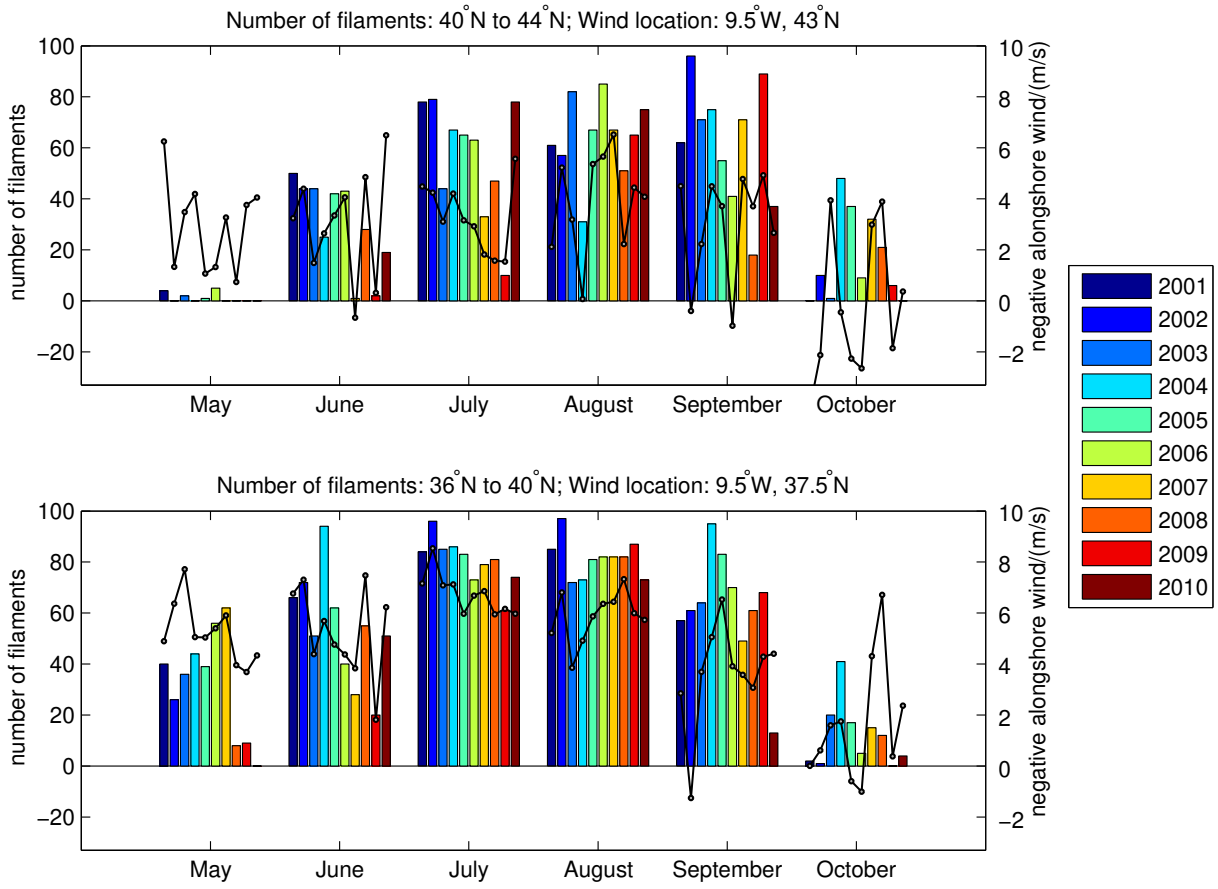

Figure 2.9: Monthly and yearly integrated number of filaments (bar graphs) and negative of the monthly means of alongshore winds (*circles*) on (top panel) the northern region and (bottom panel) the southern region. Positive (Negative) values mean northerly (southerly) winds.

The number of filament occurrences and wind strength was generally lower in the northern region, and filaments were most common in August and September, while in the southern region they were most frequent in July and August. The interannual variability of monthly filaments was generally higher in the northern region than in the southern one.

In the northern region some years did not present filaments in May and the others were weak. For June and October the same occurred but with more number of filaments. For the remaining months, a high number of filaments was present in 2002 (June and September), 2009 (August and September), 2010 (July and August), 2006 (August), 2001 (July). Fewer filaments were observed in 2009 (July), 2007 (July), 2008 (September), 2004 (August).

In the southern region some years did not present filaments in May and October while others presented few filaments. In May, number of filaments was considerably higher than

in the northern region. In June and September filaments were observed for all years, although with relatively high interannual variability, e.g. in 2004 filament numbers were on the order of the top monthly occurrences (>80 filaments/month), while September 2010 and June 2009 presented <20 filaments/month. In July and August, filament occurrences were higher than 60 filaments/month, with 2002 presenting the greatest number of filaments in both months. The interannual variability of these months was significantly lower than any other in the southern region and than all months on the northern region.

In May and October less relationship between filament number and alongshore wind was found, possibly because the number of occurrences was low. In the months with most occurrences (June, July, August and September) the number of filaments followed trends similar to the intensity of alongshore winds. With stronger monthly northerly winds, more filaments were observed, except in September 2002, which had numerous filaments despite southerly winds. This was the only month when filament number was relatively high and mean monthly winds were southerly.

The explanation of this anomalous behavior in September 2002 is evident in Fig. 2.4. Strong northerly wind from late August to 10 September generated several persistent filaments along the WIM. After that date, wind was variable in the northern region, and southerly in the southern region. Consequently, filaments maintained their identity throughout the northern region, but disappeared in the second half of September in the southern region.

2.3.4 Filament Distribution in a Climatological Simulation

In order to evaluate the dependence of the wind variability on the filament field, the filament detection method was also applied to the results of a climatological model simulation (*Nolasco et al.*, 2013a). The surface fluxes were obtained from the Comprehensive Ocean–Atmosphere Data Set (COADS; *da Silva et al.* 1994), which consisted in monthly climatological wind and heat fluxes without interannual variability, run through nine consecutive years. For filament detection, images of 3-day averages of SST were produced from the years six to nine of the simulation.

The temporal and spatial distribution of the 4 year filament field was analyzed, as in Fig. 2.6, on a grid spaced at 12 days on the horizontal axis and in 50 equal intervals between 36°N and 44°N on the vertical axis. The distribution of the filaments is illustrated in this time-latitude grid (Fig. 2.10) with temporal integration (top panel) and latitudinal integration (right panel). The evolution of filament number through the climatological summer was characterized by an increase of occurrences in May and June, a maximum in

July, a high number in August, and decreasing numbers in September and October.

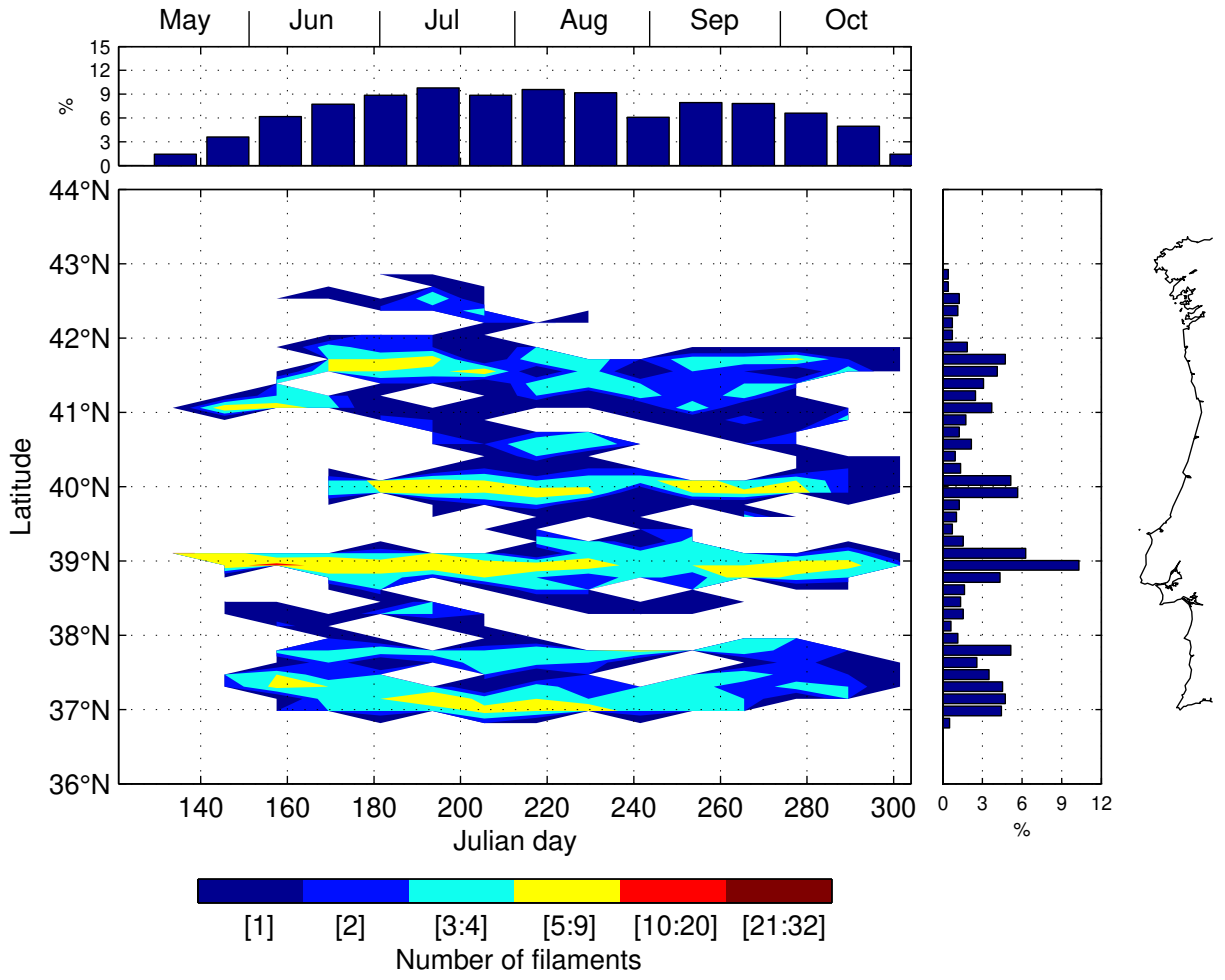

Figure 2.10: Number of filament observations each 12 days in 50 latitude boxes between 36°N and 44°N, for 4 years of the climatological simulation. Bar graphs represent percentage of filaments integrated (top) for each 12 day interval and (right) for each latitude interval.

The main regions for filament occurrences were located between Vigo and Porto, near Cape Mondego, off the Estremadura Promontory region near Cape Sines and off Cape São Vicente. These regions presented filaments during most of the May to October period. North of Vigo some filaments were registered in June and July but were not present after August. By direct inspection of the SST field (not shown) and from Fig. 2.10, filaments north of Cape Mondego were displaced southward between June and August, as seen in the slope of the distribution of number of filaments.

2.4 Discussion and Conclusions

The field of upwelling filaments generated in a numerical model of the WIM was analyzed and compared to a database of satellite images for the common period 2001-2010, using methods similar to the *Haynes et al.* (1993a) study of the period 1982-1990. The results from both periods and studies are similar in that filament generation over the WIM is associated with periods of fully developed upwelling, occurring every summer mainly during July and August. Filaments are generated along most of the WIM with different patterns in distinct regions. In the region between Nazaré Canyon (40°N) and Bay of Biscay, filaments are concentrated in the neighborhood of Cape Finisterre (43°N), Vigo (42°N), Porto (41°N) and Cape Mondego (40.3°N). The filaments associated with Cape Finisterre and Cape Mondego frequently remain anchored to these capes. The region between these capes has a relatively straight bathymetry, although several submarine canyons exist (Porto and Aveiro canyons, see Fig. 1.1). In this region, there is evidence (*Peliz et al.*, 2002) that the poleward flow offshore (and its mesoscale features) interacts with equatorward flow on the shelf, generating horizontal shears, and hence instabilities, evolving into filaments. The occurrences off Vigo and Porto are related with filaments that move appreciably alongshore around those latitudes. In general these filaments are displaced southward during June and July and northward in August, September and October. The southward displacement might be related to the general strengthening of the equatorward flow at the beginning of the upwelling season. In September and October filaments are usually advected northward by the presence of the Iberian Poleward Current until the coastal cold SST signature of upwelling is overrun by the warmer oceanic surface water.

In the region between 39.5°N and 40°N few filaments were found in either satellite or model fields. This lack of filament generation might be related to a predominantly anticyclonic circulation in the region north of the Estremadura Promontory, associated with the separation of the Mediterranean Water vein at depth from the Estremadura Promontory (*Nolasco et al.*, 2013a).

Further south on the same promontory both Cape Carvoeiro and Cape Roca give rise to separate filaments that frequently merge together. This situation occurs more commonly in the model, where it results in underestimation of the Cape Roca filament occurrences (Fig. 2.5). Near Cape Roca, filaments with strong southward component can be a consequence of overshooting of the equatorward upwelling jet, as suggested by *Relvas and Barton* (2005), for the similar case of Cape São Vicente. This occurrence frequently shelters the region south of it, such as in Monterey Bay in the California Current (*Graham et al.*, 1992). This is also observed south of the Estremadura Promontory (*Moita et al.*,

2003), at the Setubal canyon region, where filaments are rare.

From Cape Sines to Cape São Vicente a high number of filaments is observed with most occurrences at or near these capes. Filaments are mostly located downstream of Cape Sines and upstream of Cape São Vicente, but have a tendency to migrate and merge between both locations. These filaments usually have a SW direction and, in the case of Cape São Vicente, filaments can have a stronger southward component associated with periods of cyclonic circulation generated in the southern margin near the cape.

Studies in other Eastern Boundary regions have also concluded that the most extended and predominant filaments are associated with the major capes and ridges. South of Iberia in the Canary Upwelling System major filaments are frequently associated with the Cape Ghir plateau (*Troupin et al.*, 2012). Further south still at 20°N filaments were identified near Cape Blanc, where *Meunier et al.* (2012) report on the relation between filament structure, eddies and bathymetry. *A.G. Kostianoy and A.G. Zatsepin* (1996) reported on filaments off both NW Africa and in the SW African region in the Benguela Upwelling System. In the latter system no relation between filament location and coastal features was observed. In the California Current System, where upwelling filaments were first identified (*Breaker and Gilliland*, 1981), between Cape Blanco and Point Conception, upwelling filaments, of lengths up to 300 km, are associated with the main coastal features (*Flament et al.*, 1985; *Strub et al.*, 1991).

In the Northeastern Atlantic upwelling system between 15° and 20°N the upwelling season occurs in winter/spring while north of 20°N it occurs progressively later with increasing latitude, occurring in summer in the WIM. The temporal evolution of the filament field through the May to October period starts with the development of small structures mainly anchored to the capes south of 40°N. As the upwelling season progresses, filaments grow and develop in most of the preferred sites named above. At the end of the upwelling season the number of filaments decreases as the upwelling-favorable winds decrease and the upwelling jet slows. Filaments are rarely observed along the WIM after the onset of northward surface flow in the Iberian Poleward Current over the slope region (*Relvas et al.*, 2007).

In *Haynes et al.* (1993a) filaments had systematically greater lengths and were found in narrower location ranges than IN this study. These differences are partly related to the subjectivity inherent in this kind of studies, and to small differences in methodology. While *Haynes et al.* (1993a) based their analysis on individually contrast-enhanced, gray-scale images supplied as prints by the UK Dundee Remote Sensing service, the present study used standard downloaded color-coded image products from EUMETSAT Ocean & Sea Ice Satellite Application Facility. The different definition of the filament termination

used in this study (see Section 2.2.3), resulted in underestimation of about 40 km in the mean filament length (from 120 km in *Haynes et al.* (1993a) to 80 km here). This underestimation occurs, since in this study, the offshore filament termination was marked as the point where the northern and southern boundaries of the filament converge, even if it extends visually further from this point. On the other hand, marking pixels with high SST gradients allowed more precise positioning of the filament origin at the coast. Despite the above apparent differences in results between the two studies, the main filament locations reported here for 2001-2010 and found by *Haynes et al.* (1993a) for 1982 to 1990 are remarkably similar. Nevertheless, while those authors found the maximum number and length of filaments occurred in September, here it is found that the months of July to September all have equally high occurrence and maximal length.

In the WIM northerly winds largely control the upwelling intensity (*Fiúza et al.*, 1982) and consequently filament distribution. This relation is especially strong in July and August, in which months the years with most (fewest) filament occurrences were the ones with most (least) upwelling-favorable wind. Considering the relation between filament occurrences and northerly winds, at 40°N the WIM is separated into two distinct regions. Filaments mainly develop earlier and are more abundant in the southern region than in the northern region. The greater strength of northerly winds in the southern region lends support to the idea that upwelling-favorable wind is the main controlling factor in the development of filaments.

The number of filaments showed interannual variability, for example in the month of September, filament occurrences ranged between 20 and 90. Regionally the interannual variability was greater in the northern sector, than in the south, and related to the variability of the wind. It was also evident that the number of filaments was more consistent between years in the peak months of filament production, July and August.

Results of modeling under climatological wind forcing indicated that, in some latitudes, the integrated filament distribution differed from the 10 year realistic simulation. As opposed to the interannual case, north of Vigo filaments rarely developed. This can be explained by the climatological wind field which is almost purely northerly, while real winds are mainly northeasterly or northwesterly. The former causes upwelling north of Cape Finisterre as reported by *Torres et al.* (2003). Consequently upwelling in the neighborhood of Cape Finisterre is not well resolved, giving rise to a warmer temperature anomaly in the climatological simulation as discussed in *Nolasco et al.* (2013a).

It is difficult to make a full quantitative analysis of the interaction of filaments with the eddy field because the location, size, strength and sense of rotation of eddies all have a particular effect in individual eddy-filament relations. Nevertheless, the model simulation

provided some examples of eddy-filament interactions in which the most important effects occurred during periods of wind relaxation when wind-driven currents are weaker, a situation that frequently occurs in late summer. The question of eddy-filament interactions deserves further dedicated investigation in this region.

In summary, a model simulation during a ten year period was shown to be an efficient tool to study in a realistic way the filament field at the Western Iberian Margin. The main results of this study are:

- Filament fields estimated with SST images, from the model and the satellite products, compare well with each other.
- The results show that filament development was very similar to that described by *Haynes et al.* (1993a) for a period of two decades earlier.
- The preferential locations of filaments are associated with topographic irregularities (capes and promontories), or to instabilities likely associated with horizontal shear between equatorward upwelling flow and poleward flow offshore.
- Latitude 40°N marks a separation between a northern filament region of weaker winds resulting in fewer filaments of variable position and oriented generally southwest, and a southern one of stronger upwelling-favorable winds, where filaments are more abundant, more anchored to coastal features, and slightly more southward.
- Significant interannual variability in the number of filaments is observed throughout the upwelling season, but least in July and August, and is stronger in the northern region than the southern one.
- A good representation of the wind field is important for retrieving realistic filament distributions, as shown by the failure of the climatological simulation to reproduce filaments in key regions where their presence is consistently observed.

Chapter 3

Transient Response of Upwelling Onset

The contents of this chapter have been published in *Cordeiro et al.* (2018).

3.1 Introduction

In the previous chapter, the distribution of mesoscale features typical of the upwelling season was analyzed for all the WIM. The mechanisms of filament formation on the WIM have been more or less described by several authors (*Haynes et al.*, 1993a; *Røed and Shi*, 1999; *Relvas et al.*, 2007; *Meunier et al.*, 2010). The main filaments on the WIM are formed either through instabilities of the upwelling jet over ridges and coastal features (Estremadura Promontory) or the offshoot of the upwelling jet through 90° angled capes (Finisterre and São Vicente). On the relatively smooth shelf between Porto (41°N) and cape Silleiro (42.1°N) filaments were also observed, although the mechanism responsible for their formation remains controversial. One step onto the understanding of filament origin is done through the knowledge of the shelf circulation on the initial stages of filament formation. The oceanographic survey of July 2009, aboard the RV *Sarmiento de Gamboa*, contributed with observations of the inception of upwelling in the NW Iberian peninsula shelf between cape Silleiro and Porto.

In this chapter, the shelf circulation is presented in response to the atmospheric forcing over a sequence of upwelling and relaxation cycles. The presence of the Iberian Poleward current in the slope and shelf during the upwelling season is also discussed. In Section 3.2 are presented the data from the cruise and auxiliary observations. The main results of the July 2009 cruise are presented in Section 3.3 and discussed in Section 3.4. The conclusions were drawn in Section 3.5 in which a proposal for a scheme of the observed circulation was drawn.

3.2 Data and Methods

The cruise from which transects were made, took place from 7 to 23 July 2009 (Fig 3.1), which was described in Section 1.3.1. The zonally oriented transects of salinity, temperature, plus alongshelf and across-shelf currents are analyzed in this chapter, and are ordered chronologically from 1 to 9 in Fig 3.1b.

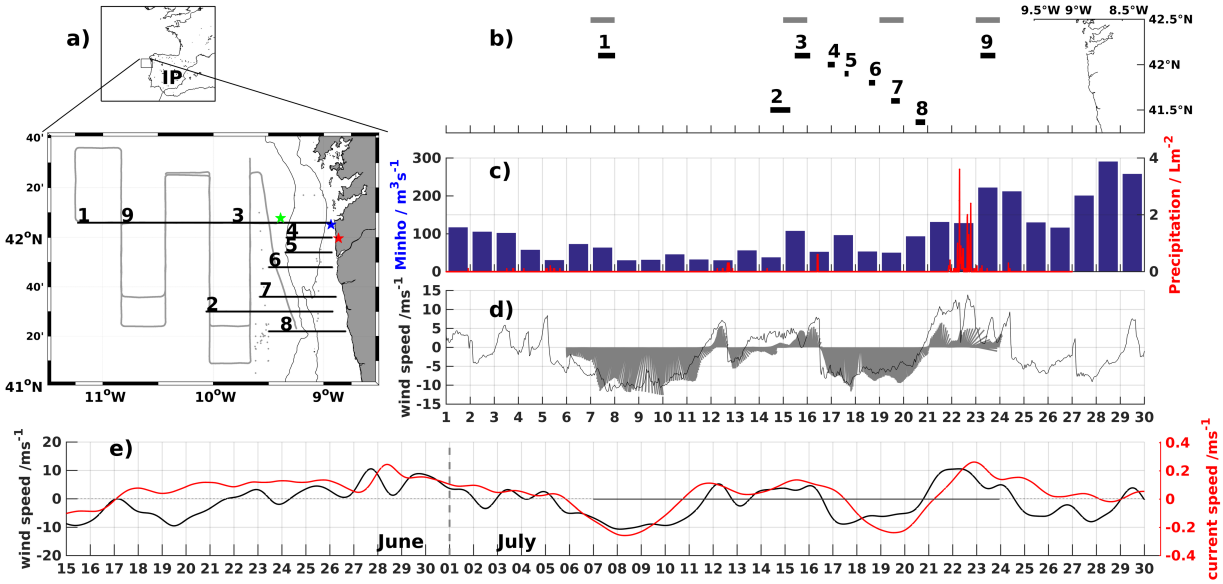

Figure 3.1: **Location and time of observations** a) Study area, with gray line representing the SeaSoar path and gray dots the CTD stations. Zonal CTD transect (black lines) numbers 1 to 9 are indicated at their western end. Stars represent the position of *Puertos del Estado* Buoy (green), moored ADCP (blue) and Castro Vicaludo meteorological station (red). IP labels the Iberian Peninsula. The 100-m and 200-m bathymetric are shown in dark thin lines. b) Time-series with latitude of the numbered transects (black lines) and indication of the day of the satellite image (gray lines). c) precipitation at Castro Vicaludo Meteorological station and river Minho outflow, d) Hourly meridional winds from WRF simulation at the moored ADCP location and stick plot of filtered winds registered on the research vessel meteorologic station. e) 33-hour filtered meridional winds from WRF simulation and barotropic meridional currents from the moored ADCP.

The zonal transects number 4 to 8 were performed to follow the path of the drogued buoy (red line in Fig. 3.2c) in succession from north (42°N) to south (41.4°N), covering the continental shelf. This sampling methodology was designed to follow approximately the same water parcel during the upwelling event described below.

Transects number 1, 3 and 9 were made in front of Cape Silleiro, on 7 July, 15 July

and 23 July respectively (Fig 3.1b). Transects 1 and 9 included 7 stations on the shelf and were continuous with the offshore zonal SeaSoar transect. Transect 1 extended to 11.25°W and transect 9 to 10.83°W. Transect 3 had 11 CTD stations between 9.45°W and the coast. Transect number 2 was made on day 14 and was located at 41.5 °N, between 10.07°N and the coast.

The evolution of the depth-averaged alongshore currents during the period of the cruise was obtained from the mADCP located in front of cape Silleiro (presented in Section 1.3.1).

Precipitation measured every 10 minutes at the Castro Vicaludo meteorogical station was provided by MeteoGalicia located at 8.86°W, 41.99°N (green star in Fig 3.2). Hourly wind speed and direction at 10 m above sea surface from the WRF configuration described in Section 1.4.4.

SST maps were retrieved for the days 7, 15, 19 and 23 July from the AVHRR dataset

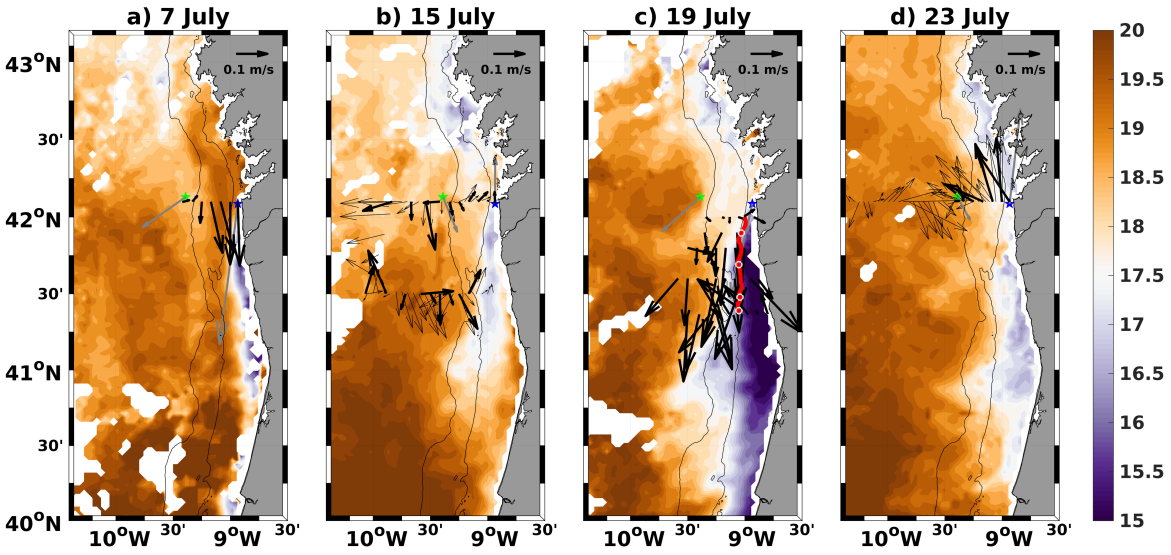

Figure 3.2: **Maps of the SST from AVHRR satellite data** on the days marked in Fig 3.1b, with instantaneous currents measured along the research vessel path from lADCP (bold arrows) and vmADCP (thin arrows), when available, between 50 m and 80 m depths. The 100 m and 200 m bathymetry are represented in black. Moored ADCP and the *Puertos del Estado* Buoy are located at the dark blue and green stars respectively. Mean currents for each day at 10 m depth from the moored ADCP and 3 m depth from the *Puertos del Estado* Buoy are represented by gray arrows. On panel c), the currents correspond to the period from 17 to 20 July, and a red line shows the trajectory of a surface drifting buoy (starting in the north), with white circles marking its location at 00h00 of each day (vmADCP data was omitted here for better visualization).

(Section 1.3.2), marked with gray lines in Fig 3.1b. These four days are representative of the oceanographic conditions during the hydrographic transects with maximum possible image availability.

3.3 Results

3.3.1 General Cruise Conditions

Four distinct periods of wind forcing were identified during the cruise (Fig 3.1d). Between 5 and 11 July, an upwelling period was observed with northerly winds gradually strengthening to about 10 m/s on 8 July. On 11 July the wind weakened and shifted to a westerly direction, changing to a southerly direction on 12 July, at the start of a relaxation period with weak variable winds. This period lasted until mid 16 July, when the wind reverted from southerly to northerly, starting the second upwelling period. During this period, wind strength rapidly reached near 10 m/s, where it remained until late 19 July, when it started to weaken again. On 21 July, winds shifted to southerlies, peaking at almost 15 m/s on 22 July in the WRF record. On this day high precipitation rates were registered (accumulating 35 Lm^{-2} on 22 July) and the daily mean river Minho outflow was higher than 150 $m^3 s^{-1}$(Fig 3.1c).

Fig 3.1e shows the low-pass filtered alongshore component of the sub-inertial currents and wind for the second half of June and July at the moored ADCP location. Weak and variable winds prevailed in the weeks preceding the study period, while the shelf flow was poleward with currents between 0.1 m/s and 0.2 m/s. During the first and second upwelling periods the current became equatorward within a few hours, in response to the northerly wind, with maximum alongshore current of about -0.2 m/s. During the southerly wind event starting 21 July, poleward flow velocities were recorded by the mADCP by 23 July. For the period depicted in Fig 3.1e, alongshore wind and current components were significantly correlated (R=0.62,p=0) with wind leading current by 12h.

A synoptic view of the circulation regime can be seen in a combination of satellite images and currents on the shelf, measured by the vmADCP and mADCP on Fig 3.2. The early stage of the first upwelling period (5 to 11 July) is shown in Fig 3.2a where a developing equatorward flow and the first stage of outcropping of cold waters associated with coastal upwelling is evident. After the upwelling period has passed, in Fig 3.2b, the alongshore surface front was located near the shelf edge. Resulting from the wind inversion to southerly on 12 July, a warm inner-shelf poleward flow was set up from 13 to 15 July between the cold recently upwelled waters and the shore, particularly at 41°N. On the

inner shelf, currents were generally poleward while near the slope they were equatorward. The second upwelling period (16-21 July) is represented in Fig 3.2c, where the strong temperature front between offshore waters and recently upwelled onshore waters is seen. Measured currents were mostly southward across the sections. The Lagrangian drifter drogued at 10 m depth was also moving southward along the 100 m bathymetry. The drifter accelerated during 18 and 19 July and slowed down on 20 July, in agreement with the pattern of the mADCP currents (Fig 3.1e) and the lADCP at nearby stations. The period of 21 to 23 July (represented in Fig 3.2d) is characterized by an inversion of the previous upwelling favorable conditions, and the setting up of a generalized poleward flow along most of the shelf with currents of 0.2 m/s. In spite of the prevailing downwelling conditions a remnant of the previous upwelling pulse is still visible as a band of cold water at the coast.

3.3.2 Water Masses

Fig 3.3 shows the TS-diagram of all CTD casts and SeaSoar profiles. Surface waters, with densities between 25.5 and 27 kg/m^3, increased in temperature and salinity from the shelf to offshore. Most profiles converge to the same water mass below 27 kg/m^3, reaching the depth of the ENACWst (Eastern North Atlantic Central Waters - Subtropical). At this level, salinity maximums are observed, reaching 35.82$\pm$0.2 on the shelf and 35.9$\pm$0.5 offshore. The ENACWst density remains fairly constant for salinities higher than 35.7. Between this point and 35.6, all profiles contain a salinity minimum as the signature of the subpolar origin waters (ENACWsp). In CTD profiles on the slope, a rise of salinity and temperature with depth in the lower part of the ENACWsp below 500 m depth, reveals the influence of the underlying Mediterranean waters.

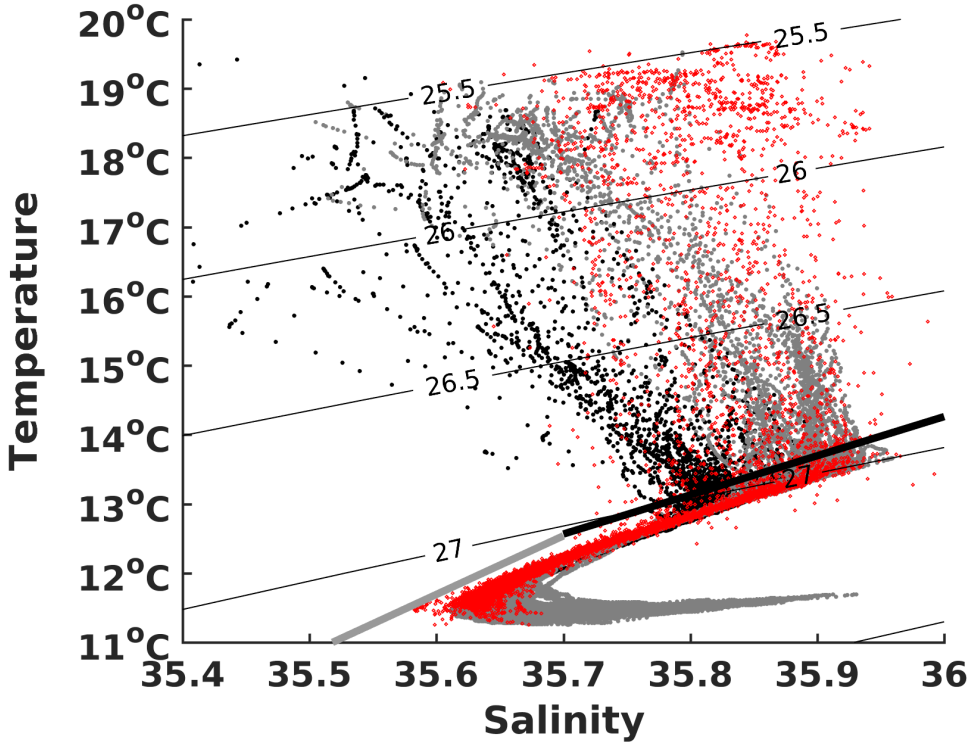

Figure 3.3: **TS diagram of CAIBEX cruise hydrography observations** Points represent SeaSoar (red) and CTD measurements (black - on the shelf, gray - profiles deeper than 200-m depth). Isopycnals are represented in thin lines (kg/m^3) and solid lines correspond to a definition of ENACWst (black) and ENACWsp (gray) based on (*Fiúza et al.*, 1998).

3.3.3 The IPC

The poleward flow off the Western Iberian Margin is associated with a subsurface salinity and temperature maximum and a downward slope towards the coast of isotherms and isohalines. The characteristics of the top 400 m of the IPC (Fig 3.4) were evaluated at the beginning and end of the cruise, on 7 and 23 July respectively, with the two long hydrographic transects off Cape Silleiro (transects 1 and 9 in Fig 3.1).

In transect 1, 7 July, below ∼70 m depth both the thermal and haline fields tilt downward towards the coast, in association with subsurface poleward flow across this section between 11°W and the slope. Above 70 m depth the opposite behavior is observed for the isopycnal field, with a tendency to tilt upward in this layer. At ∼10.2°W a mesoscale anticyclonic feature is visible.

Near the end of the cruise, 23 July, a shorter transect made at the same latitude,

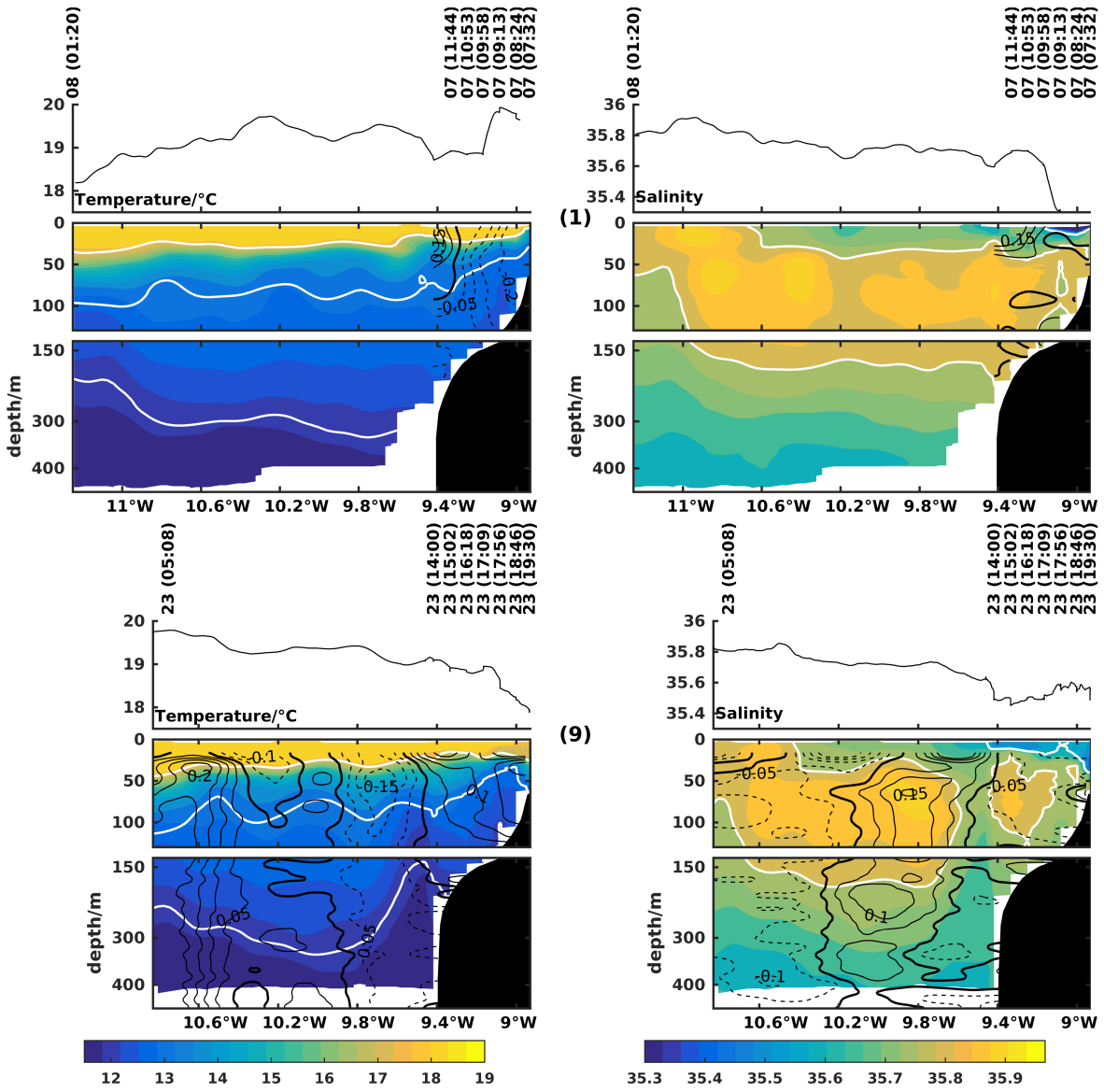

Figure 3.4: **Zonal transects numbered 1 and 9 of temperature (left column) and salinity (right column) off Cape Silleiro (42.10°N)** Day and time of each CTD cast and the underway surface temperature and salinity from the thermosalinograph are shown at the top. Dark contour lines represent along-shore (left column) and cross-shore (right column) currents in m/s measured with lADCP or vmADCP, when available. White contour lines are the 26 kg/m^3 and 27 kg/m^3 isopycnals on the left plots and the 35.6 and 35.8 isohalines on the right.

showed similar patterns to the initial transect from offshore 10.6°W to 9.8°W near the slope. The observed meridional flow was mainly poleward from the western extreme at ~10.8°W to 9.8°W, associated with the downward slope of the isopycnals. This poleward

flow was centered at ∼10.7°W with a maximum velocity of 0.2 m/s. From 9.8°W to 9.4°W the slope of thermal and haline fields changed and upwelling was observed below 50 m depth. Accordingly equatorward flow was observed near the upper slope, with maximum velocity around 0.15 m/s. The dynamics associated with this flow are discussed below.

3.3.4 Hydrography and Currents of the Distinct Periods

Four distinct periods were identified, as upwelling-favorable periods were interleaved with relaxation and downwelling. The first upwelling period of the cruise, 5 to 11 July was sampled only once on the shelf in transect 1. A relaxation period between 11 and 16 July was sampled by transects 2 and 3. The second upwelling period, 16 to 20 July, was sampled in 5 different latitudes by across-shelf transects 4 to 8. From 21 to 24 July, a downwelling period, the shelf was sampled once, on transect 9.

5-11 July : First Upwelling Period

The first upwelling favorable period followed a two week period of poleward flow and weak winds (Fig 3.1). Cold waters surfaced for the first time in AVHRR satellite images nearshore on 7 July, and gradually extended to the shelf edge until 10 July (not shown). Northerly winds were strongest in this period of offshore advection of the front, and relaxed rapidly on 11 July.

Fig 3.5 shows the top 200 m of transect 1 inshore of 9.80°W sampled on 7 July. The 27 kg/m^3 isopycnal rose from about 80 m depth offshore to less than 50 m nearshore. The thermocline was also shallower than 10 m nearshore, although not outcropping the surface. A fresher (<35.5) and warmer water (∼19.8°C) plume was observed at the surface of the inner shelf. The surface plume extended to 9.1°W as a warm water patch in the SST AVHRR image (Fig 3.2a) flowing out from Ria de Vigo to the shelf.

During the upwelling event, the currents on the shelf flowed equatorward, most strongly on the inner shelf (>0.2 m/s; Fig 3.5). Nevertheless on the outer shelf, the top 100 m flowed poleward with a maximum of 0.15 m/s. The zonal component was near-zero everywhere.

11-16 July: First Relaxation Period

Resulting from the wind relaxation of 11 to 16 July, set up of poleward flow was registered by the mADCP from 11 July onward (Fig 3.1e) with typical values of 0.1 m/s. On 14 July this flow was evident in transect 2 (Fig 3.6a) at latitude 41.5°N, coexisting with an upwelling front at longitude 9.1°W, an equatorward flow over the upper slope and the

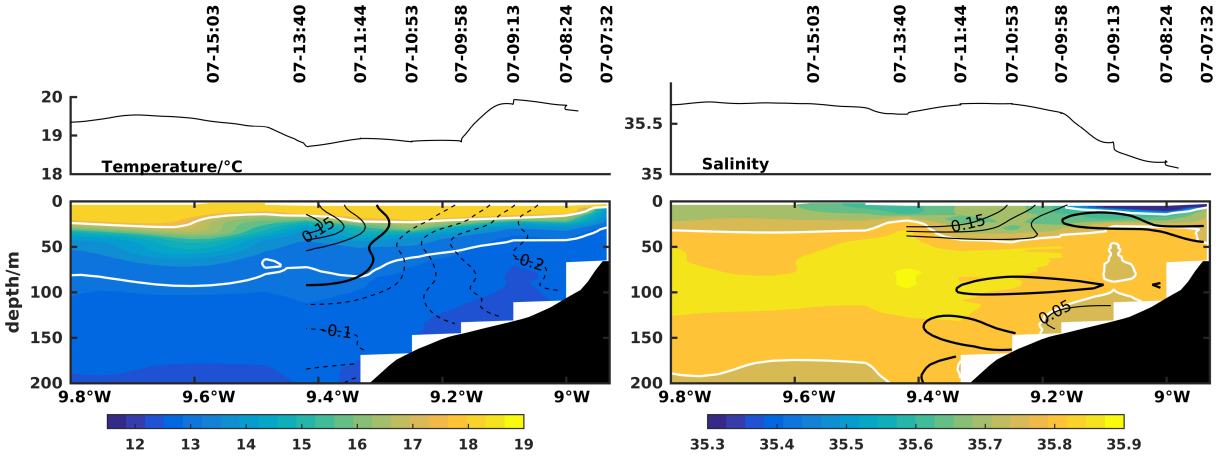

Figure 3.5: **Zonal transect 1 of temperature (left column) and salinity (right column) off Cape Silleiro (42.1°N)** Day and time of each CTD cast and the underway surface temperature and salinity from the thermosalinograph are on the top. Contour lines represent along-shore (left column) and cross-shore (right column) currents in m/s measured with lADCP or vmADCP, when available. White contour lines are the 26 kg/m^3 and 27 kg/m^3 isopycnals on the left plots and the 35.6 and 35.8 isohalines on the right.

IPC offshore of 9.7°W. Associated with the expected shoreward retreat of the upwelling surface front and with the onset of weak southerly winds, a shoreward surface flow is visible centered at 9.2°W, coincident with the plume of fresh waters. One day later, at 42.1°N latitude in transect 3 (Fig 3.6b), weak poleward flow of less than 0.1 m/s was still observed over the shelf while offshore of the shelf break, equatorward flow was prevalent.

16-20 July : Second Upwelling Period

During this upwelling period, a drifter drogued at 10 m depth was released on 17 July in mid-shelf at 42°N. Following the path of the drifter buoy, a sequence of 5 across-shelf transects (numbers 4 to 8) was conducted (Fig 3.7). Since the drifter buoy had a quasi-Lagrangian nature, the transects sampled approximately the same water parcel at 10 m at the longitude where they crossed the buoy path. The drifter followed the 100 m depth contour in the equatorward direction but was also affected by tidal and inertial oscillations. On the last day, 20 July, the drifter slowed down as the northerly winds relaxed.

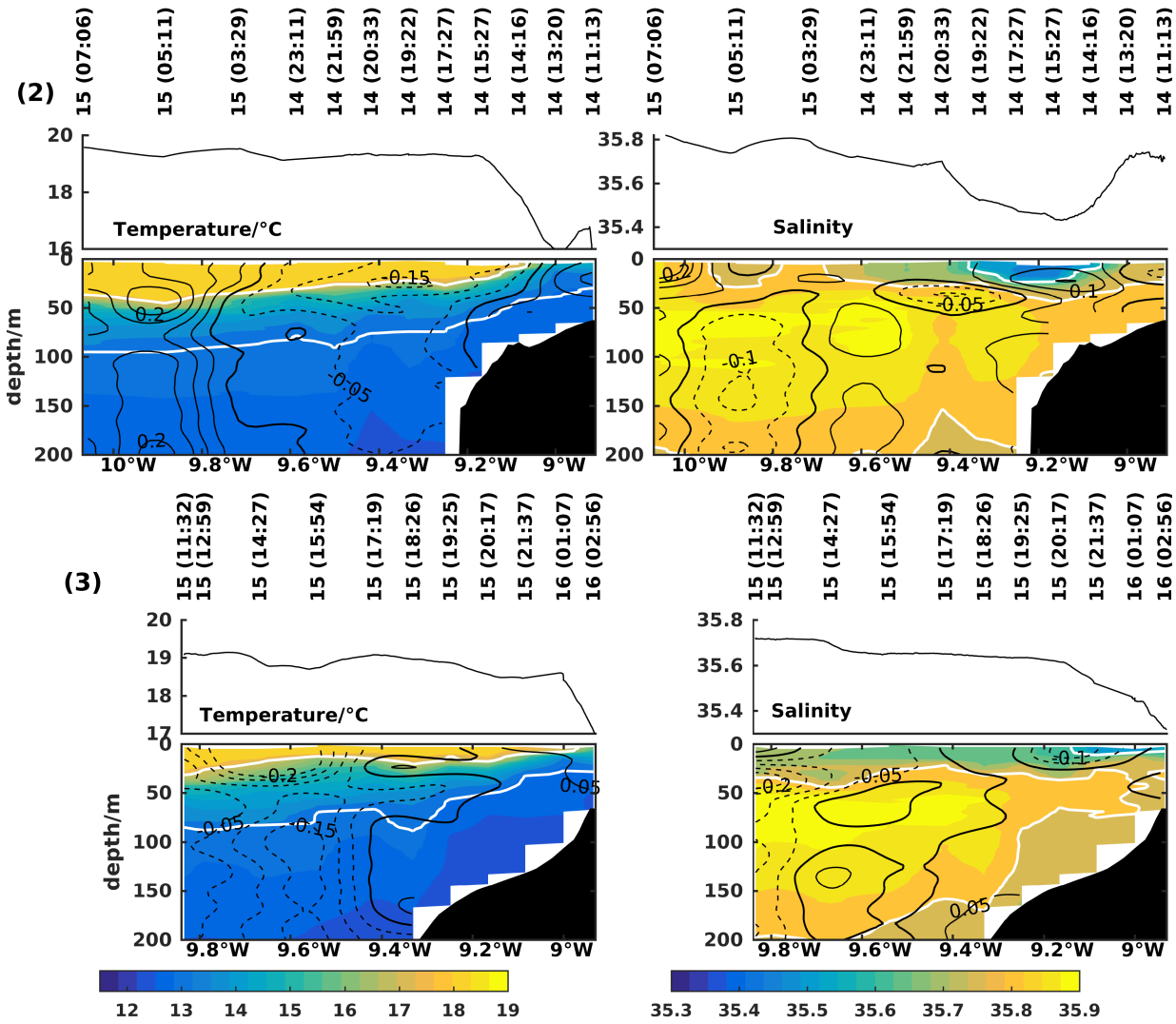

Figure 3.6: **Zonal transects 2 and 3 of temperature (left column) and salinity (right column) off Cape Silleiro (42.1°N)** Day and time of each CTD cast and the underway surface temperature and salinity from the thermosalinograph are shown at the top. Contour lines represent along-shore (left column) and cross-shore (right column) currents in m/s measured with lADCP or vmADCP, when available. White contour lines are the 26 kg/m^3, 27 kg/m^3 and 27.1 kg/m^3 isopycnals on the left plots and the 35.6 and 35.8 isohalines on the right.

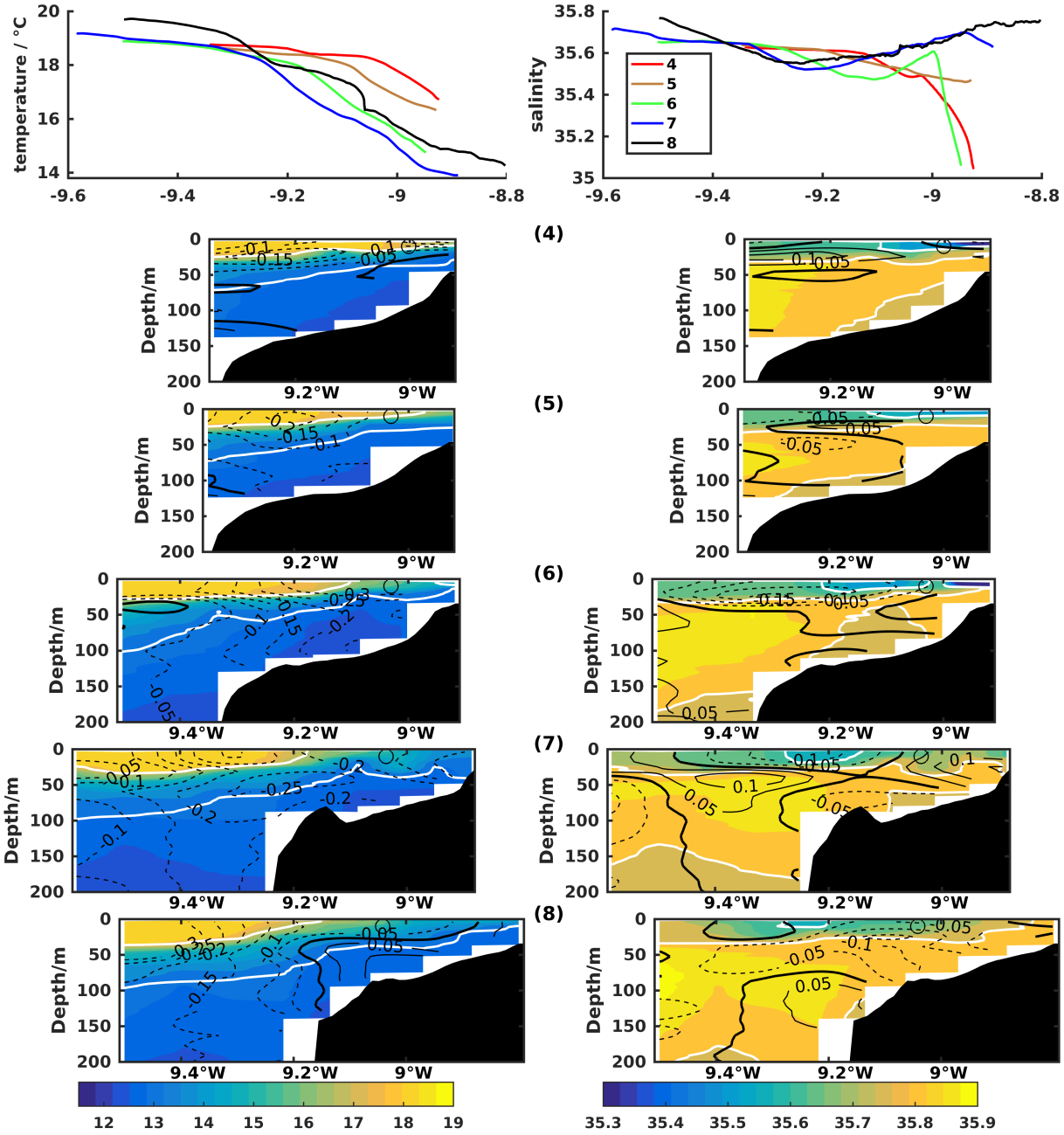

Figure 3.7: **Sequence of zonal transects 4 to 8 of (left column) temperature and (right column) salinity** The underway surface temperature and salinity from the thermosalinograph are shown at the top. Contour lines represent (left column) along-shore and (right column) cross-shore currents in m/s measured with lADCP or vmADCP, when available. White contour lines are the 26 kg/m^3 and 27 kg/m^3 isopycnals on the left plots and the 35.6 and 35.8 isohalines on the right. At each transect, a circle located at 10 m depth represents the position of the drifter buoy

The northernmost transect at latitude 42°N (4, of Fig 3.7) was sampled around 15h after the beginning of the upwelling pulse. At this time an equatorward flow was present at the surface, while poleward flow was still observed below ∼40 m depth. As a result of the preceding relaxation period, a stratified surface layer was observed across the shelf, with evidence of an incipient upwelling near the coast. SST measured by the thermosalinograph decreased 1°C near the coast. Beneath the surface, the temperature and salinity fields were tilted upward, and central waters were evident on the shelf bottom (<13°C temperature, <35.6 salinity). The surface salinity field was strongly influenced by a river plume. While offshore flow associated with the Ekman layer appeared at the surface, a compensating onshore flow was observed to transport salty waters onto the shelf below.

Still on 17 July, transect 5 at latitude 41.9°N shows the development of the surface equatorward flow with maximum velocities of 0.2 m/s. The development of upwelling is noticeable in the thermal field, with the cooling of the inner shelf surface waters and the establishment of a surface front. The cross-shore field exhibited a surface offshore flow.

The typical picture of fully developed upwelling was first seen in transect 6 on 18 July at 41.8°N latitude. At the surface, equatorward flow was observed, reaching maximum values of 0.3 m/s above a weakly sheared equatorward flow with values over 0.2 m/s. By this day the 27 kg/m^3 isopycnal had broached the surface, and the 26 kg/m^3 isopycnal outcropped mid-shelf as part of a well developed front being advected offshore at 0.2 m/s by a 40 m thick surface flow. At depth, a weak onshore return current was observed, as expected in a well developed upwelling phase. The surface plume of low salinity, previously adjacent to the coast, now extended to 9.2°W and was broken into two at around 9.05°W though stronger on the inner shelf. At deeper levels, the onshore flow advected salty waters (35.8-35.9) onto the continental shelf.

By 19 July, at 41.6°N latitude (transect 7), continued upwelling had advected the surface front offshore to the shelf break. The band of equatorward flow also extended offshore to the shelf break, while coastal alongshore currents decreased from -0.3 m/s in transect 6 to -0.1 m/s here. The offshore flow in the Ekman layer decreased while a complex cross-shore distribution developed below. The fresh water surface tongue extended further offshore with the salinity minimum observed at about 9.2°W just offshore of the shelf break.

At the end of the upwelling pulse, transect 8 was sampled at 41.36°N latitude, late 20 July. The surface seaward advection of the upwelling front seen in the previous two transects ceased simultaneous with the start of the northerly wind relaxation. Poleward flow was rapidly established on the inner shelf and below 30 m on the middle and outer shelf. Offshore of the shelf break the equatorward flow persisted in the surface layer. Resulting from the wind relaxation, the saltier waters at deeper levels over the shelf were

advected weakly seaward.

21-24 July : Second Relaxation Period

During this period, intense southerly forcing produced in transect 9 at 42.1°N (Fig 3.8) set up of poleward flow across most of the shelf, as usual coexisting with equatorward flow offshore of the shelf break. In the cross-shore flow, Ekman coastal convergence induced local downwelling of a low salinity plume down to ∼50 m depth, while weak offshore return flow was observed below this layer. A closed salinity maximum of 35.8 separate from the offshore IPC was observed at the outer shelf.

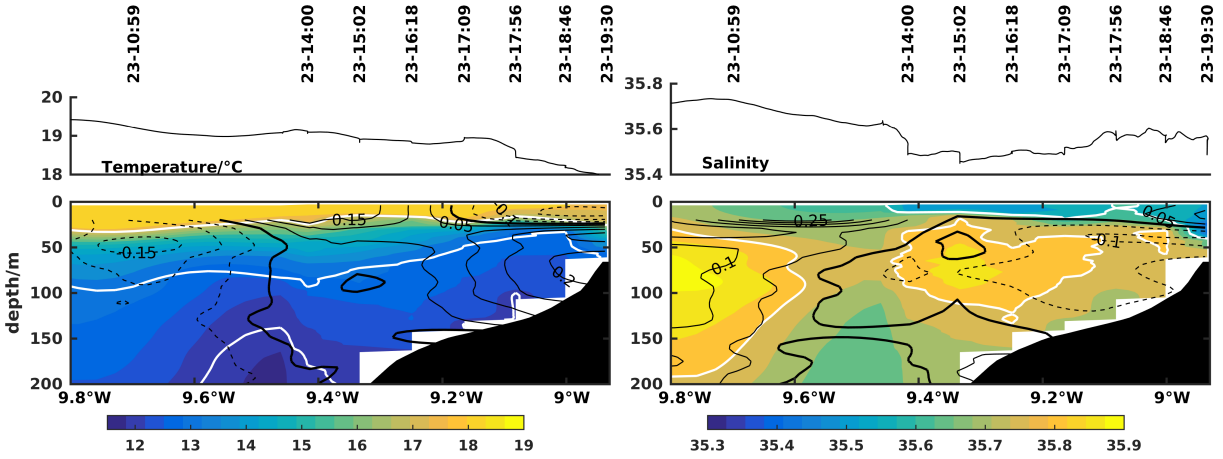

Figure 3.8: **Zonal transect 9 of (left column) temperature and (right column) salinity off Cape Silleiro (42.1°N)** Day and time of each CTD cast and the underway surface temperature and salinity from the thermosalinograph are shown at the top. Contour lines represent (left column) along-shore and (right column) cross-shorecurrents measured with lADCP or vmADCP in m/s, when available. White contour lines are the 26 kg/m^3, 27 kg/m^3 and 27.1 kg/m^3 isopycnals on the left plots and the 35.6 and 35.8 isohalines on the right.

3.4 Discussion

In the present study a situation of repeated upwelling spin up and relaxation cycles was observed, consisting in a sequence of development, offshore advance and retreat of upwelling fronts during nearly three weeks of July 2009. This situation corresponds to the first significant upwelling after the establishment of the surface layer stratification associated with the spring transition of that year. During the preceding two weeks, weak

southerly winds prevailed. The oceanographic conditions on the shelf were characterized by poleward flow, sampled with an ADCP moored at -8.93°W, 42.08°N, at the 72 m isobath, with mean values of 0.1 m/s.

The first transect of the cruise took place on 7 July, two days into the first upwelling favorable (northerly) wind period. Within this short period, a nearly barotropic equatorward jet associated with upwelling was set up, with maximum values of 0.2 m/s at the mADCP position, although the signature of upwelling could not be seen at the surface, as no clear outcropping of isopycnals was observed.

From 11 to 16 July was the first period of relaxation with weak and mostly southerly winds. In spite of the lack of upwelling-favorable winds, the hydrographic fields still resembled those of the previous period with evidence of upwelled waters on the shelf. However, the reversal of the flow was observed on the shelf with prevalence of a weak poleward flow (0.05-0.1 m/s).

Another upwelling favorable period occurred between 16 and 20 July. The observations show the quasi-Lagrangian sequence of the upwelling cycle south of Cape Silleiro, following a drifting buoy through the event. The shift from weak shelf currents to a fully developed equatorward flow was observed early in this upwelling cycle. On 20 July, wind began to relax and, in the southern transect, a poleward flow was observed nearshore extending to the mid-shelf bottom while equatorward flow was located offshore of the shelf.

From 21 to 23 July the second relaxation period occurred with strong downwelling favorable (southerly) winds. On 23 July, poleward flow was predominant on the shelf and coastal convergence was noticeable with a low salinity plume constrained against the coast.

In July 2009, on the Western Iberian Margin north of 41°N, two upwelling events were able to force equatorward shelf flow when they were strongest. The interruption of the upwelling regime, either by downwelling-favorable winds or relaxation, allowed the almost immediate return to a shelf poleward flow. These circulation cycles characterize the upwelling season of the NWIM, as the upwelling-favorable winds occur as intermittent pulses of several days and do not persist long enough to impose a completely equatorward regime.

On the three occasions the research vessel sampled offshore of the slope (transects 1, 2 and 9), poleward flow was observed, either directly through vmADCP measurements or estimated through the density fields. These flows at the offshore region are associated with the Iberian Poleward Current, observed predominantly during Autumn/Winter (*Haynes and Barton*, 1990; *Álvarez-Salgado et al.*, 2003; *Peliz et al.*, 2005; *Torres and Barton*, 2006), but also during the Spring-Summer transition (*Torres and Barton*, 2007). The poleward flow during summer was found also in numerical modeling studies of the WIM (*Nolasco*

et al., 2013a). The numerical study of *Teles-Machado et al.* (2016), using realistic forcing, reports an IPC (for spring) with similar structure to our observations, i.e. spread further from the slope.

Around the upper slope region, equatorward flow, accompanied by a doming of cold and fresh water between 9.4°W and 9.6°W is observed from the second transect onward. This flow could originate at Cape Finisterre and then be advected in the equatorward direction along the upper slope (*Torres and Barton*, 2007). Similar behavior was described by *Sordo et al.* (2001) based on satellite imagery to interpret the tongue of cold water extending from Cape Finisterre to Porto as a remnant of the equatorward jet of previous upwelling periods. Note that other authors report similar behavior for other locations of the WIM, namely *Moita et al.* (2003) for Cape Roca, and *Relvas and Barton* (2002) for Cape São Vicente.

The equatorward flow over the upper slope is characterized by a weak vertical shear intensified at the surface Ekman layer. It is likely that this equatorward flow influences the location of the IPC, keeping it offshore in the early upwelling season as suggested by the numerical study of *Nolasco et al.* (2013a), while later in the upwelling season the IPC usually develops under the upwelling jet in the upper slope (*Teles-Machado et al.*, 2016).

The upper slope equatorward flow separates two subsurface high salinity cores, one offshore associated with the IPC and another over the mid and outer shelf. This is particularly visible at the end of the cruise at longitude ∼9.5°W (transect 9). Furthermore, the dome of temperature and salinity fields associated with the upper slope equatorward flow is located offshore of the upwelling front. On the other hand, its SST signature is not clearly discernible by satellite imagery, as it is in *Sordo et al.* (2001) examples.

On the shelf, the circulation is mainly wind driven though pressure gradients and buoyancy input from river outflows play a role. During the two periods of northerly winds, an upwelling front developed along with its corresponding equatorward jet and across-shelf circulation. The lagrangian drifter released in the frontal region early in the upwelling period of 16 to 20 July proceeded to move equatorward following the 100 m isobath, advected under the influence of the upwelling jet.

The surveyed region, between Cape Silleiro and Porto, was a center of upwelling in July 2009, as is often the case (*Relvas et al.*, 2007) evidenced by the July mean SST (Fig 1.3). The existence of this upwelling center could be associated with two factors: i) coastal orientation nearly parallel to the prevailing upwelling-favorable winds (NNW) and ii) the variable alongshore shelf bathymetry. In the region of the upwelling center, the shelf widens in the equatorward direction. *Pringle* (2002), using a barotropic, linear and steady potential vorticity equation, showed that the onshore transport of deep upwelled waters,

primarily through the bottom layer, enhances where the shelf widens in the direction of the upwelling jet, hence upwelling is intensified in these regions. The generation of upwelling centers was discussed in the baroclinic case by *Gan et al.* (2009) for the northeastern South China Sea, reinforcing the association of upwelling centers to regions of widening shelfs.

This upwelling center may induce the establishment of a poleward inner shelf flow once the northerly winds relax, as is the case of the Northern Californian shelf from Point Reyes to Point Arena (*Pringle and Dever*, 2009). These authors show that in the presence of an upwelling center, a poleward gradient in density sets an equatorward pressure gradient that induces poleward flows, maintained when upwelling favorable winds relax. This mechanism may explain the trend to poleward flow during the relaxation period of 12 to 16 July. This mechanism could also explain the coastal poleward flow described by *Sordo et al.* (2001) associated with wind relaxation at the end of the upwelling season.

On the other hand, during the second relaxation period, the observed poleward flow in the shelf seems to be associated with downwelling-favorable winds, in accordance with the classic downwelling theory. Other example of wind driven downwelling flow in the region is provided by *Torres and Barton* (2007). In this relaxation period, the coastal poleward flow advected a low salinity plume and downwelling promoted its convergence and coastal trapping near Cape Silleiro. This structure is unusual in the summer although it was already documented in similar systems such as the Columbia River plume (*Fiedler and Laurs*, 1990) and supports regional modeling experiments such as *Otero et al.* (2013). In the early stages of upwelling, exporting of plumes from Rias Baixas, can briefly hinder the surfacing of upwelled waters, such as in Fig 3.5. During the upwelling periods, the buoyant plume is advected southward and offshore across the shelf, as was the case in *Rossi et al.* (2013) further south on the WIM and was observed in the sequence of transects in Fig 3.7. The shoaling of the exported offshore plume results in the confinement of plankton in these nutrient rich waters (*Ribeiro et al.*, 2005).

The response of the circulation on the shelf to transient events of upwelling, relaxation and downwelling is linked to the ecosystem dynamics. In terms of advection patterns, upwelling pulses and downwelling events have been shown important for the bi-directional transport of species of phytoplankton between the Rias Baixas and central WIM (*Moita et al.*, 2016), responsible for the alongshore spreading of HABs.

As *Rossi et al.* (2013) reported during an upwelling event, the upwelling pulses regularly bring cold, fresh and nutrient-enriched waters to the surface, driving the biological cycles. In general the upwelling front separates the oligotrophic offshore ecosystem characterized by low biomass of small phytoplankton species (mainly cyanobacteria) located at the bottom of the surface mixed layer in a subsurface chlorophyl maximum (20-50m depth), from the

inner coastal waters, where the species distribution are mostly large microplakton (diatoms and dinoflagellates) especially during the upwelling relaxation (*Castro et al.*, 1997; *Tilstone et al.*, 2003; *Lorenzo and Taboada*, 2005).

The physical processes dicussed above are also linked to the nutrient and oxygen cycles. In the presence of upwelling, the surface nutrients are depleted by the phytoplankton, then replenishment at depth by microbial remineralization of the sinking organic matter (*Álvarez-Salgado et al.*, 1997), which consumes the oxygen at deeper levels. Minimum oxygen concentrations were observed in the bottom layers of the shelf in this cruise (not shown) in line with the *Rossi et al.* (2013) results. In the offshore olygotrophic waters, sub-surface maximums of oxygen are associated with photosynthesis of phytoplankton.

3.5 Conclusion

An 18 days long oceanografic survey took place in the NW Iberian Margin in July 2009, sampling the shelf and offshore, allowing a synoptic view of several events, including a novel quasi-Lagrangian sampling of an upwelling event. The cruise observations were complemented by an upward looking ADCP moored near Cape Silleiro at 72 m depth.

The results of this cruise show the rapid response of the shelf circulation to changes in alongshore wind both in developing an equatorward flow regime (following the classical theory of upwelling), and the set-up of poleward flow associated with wind relaxation. These two circulation regimes are schematically represented in Fig 3.9. Excepting the shelf, the circulation was similar to both regimes, with the IPC located offshore of an upper-slope equatorward current, both associated with the subsurface isothermal slope.

The scheme of Fig 3.9a corresponds to a regime typical of prevailing northerly winds, including a center of intense upwelling (with an associated temperature front) and an upwelling jet observed throughout the shelf, circulating alongside the upper-slope equatorward current. Another regime is associated with the relaxation of upwelling favorable winds (Fig 3.9b), which is characterized by a poleward flow along the shelf. Warm waters are carried nearshore intruding into the previously generated cold upwelling center. The system of currents reported here, at the timescale of the shelf circulation response to wind forcing, confirms previous findings in the literature. Their further investigation in this region is relevant from the point of view of marine ecosystem management, as these transport processes strongly influence the biogeochemical properties and the alongshore distribution of HABs, larvae and pollutants along the coast of the NW Iberian Margin.

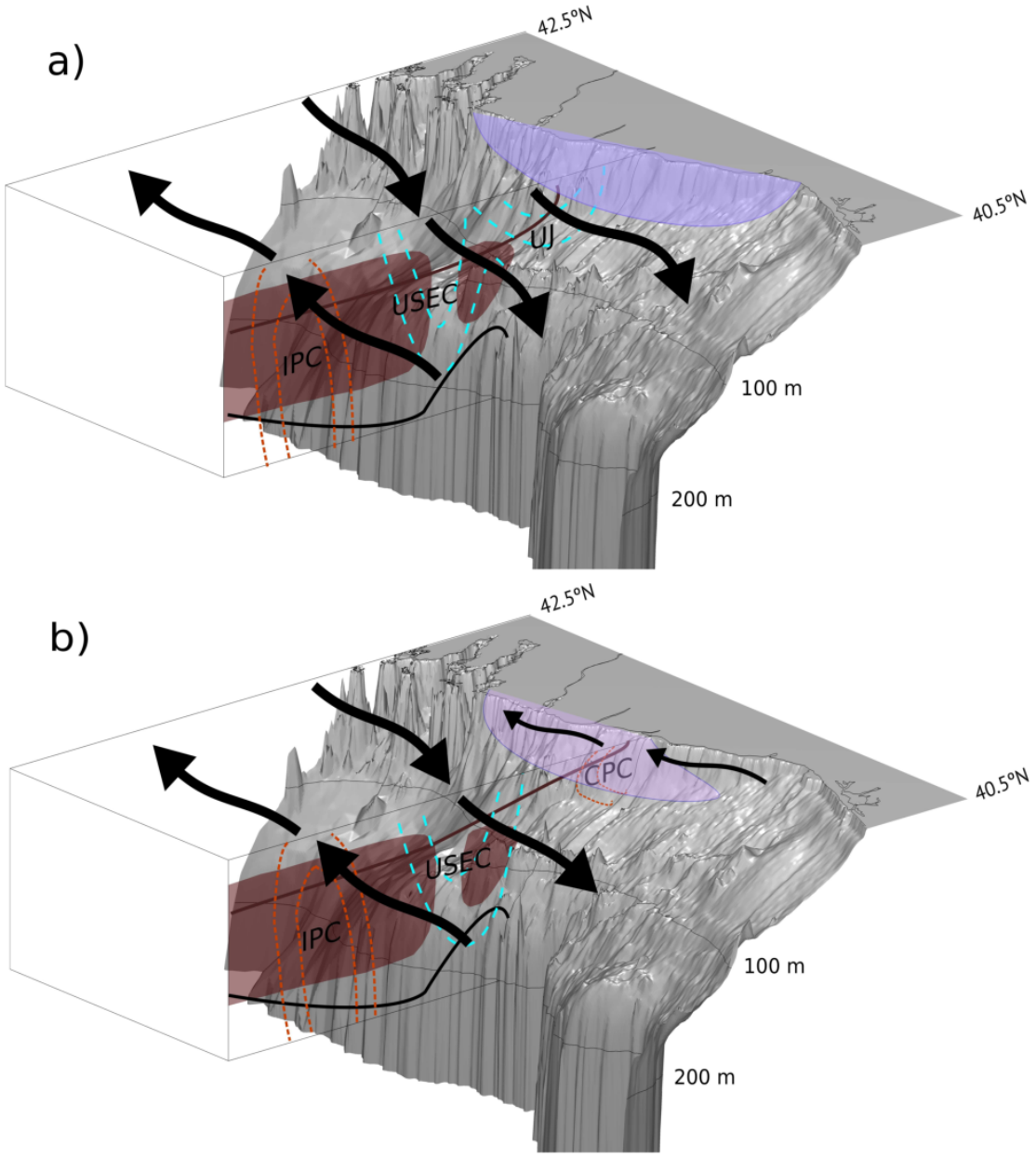

Figure 3.9: **Conceptual schemes of circulation** Under (a) upwelling regime and (b) relaxation regime. The prevalent currents are depicted on the transect by the dashed countours in red (poleward flowing) and blue (equatorward flowing) and identified with the acronyms: Iberian Poleward Current (IPC), Upper Slope Equatorward Current (USEC), Upwelling Jet (UJ) and Coastal Poleward Current (CPC). On the transect, dark lines represent the preceived field of isothermals and reddish areas mark location of central waters with subtropical origin. At the surface, the perceived paths of currents are marked as arrows, and the upwelling center as the blue (a) and purple (b) shading, representing a stronger and weaker temperature anomaly, respectively.

Chapter 4

NWIM Continental Shelf Seasonal Cycle

4.1 Introduction

The study of the shelf circulation throughout the annual cycle has seen some development in the past through observational efforts of regional projects. Covering stations on the shelf outside of Ría de Vigo, under IEO Radiales program, monthly surveys have been performed since 1987 (*Valdés et al.*, 2002; *Gago et al.*, 2011). Apart from this long time series, observations of physical parameters on the shelf have been punctuated with extensive survey programs like MORENA or Galicia II to XI cruises (references within *Castro*, 1996), and for monitoring of the coastal region either from the perspective of oil spill (Hydroprestige) or resulting from the growing awareness of HAB events repercussions on Rías Baixas economical activities (ASIMUTH, HAB-SPOT). Under the OMEX II-II project a mooring monitored the mid shelf circulation and hydrography in Porto region between January and May 1998. In the framework of project DYBAGA a transect of 5 stations on the shelf in front of Cape Silleiro was repeated 47 times from May 2001 to May 2002 (*Nieto-Cid et al.*, 2004; *Herrera et al.*, 2008), providing enough sampling frequency for an analysis on the processes responsible for the shelf dynamics.

The focus of the previous chapter (chapter 3) was the analysis of upwelling cycles and their corresponding relaxations, based on the data from an oceanographic cruise occurring in July 2009 and covering the NWIM. Profiting from the extensive data set gathered during the CAIBEX experiment, an annual cycle (from autumn 2008 through autumn 2009) of the shelf hydrology and circulation is analyzed in this chapter, in which the period from Chapter 3 is included. Special focus is made on the shelf off cape Silleiro, south of Rías

Baixas where the quasi-monthly cruises were performed.

In this chapter, a model configuration of the NWIM is presented in order to complement the observational data and investigate the temporal evolution of the 3D fields. The validation of the model results is based on the comparisons with the available data set. With the model thoroughly validated, the main processes on the shelf are assessed based on the combined results of the modeling and the observational data.

This chapter presents the following structure: Section 4.2 describe the data and methods applied. The results are presented in Section 4.3, in which the model is validated through its comparison with the observations of time series of temperature, salinity and currents for various points across the shelf. Different periods were identified according to the hydrology and circulation patterns for further exploration in Section 4.3.3 by the inspection of specific characteristic events. The main findings are discussed in Section 4.4 and summarized in Section 4.5.

4.2 Data and Methods

4.2.1 ROMS Model

A model configuration (NWIc, Section 1.4.4) was developed specifically to simulate the circulation and hydrography on the Northwestern Iberian Margin, applying a two-way nesting approach to solve the open ocean, shelf and Rias Baixas interactions. The analysis done in this chapter is based on the results of the NWIc model for the period between November 2008 and December 2009.

4.2.2 Observational Data

For this chapter, observational data obtained from the region near cape Silleiro was used (Section 1.3, Fig. 1.2). Alongshore currents from the mADCP were retrieved at 6 m depth (near-surface) and at 2 m above bottom (near-bottom), as well as the near-bottom temperature. The temperature and salinity of CTD profiles was retrieved from the 11 transects of the monthly surveys (7 stations each, oriented across shore) and 19 inner-shelf stations aboard RV *Mytilus*, as well as 3 transects as part of the wider oceanographic cruise aboard RV *Sarmiento de Gamboa* in July 2009 with a CTD *seabird 911+* (analyzed in Chapter 3). Details of the 14 CTD transects are documented in Appendix B. Five of these transects (14 November 2008, 13 January 2009, 22 June 2009, 17 September 2009 and 10 November 2009) are also shown and analyzed in this chapter.

As a proxy of the freshwater inflow in the region, the river Minho flow at the Frieiras Dam is presented in this chapter, due to its proximity to cape Silleiro and high correlation with the other main rivers located south of Rías Baixas (*Otero et al.*, 2010).

4.2.3 Statistical Analysis

A thorough evaluation of the model results is required, assessing its strengths and weaknesses while comparing with the available observations. Regarding time series of temperature, salinity and currents the model performance was obtained through a Taylor Diagram (*Taylor*, 2001). The Taylor diagram is composed by three statistic parameters, namely the correlation coefficient (r), centered root mean square difference (RMSD) and standard deviation (σ).

The correlation coefficients calculated in this chapter are significant to a p-value$<$0.05. Both the correlation coefficient and the centered root mean square difference are applied to normalized data:

$$r = \frac{\sum_{n=1}^{N}[C-\overline{C}]\times[Cr-\overline{Cr}]}{N\times\sigma_C\times\sigma_{Cr}}; RMSD = \sqrt{\frac{\sum_{n=1}^{N}((C-\overline{C})-(Cr-\overline{Cr}))^2}{N}} \tag{4.1}$$

In which C and Cr are respectively the normalized modeled parameter (M) and normalized observations of the same parameter (D), and σ is the standard deviation:

$$C = \frac{M-\overline{M}}{\sigma_M}; Cr = \frac{D-\overline{D}}{\sigma_D}; \sigma = \sqrt{\frac{\sum_{n=1}^{N}(C-\overline{C})^2}{N}} \tag{4.2}$$

A skillful model should be able to accurately simulate the amplitude and pattern of variability. The importance of each factor depends on the application and should be decided subjectively. Thus a single skill score cannot be defined universally. Based on the Taylor diagram, the skill depends solely on the RMSD, increasing with higher correlations or when the modeled variance approaches the observed variance. This way, the Taylor diagram only defines the model skill based on pattern differences and not based on mean differences, which is given by the bias (bias = M - D).

4.2.4 Empirical Orthogonal Functions (EOFs)

To investigate the temporal and spatial variability of the surface oceanographic properties, Empirical Orthogonal Function (EOF) analyses were applied to the modeled surface

fields of temperature, salinity and velocity.

The EOF method allows the representation of the data in terms of a reduced set of orthogonal functions or modes. The EOF eigenvectors and eigenvalues are obtained through Singular Value Decomposition (SVD) (*Preisendorfer*, 1988). The outputs consist on spatial eigenvectors (spatial EOF) with their associated eigenvalues (relative amount of variance) and Principal Component time series (PC - temporal weightings for each time step).

That is, a variable is considered to be a function f of space and time, computed for constant space and time intervals. The EOF method represents the data as a sum of products of both the spatial EOFs (EOF_i) and the PC time series (PC_i):

$$f(x,y,t) = \sum_{i=i}^{N} EOF_i(x,y)\ PC_i(t) \tag{4.3}$$

with which the original data set can be reconstructed using i = 1 to N modes. The advantage of EOF analysis is that it provides a compact description of the spatial variability and its temporal variation, in terms of empirical modes, each contributing with a certain percentage to the total variance. However, the empirical modes do not necessarily correspond to true dynamical modes or modes of physical behavior, thus their physical interpretation is not always possible. For example, a single physical process can be reproduced in more than one mode or, on the other hand, more than one physical process may be contributing to the variance contained in one mode.

The application of this method to vectorial properties such as the oceanic currents, needs to take in consideration the Cartesian components (*Kaihatu et al.*, 1998). The simplest approach indicated by those authors is the Real Vector EOF (rvEOF), whose only difference from the generic EOF is that each spatial EOF is composed by a meridional and zonal component. The resulting spatial EOFs consist on vector fields with their corresponding scalar PC time series.

The EOF analysis was applied to the surface velocity, temperature and salinity fields of the NWIc-1 domain detailed in Section 1.4.4. The model outputs were composed by 12h averages with the original spatial resolution. Before performing the EOF analysis, the temperature time series were smoothed by using a 100 day high pass filter, removing low frequency variations. This way, the target time scales of days to months are highlighted, as the seasonal and semi-seasonal cycles were removed from the data. The salinity and velocity data were not filtered, since their signals are not dominated by seasonal and semi-seasonal frequencies. For each variable, the analysis was done to the two modes explaining

the highest variability. The rule of thumb by *North et al.* (1982) was applied to all modes, verifying that, for each variable, the first and the second modes were statistically significant.

4.3 Results

4.3.1 Time Series of Available Data

At the mooring site, time series with hourly alongshore currents, temperature and salinity were made for the near-surface (6 m depth) and near-bottom (2 meters above bottom - mab) in order to compare with shallowest and deepest noise-free layers sampled by the mADCP (Fig. 4.1). CTD casts sampled in the site were used to validate the temperature and salinity on both layers, and the temperature was complemented by the continuous record near the bottom from the mADCP.

Another place where it was possible to obtain time-series of data was the Silleiro buoy (green star in Fig. 1.2), 55 km from the coast, from which the near-surface (3 m depth) hydrography and circulation were compared with the observations (fig 4.2).

The model performance was assessed for the mADCP location and the Silleiro buoy in terms of its ability to reproduce the temperature, salinity, currents and wind variability at these points. The assessment is summarized in the form of a Taylor diagram in Fig. 4.3. The wind at the Silleiro buoy (Fig. 1.4) was generally better reproduced than the oceanographic variables, although the surface temperature at the Silleiro buoy (Tsb in Fig. 4.3) had the best scores. In fact, the temperature variable was well reproduced in all locations, with $r>0.80$ and standard deviations close to 1. The salinity performance was not as good, with $0.6<r<0.85$ and, with standard deviations spread between 0.78 (surface mooring - Ssm in Fig. 4.3) and 1.25 (bottom mooring - Sbm in Fig. 4.3). The alongshore current was better represented at the mADCP location than at the Silleiro buoy, while the temperature was better represented at the latter.

At the mADCP location, the near-surface temperature (Fig. 4.1b, Tsm in Fig.4.3) of ROMS and CTD cast records were similar throughout the seasonal cycle, ranging from $\sim$12°C in January to $\sim$18°C in July. In Spring, the rising temperature was interrupted by infrequent decreases associated with upwelling favorable wind pulses, most notably late May and middle June. In July the temperature was mainly about 18°C with brief dips during upwelling periods, while after early August through September, the temperature bordered 14°C with brief increases on relaxation periods. With the ceasing of northerly wind pulses in October, and development of southerly winds, both modeled and observed temperatures returned to nearly 18°C. During an event of strong northerly winds in the

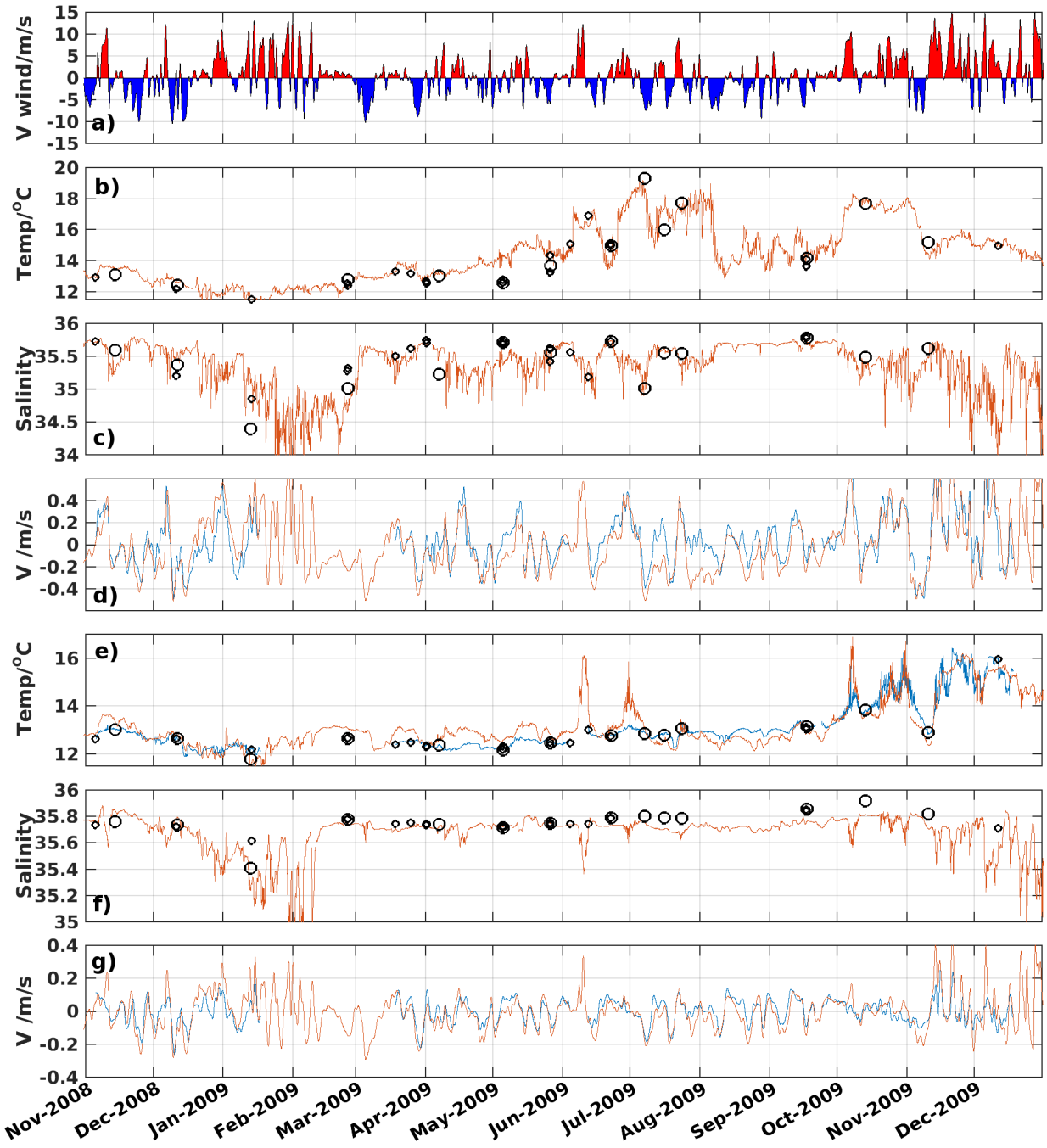

Figure 4.1: Time series of (a) the alongshore component of wind, (b,e) temperature, (c,f) salinity and (d,g) alongshore component of currents at the mADCP location, taken from (b,c,d) 6 m depth and (e,f,g) 2 mab. Red lines are the model results, blue lines represent measurements by the mADCP and black circles represent CTD measurements, where the large ones are from the quasi-monthly cruises and the smaller ones are from other spurious CTD casts.

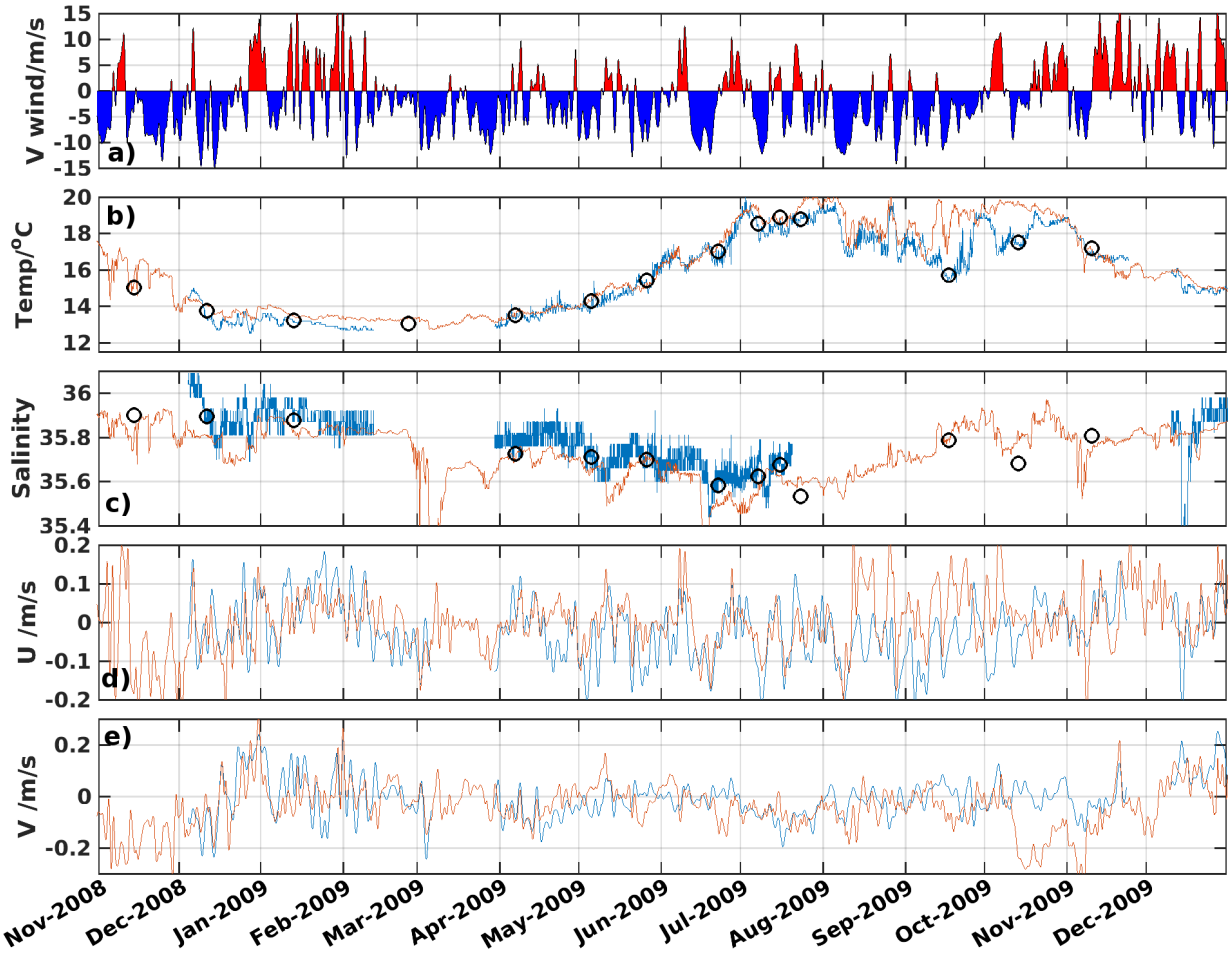

Figure 4.2: Time series of the alongshore component of (a) wind, (b) temperature, (c) salinity, (d) cross-shore component of currents and (e) alongshore component of currents at the Silleiro buoy, taken from (b,c,d,e) 3 m depth. Red lines are the model results, blue lines represent measurements by the buoy instruments and black circles represent CTD measurements.

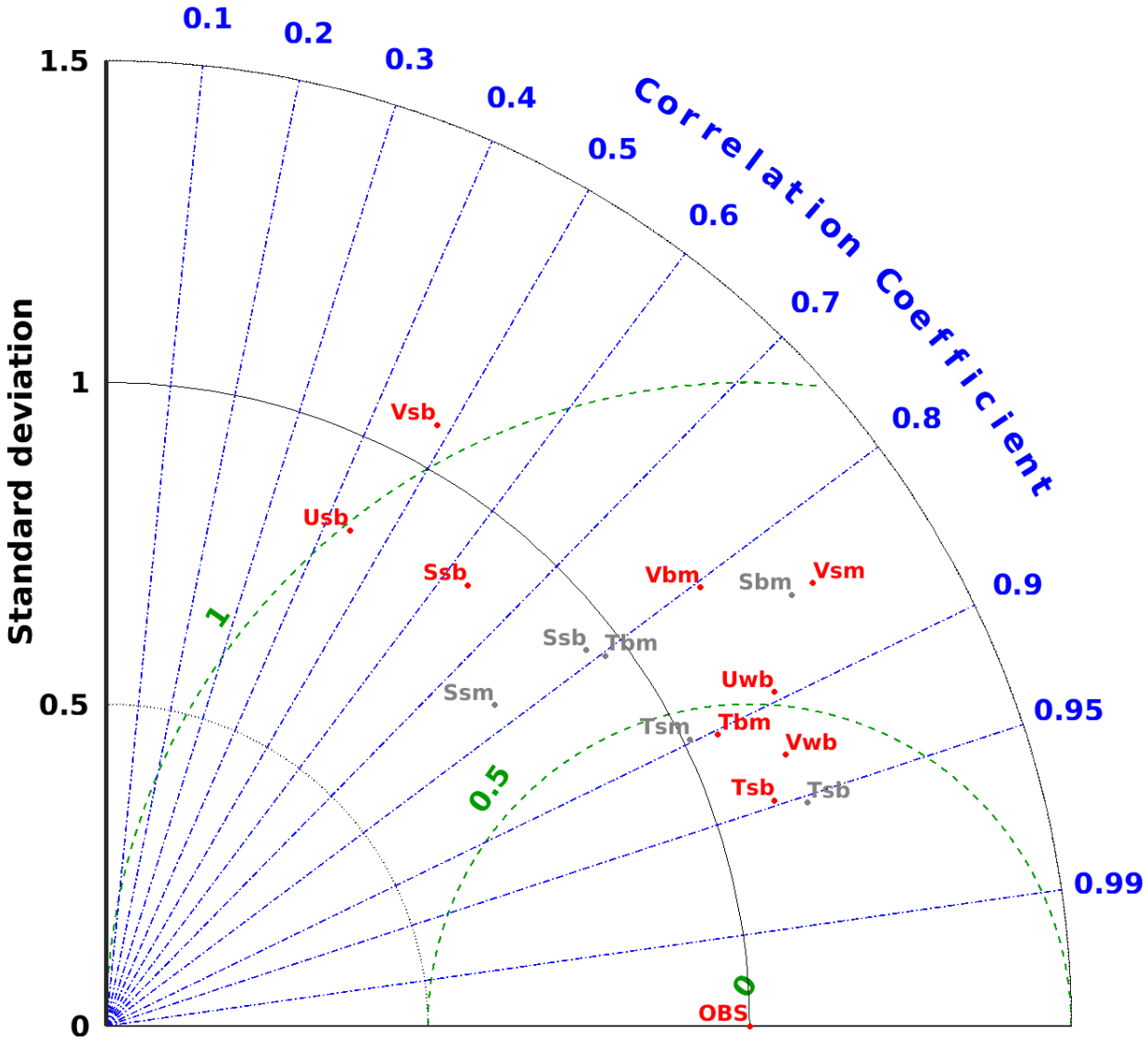

Figure 4.3: Taylor diagram of the all time series comparisons between observations and model from Figs 4.1 and 4.2. Gray points represent the comparison with the CTD stations and red points are the comparisons with continuous time series (mADCP and buoy). The text code of each validation is composed by "Capital letter" "first lower case" "second lower case". The capital letter is the variable: temperature (T), salinity (S), current/wind velocity cross-shore component (U) and along-shore (V); The first lower case is the position in the water column: surface (s), bottom (b) and wind at 10 m high (w); and the second lower case is the location of the station: mADCP location (m) and Silleiro buoy (b). The reference point (OBS) represents the observations and has standard deviation of 1 and correlation of 1.

first days of November, the temperature fell ∼3°C, remaining around 15°C at the surface until the end of the year. The temperature in November and December 2009 was about 2°C higher than the same months of the previous year, while the alongshore winds were predominantly southerly for these 2009 months and northerly in 2008, as discussed later.

The near-surface salinity (Fig. 4.1c - Ssm in Fig. 4.3) did not display a marked seasonal cycle like the temperature. It usually varied between 35 and 35.8, except in January/February 2009 and after mid November 2009, when the salinity maximum barely passed 35.6 and minimum values were as low as 34. Comparing with the CTD, the model results had differences of <0.1 in the periods of low variability (e.g. March 2009) and up to ∼0.5 in highly variable periods (e.g. January 2009).

The near-surface alongshore subinertial velocities at the mADCP location (Fig.4.1 - Vsm in Fig. 4.3) responded to the local meridional wind velocity, with maximum correlation between them at a lag of 14 hours (r = 0.72). Peaks of 5-10 days length were observed throughout the time series, with equatorward peaks of about 0.4 m/s and poleward peaks reaching about 0.5 m/s during the downwelling periods (winter 2008/2009 and autumn 2009). In general the observed (blue) and modeled (red) alongshore velocities corresponded well. Exceptions occurred in some periods of relaxation from northerly upwelling-favorable winds, for instance in the relaxation periods of mid and late July the observations showed a quick shift to poleward flow (the Coastal Poleward Current reported in Chapter 3) while the modeled currents remained equatorward.

The temperature near the bottom (Fig. 4.1e, Tbm in Fig. 4.3) had a less defined seasonal cycle, with low variability around 13°C during most of the studied period until end of September 2009. From October 2009 onward, associated with the increasing frequency of downwelling pulses, the bottom temperature simulated by the model and the mADCP record increased nearly 3°C. Also associated with downwelling pulses, two peaks of 2-3°C increase were simulated in June 2009. During the first peak, occurring around 10 June, no observations were performed, while in the second the mADCP temperature registered a slight increase of <0.5°C. The simulated temperature generally followed the same patterns as the observed temperatures with differences under 0.5°C, except between March and June when the modeled temperature was about 0.5°C higher than observed.

The near-bottom salinity (Fig. 4.1f, Sbm in Fig. 4.3) was about 35.7-35.8 during the study period, with dips associated with convergence of fresh water plumes, reaching as low as 35 early February 2009. The differences between the simulated near-bottom salinity and the CTD casts were typically under 0.1, with the simulation being noticeably lower than the observations between July and October 2009.

The modeled and observed near-bottom alongshore currents (Fig. 4.1g, Vbm in Fig. 4.3)

had similar signal to the surface currents, although less intense. The equatorward peaks did not surpass -0.3 m/s and the stronger poleward peaks were about 0.3-0.4 m/s.

At the Silleiro buoy the seasonal cycle of the temperature (Fig. 4.2b, Tsb in Fig. 4.3) was more pronounced than in the more coastal mADCP location, and was frequently influenced by the position of the upwelling front separating coastal from oceanic waters. The temperature values ranged from about 13°C in winter months (January, February and early March 2009) to a maximum of 20°C in the summer with 2°C drops during strong upwelling events. The difference of the simulated temperature from the observations was under 0.5°C until end of July 2009. In September and October, brief periods occurred when simulated temperatures were 1-2°C higher than the available observations.

The salinity at the Silleiro buoy (Fig. 4.2c, Ssb in Fig. 4.3) varied between 35.4 (March 2009) and 35.9 (November/December 2008). Up to March 2009, the simulated salinity decreased from around 35.9 in December 2008 to <35.8 in March 2009, similar to the observations, with differences under 0.05. Starting April 2009 the simulated and observed salinity decreased from 35.8 until reaching about 35.5 in June 2009. In July and August 2009 the salinity gradually increased, remaining around 35.8 through the rest of the year.

In general, the surface velocity (Fig. 4.2d and e, Usb and Vsb in Fig. 4.3) observed at the Silleiro buoy was similar to the model results and responded to the wind forcing. The cross-shore component (U) was primarily associated with the Ekman layer dynamic, with positive (negative) values associated with downwelling (upwelling) favorable wind. Also associated with the upwelling/downweling dynamics, the along-shore component (V) responded similarly to the mADCP location.

4.3.2 Seasonal Cycle of the Shelf Hydrography

Hovmuller diagrams of longitude against time in the Silleiro transect were built for the 6 m depth temperature and salinity stations, showing the time evolution of these variables across the shelf (fig 4.4). Modeled variables were represented for late 2008 and 2009, superimposed by colored circles of the discrete observations by the CTD casts. On the left side of the temperature plot, equatorward (poleward) wind speed is displayed in blue (red) colors, while on the right side of the salinity the river Minho flow at the Frieiras Dam is shown.

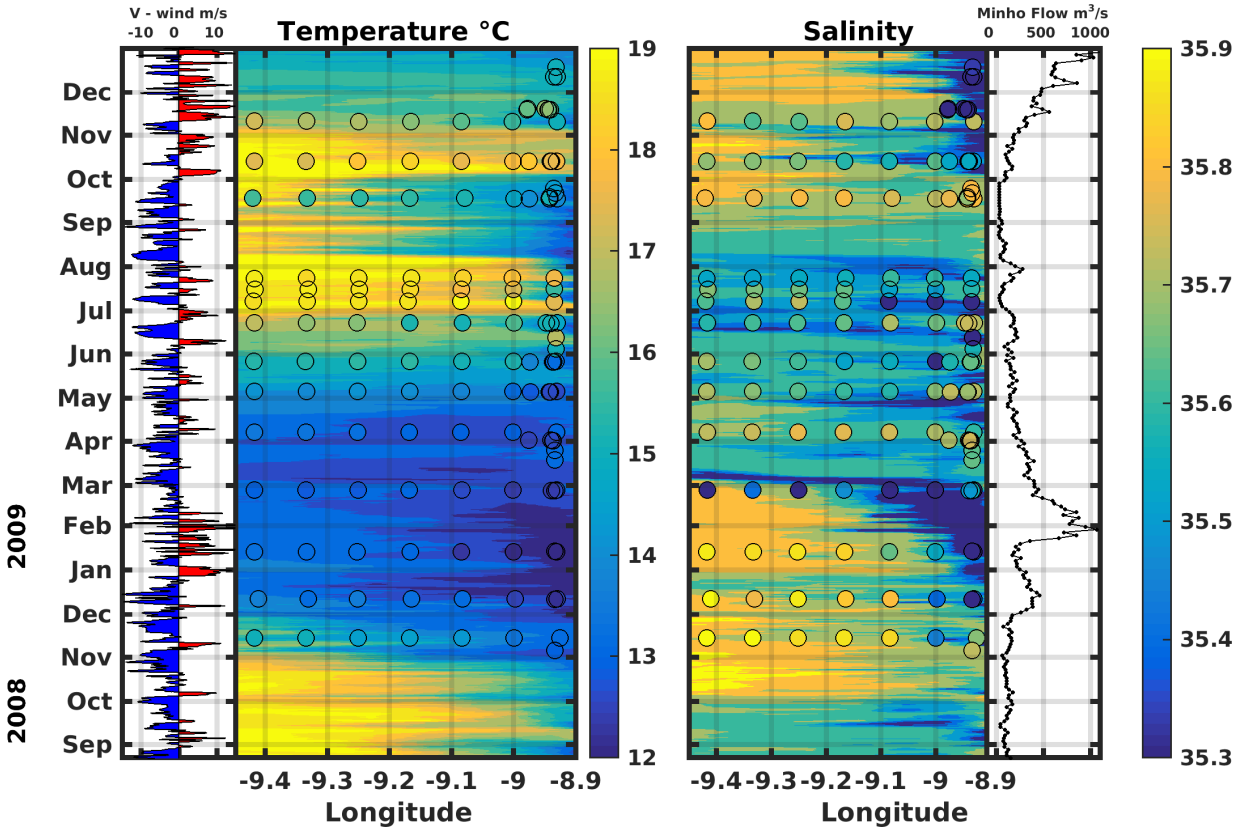

Figure 4.4: Hovmuller diagram of temperature and salinity at 6 m depth, with (left) alongshore winds at the shelf edge and (right) River Minho flow at the Frieiras Dam.

At the end of the upwelling season of 2008, in October, the shelf was flooded by saline and warm waters (salinity of ∼35.9 and temperature of ∼19°C). In early November 2008, resulting from a strong upwelling event related to northerly winds persisting since mid October, these waters were replaced by colder and fresher waters, homogeneous across most of the shelf.

In January, the continuous passage of atmospheric frontal systems resulted in strong surface winds and input of fresh water induced by continental runoff. Even though winds were variable, downwelling prevailed until mid February and the WIBP was generated as a narrow band of fresher waters near the coast (9°W-8.9°W). In mid February winds weakened and became northerlies, promoting the offshore spreading of the WIBP intensified by the remarkably high continental runoff (River Minho flow >600 m^3/s per day).

From March to June, the surface shelf temperature increased gradually and events of upwelling (∼ 15 days) were intercalated with shorter downwelling events (∼ 5 days). The WIBP was not as intense as previously but responded in the same way to the alternating upwelling/donwelling events. In spite of the presence of upwelling favorable winds, no clear

onshore-offshore SST contrast was visible. By the end of June, surface temperature over the shelf abruptly increased as offshore waters intruded during a period of downwelling. By this point, the water column became more stratified with the seasonal warming of the surface mixed layer (differences of ∼4°C between near-surface and near-bottom, Fig. 4.1).

Starting July, during an upwelling event (5 to 11 July, first upwelling period in Chapter 3), as a consequence of the contrast between the previously warmed shelf waters and the uplifting of cold subsurface waters, a thermal front was generated that remained during the summer months. In July the front stayed confined to the inner-shelf, while in August and September, with the prevalent upwelling favorable winds, it migrated further offshore to the shelf edge. In this period the salinity was associated with the upwelled waters and no clear signal of the WIBP existed, as continental runoff was minimal

In early October 2009, with southerly winds and increasing river flow, the penetration of warm and saline waters on the shelf was triggered and coexisted with the coastal WIBP (9.05°W-8.9°W). This warming tendency of the surface shelf waters was interrupted by an upwelling event occurring early November 2009 when cold waters spread seaward. With returning southerly winds, the surface temperature remained at the level of the upwelling period (between 15°C and 16°C) in fig. 4.1b), while at the bottom (Fig. 4.1e), temperature rose to values similar to the surface, breaking the summer stratification.

4.3.3 Events

Within the annual cycle of November 2008 to December 2009, five distinct periods can be identified from the point of view of the shelf hydrography. For each period a name was given with its main characteristics. In November and December 2008 is the *Autumn upwelling*, January 2009 to mid February 2009 is the *High variability winter*, March to June 2009 is the *Spring upwelling*, July 2009 to September 2009 is the *Summer upwelling* and October 2009 to December 2009 is the *Autumn downwelling*.

Based on the observational data from the near-monthly cruises and the model outputs, events during each of the five aforementioned periods were analyzed in more detail. In every period at least one cruise was available to be compared with the modeling results.

Autumn Upwelling - November/December 2008

At the end of October, the previous state of warm and saline waters at the surface was abruptly interrupted by a strong upwelling period that lowered the surface temperature and salinity across the shelf. November and three weeks of December 2008 were characterized by

persistent upwelling dominance, and cooling of the temperature on the shelf. An example of this autumn upwelling, was sampled in the cruise of 14 November represented in Fig. 4.5.

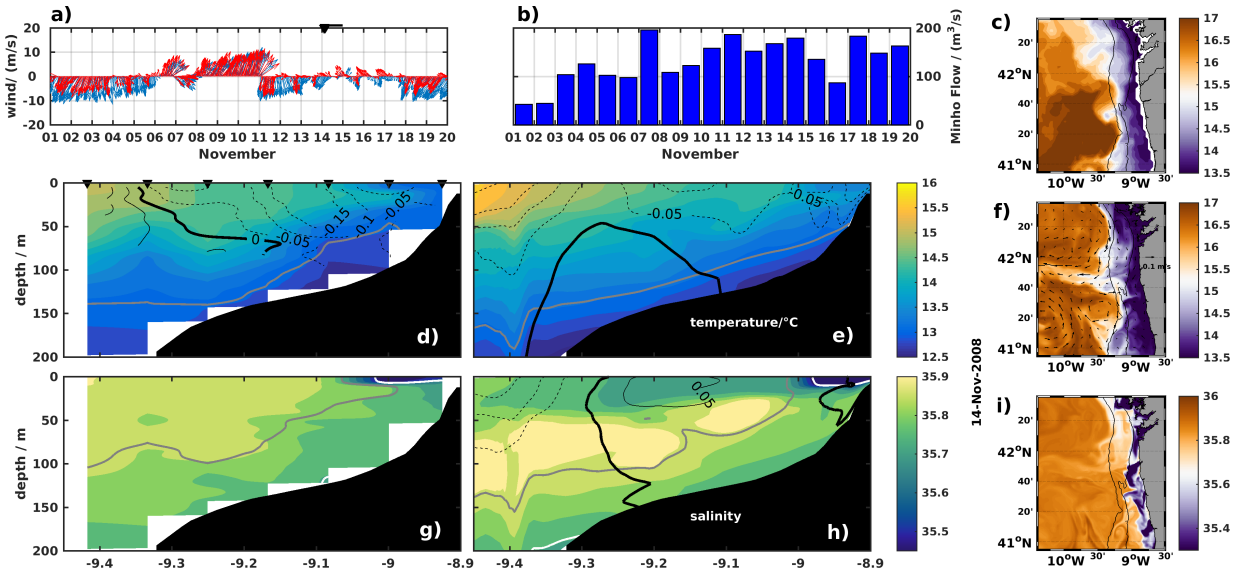

Figure 4.5: Time series of (a): WRF wind at the mADCP location (red) and the Silleiro buoy (blue) with indication on top of the temporal period of the CTD transect (dark triangle) and the day of the averaged model transect (dark line), (b) River Minho flow at the Frieiras Dam. Vertical transects of (d,e) temperature and (g,h) salinity for 14 November 2008 from CTD (d,g) and the model (e,h). When available, in the temperature transects are contoured the alongshore current velocity in m/s (dark contours), and isopycnals 27 kg/m^3 (gray) and 26 kg/m^3 (white). In the salinity transects are contoured the cross-shore current velocity in m/s (dark contours - on the model) and isolines of spiciness 2.5 kg/m^3 (gray) and 2.2 kg/m^3 (white). Maps of (c) 13 to 15 November 2008 composite SST from AVHRR, simulated (f) surface temperature with surface currents superimposed and (i) surface salinity for 14 November 2008.

The upwelling can be seen in the cold and less saline conditions near the bottom with an ascension of the 27 kg/m^3 isopycnal from 140 m offshore to ∼50 m near the coast, observed in both the sampled section (Fig. 4.5d) and the modeled section (Fig. 4.5e). An equatorward jet located coastward of 9.3°W was also associated with the upwelling event. The presence of a coastal trapped river plume was evident on the top 20 m of the salinity fields (Fig. 4.5g and h), spreading to 9°W. Clear atmosphere on 14 November, allowed a good comparison between the observed satellite and the modeled SST (Figs. 4.5c and f), showing the coastal upwelling and filaments around 42°N and 41°N, likely associated with offshore eddies as can be seen in the surface velocity. The surface salinity (Fig. 4.5i) depicted the offshore advection of the plumes from the main continental fresh water sources,

namely Rías Baixas and rivers Minho, Lima, Cavado and Douro.

***High Variability Winter* (January to mid February 2009)**

The winter period was characterized by the largest variability of wind forcing (Fig. 4.1a). Cycles of 2-4 days of downwelling favorable southerly winds were interleaved with 1-2 days of upwelling favorable northerly winds. During this period, the temperature and salinity were almost vertically homogeneous shelf-wide. Since December 2008, continental runoff was high on the Northwestern Iberia (river Minho flow >400 m^3/s in December, Fig. 4.6b), which contributed to the strengthening of river plumes during this period. Under downwelling favorable winds, onshore flux was observed in the surface layers and the plume steepened. An example of this situation was observed in the cruise of 13 January, taking place in the wake of a peak of downwelling favorable wind (Fig. 4.6c,d,e,f,g,h,i). An almost vertical front was observed around 9.1°W separating the plume from the offshore waters. Associated with the geostrophic balance at the frontal region, a poleward current was intensified during the survey on the inner-shelf. The same frontal zone was reproduced by the model at 9.05°W. On 27 January (Fig. 4.6j,k,l,m) one situation of upwelling was depicted by the model results, in which the fresh water plume was restricted to the surface and spread offshore. Equatorward currents were quickly setup on the inner shelf during upwelling and intensified at the surface.

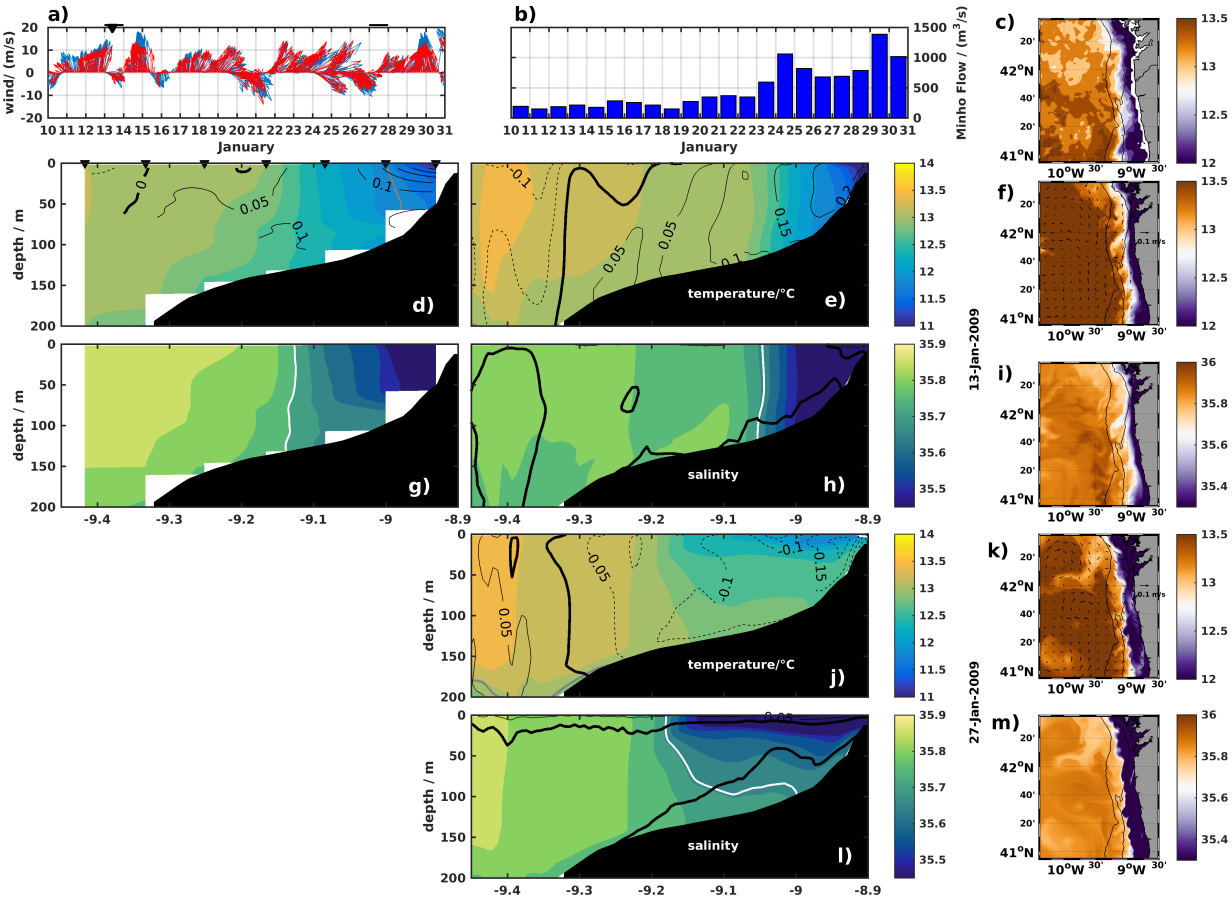

Figure 4.6: Time series of (a): WRF wind at the mADCP location (red) and the Silleiro buoy (blue) with indication on top of the temporal period of the CTD transect (dark triangle) and the day of the averaged model transects (dark lines), (b) River Minho flow at the Frieiras Dam. Vertical transects of (d,e) temperature and (g,h) salinity for 13 January 2009 from CTD (d,g) and the model (e,h). When available, in the temperature transects are contoured the alongshore current velocity in m/s (dark contours), and isopycnals 27 kg/m^3 (gray) and 26 kg/m^3 (white). In the salinity transects are contoured the cross-shore current velocity in m/s (dark contours - on the model) and isolines of spiciness 2.5 kg/m^3 (gray) and 2.2 kg/m^3 (white). Maps of (c) 12 to 14 January 2009 composite SST from AVHRR, simulated (f) surface temperature with surface currents superimposed and (i) surface salinity for 13 January 2009. (j,k,l,m) are equivalent to (e,f,h,i) for 27 January 2009.

Spring Upwelling - March to June 2009

Following the period of short scale variability with prevalence of downwelling favorable winds, the spring period (March to June) was characterized by the upwelling favorable winds interleaved with downwelling, as well as a progressive warming at the surface layer

and consequent increasing stratification (Figs. 4.1 and 4.2).

The cruise of 22 June was underway during the relaxation of a strong upwelling event and onset of a coastal poleward current. The observations (Fig. 4.7l,o) show a barotropic poleward current inshore of 9.1°W, while offshore the current was equatorward at the surface 20 m and poleward below. The model (Fig. 4.7m,p) reproduced the observed poleward currents at the coast and the slope with intensities of about 0.05 m/s and 0.1 m/s, respectively.

In early June, intense southwesterly winds were related to a stormy event ending 11 June (Fig. 4.7i). During this event, downwelling occurred, with shelf surface waters flowing shoreward to be subducted near the shore, as seen by the downward slope of the $27kg/m^3$ isopycnal and $2.5kg/m^3$ spiciness at the bottom on the 10 June transect (Fig. 4.7a,c). Poleward flow was prevalent on the shelf and intensified near shore, transporting fresh waters from southern rivers into the Rías Baixas, similarly to the January event. River Minho flow increased from $<100m^3/s$ before the stormy event until stabilizing at about $200m^3/s$ after 14 June (Fig 4.7j). The strong upwelling event followed, from 12 to 21 June. On 16 June (Fig 4.7e-h) the upwelling event was fully developed, in which surface-intensified equatorward currents were observed onshore of 9.3°W, and the top 30 m was flowing in the southwestward direction. A region of SST colder than 15°C was observed on the inner shelf between 41°N and 42°N (Fig. 4.7f). Also at the surface, warm and fresh water plumes were flowing out of the Rías Baixas and masked the recently upwelled colder waters.

Figure 4.7 *(facing page)*: Time series of (i): WRF wind at the mADCP location (red) and the Silleiro buoy (blue) with indication on top of the temporal period of the CTD transect (dark triangle) and the days of the averaged model transects (dark lines), (j) River Minho flow at the Frieiras Dam. Vertical transects of (l,m) temperature and (o,p) salinity for 22 June 2009 from CTD (l,o) and the model (m,p). When available, in the temperature transects are contoured the alongshore current velocity in m/s (dark contours), and isopycnals 27 kg/m^3 (gray) and 26 kg/m^3 (white). In the salinity transects are contoured the cross-shore current velocity in m/s (dark contours - on the model) and isolines of spiciness 2.5 kg/m^3 (gray) and 2.2 kg/m^3 (white). Maps of (k) 21 to 22 June 2009 composite SST from AVHRR, simulated (n) surface temperature with surface currents superimposed and (q) surface salinity for 22 June 2009. (a,b,c,d) and (e,f,g,h) are equivalent to (m,n,p,q) for 10 June 2009 and 16 June 2009, respectively.

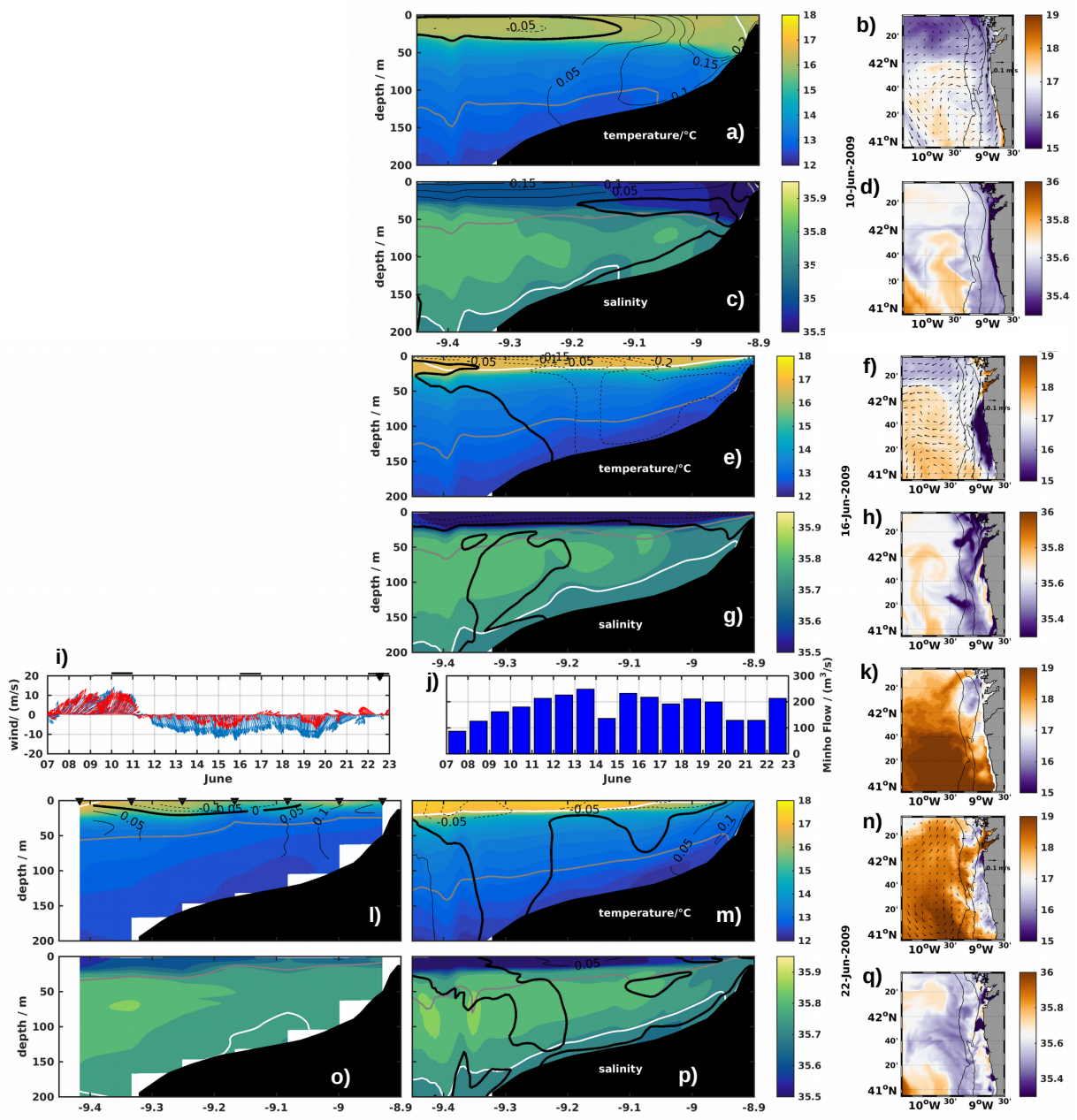
a)
b)
c)
d)
e)
f)
g)
h)
i)
j)
k)
l)
m)
n)
o)
p)
q)
temperature/°C
salinity
depth / m
wind/ (m/s)
June
Minho Flow / (m³/s)
10-Jun-2009
16-Jun-2009
22-Jun-2009

Summer Upwelling - August/September 2009

A cruise performed on 17 September illustrated the typical conditions of upwelling prevalent in the months of August and September 2009 (Fig. 4.8). Equatorward flow was observed inshore of 9.25°W and a poleward current was located offshore (Fig. 4.8d).

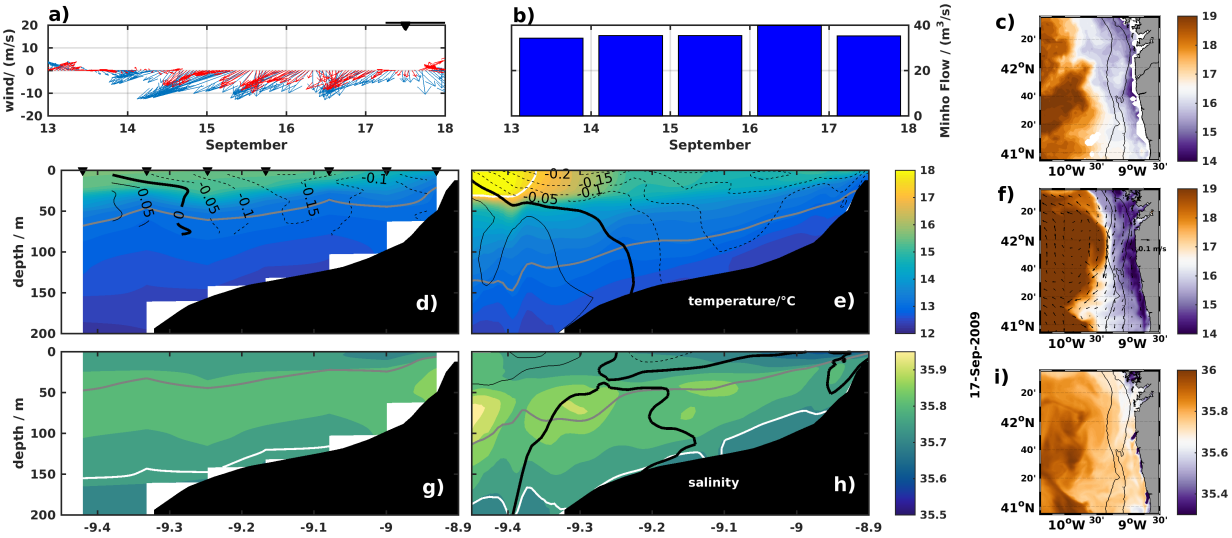

Figure 4.8: Time series of (a): WRF wind at the mADCP location (red) and the Silleiro buoy (blue) with indication on top of the temporal period of the CTD transect (dark triangle) and the day of the averaged model transect (dark line), (b) River Minho flow at the Frieiras Dam. Vertical transects of (d,e) temperature and (g,h) salinity for 17 September 2009 from CTD (d,g) and the model (e,h). When available, in the temperature transects are contoured the alongshore current velocity in m/s (dark contours), and isopycnals 27 kg/m^3 (gray) and 26 kg/m^3 (white). In the salinity transects are contoured the cross-shore current velocity in m/s (dark contours - on the model) and isolines of spiciness 2.5 kg/m^3 (gray) and 2.2 kg/m^3 (white). Maps of (c) 16 to 18 September 2009 composite SST from AVHRR, simulated (f) surface temperature with surface currents superimposed and (i) surface salinity for 17 September.

The model simulated a similar circulation structure to the observations, with equatorward currents on the shelf and a subsurface poleward current centered around the slope (Fig. 4.8e). In the model the surface front between upwelled waters and the offshore warm waters was located at 9.4°W, while in the observations it was offshore of the westernmost CTD station, as evidenced by the SST map (Fig. 4.8c).

River discharges were low (<50 mm/day from River Minho, Fig. 4.8b), and fresh water plumes were less noticeable on the surface salinity fields than in the other periods, just protruding at their respective river mouths (Fig. 4.8i).

Autumn Downwelling **- October to December 2009**

The relaxation of a post-summer upwelling event with westerly winds was found during the 10 November cruise (Fig. 4.9c-h). A surface mixed layer persisted at the top 50 m on the outer shelf, with strong stratification down to 150 m depth. The top 50 m layer of warm waters was associated with a surface intensified equatorward flow across the slope. Nearshore, the isotherms and isohalines were elevated towards the coast as a result of the previous upwelling event. On 19 November (Fig. 4.9i-l), downwelling favorable winds were prevalent and river flow was higher (river Minho flow reached 600 m^3/s). On the inner-shelf, a poleward current of about 0.2 m/s developed, associated with the downsloping of the surface layer isothermals and isohalines as a response to the southerly winds, as well as the presence of fresh water plumes close to the shore.

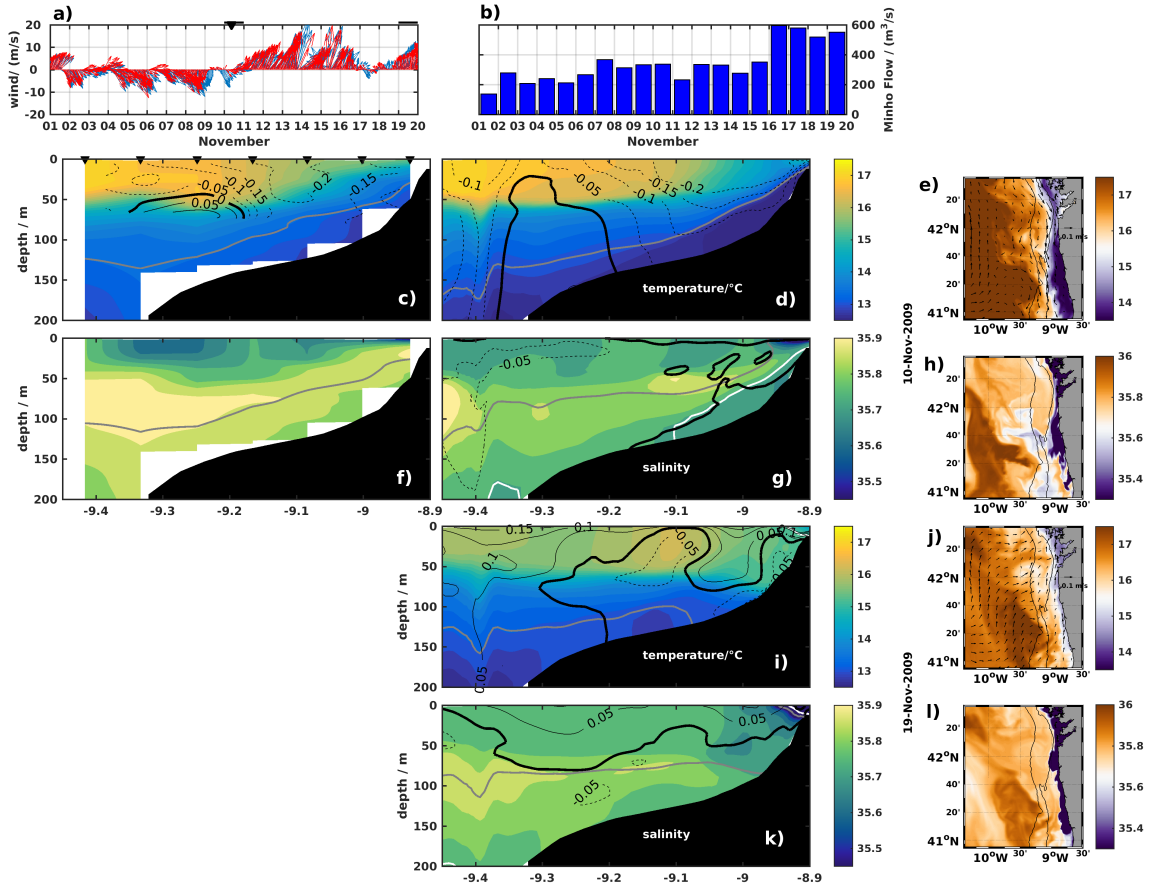

Figure 4.9: Time series of (a): WRF wind at the mADCP location (red) and the Silleiro buoy (blue) with indication on top of the temporal period of the CTD transect (dark triangle) and the day of the averaged model transects (dark lines), (b) River Minho flow at the Frieiras Dam. Vertical transects of (c,d) temperature and (f,g) salinity for 10 November 2009 from CTD (c,f) and the model (d,g). When available, in the temperature transects are contoured the alongshore current velocity in m/s (dark contours), and isopycnals 27 kg/m^3 (gray) and 26 kg/m^3 (white). In the salinity transects is contoured cross-shore current velocity in m/s (dark contours - on the model) and isolines of spiciness 2.5 kg/m^3 (gray) and 2.2 kg/m^3 (white). Maps of simulated (e) surface temperature with surface currents superimposed and (h) surface salinity for 10 November 2009. (i,j,k,l) are equivalent to (d,e,g,h) for 27 January 2009.

4.3.4 Surface Fields

Velocity EOF analysis

The variability of the surface velocity on the NWIM was assessed by means of an rvEOF. The first two modes of the rvEOF are shown in Fig. 4.10a and b with the PC time

series of mode 1 (2) superimposed on the surface alongshore wind (across-shore wind) at the Silleiro buoy location.

Mode 1 accounted for 37.1% of the total variance and the spatial EOF was roughly oriented alongshore on the shelf (Fig. 4.10c) with a strong signal ($\sim$0.025). Offshore of the shelf, the spatial EOF was mostly directed southwest-northeast with a significantly weaker signal ($<$0.01), except along two latitudinal bands, around 42°N and 41°N. The PC time series of mode 1 was correlated (r=0.83) with the alongshore wind (meridional component) at the Silleiro buoy position, which could be associated with the generation of the upwelling jet/coastal poleward current in the shelf as a response to wind forcing.

Mode 2 accounted for 10.6% of the total variance and the spatial EOF was directed mainly in the northwest-southwest direction, with a tendency to be across-shore on the shelf (Fig.4.10d). Its intensity is more evenly spread in most of the region (about 0.015), being stronger than 0.02 on the shelf north of 42°N and lower than 0.01 on the shelf south of 41.5°N. The PC time series of mode 2 were correlated (r=0.73) with the across-shore winds (zonal component) at the Silleiro buoy position.

The higher modes (not shown) were mainly represented by mesoscale offshore features, which are strongly influenced by the model internal variability and can skew the model results over scales of weeks to months. The reconstruction of the ocean currents exclusively with the first 2 modes allowed a filtering of these features. The increase in model skill can be seen in the reconstruction of the along- and acros-shore modeled velocity at the Silleiro buoy (Fig. 4.11). The usage of 2 modes increased the correlation between modeled and observed V and U components by 0.05 and 0.21, respectively. With only these two modes, the standard deviation of the reconstruction decreased, to the point where it was lower than the observations, although the RMSE was still closer than the original model outputs.

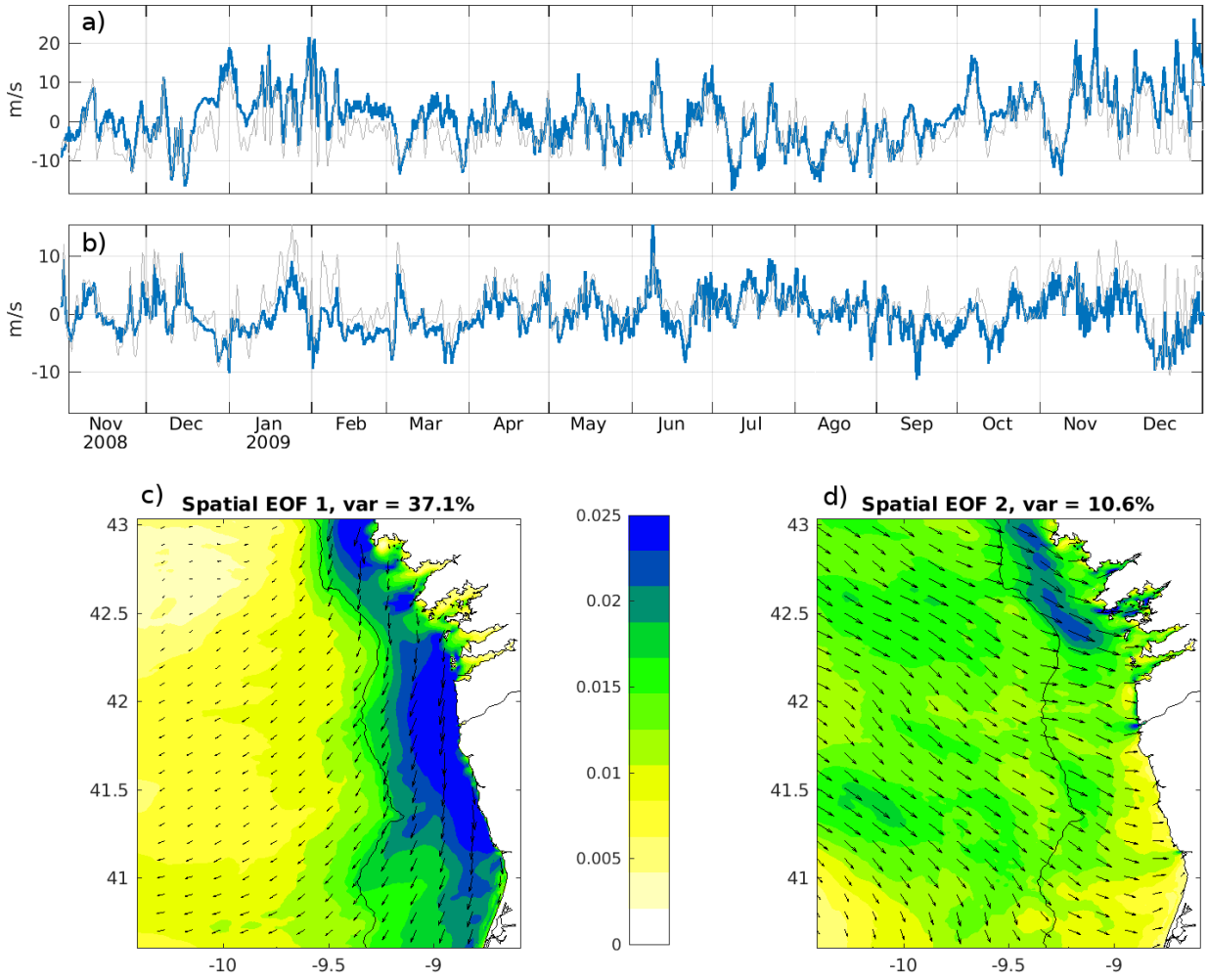

Figure 4.10: Real-Vector EOF of surface currents. PC time series of: a) mode 1 (blue) superimposed on the WRF meridional wind at Silleiro buoy (gray), b) mode 2 (blue) superimposed on the WRF zonal wind at Silleiro buoy (gray). Spatial EOF of (c) mode 1 and (d) mode 2, where the vectors indicating the direction are superimposed on the colored intensity. The contribution of each mode in a point is obtained (in m/s) by multiplying the value of the spatial EOF in that point by the PC time series.

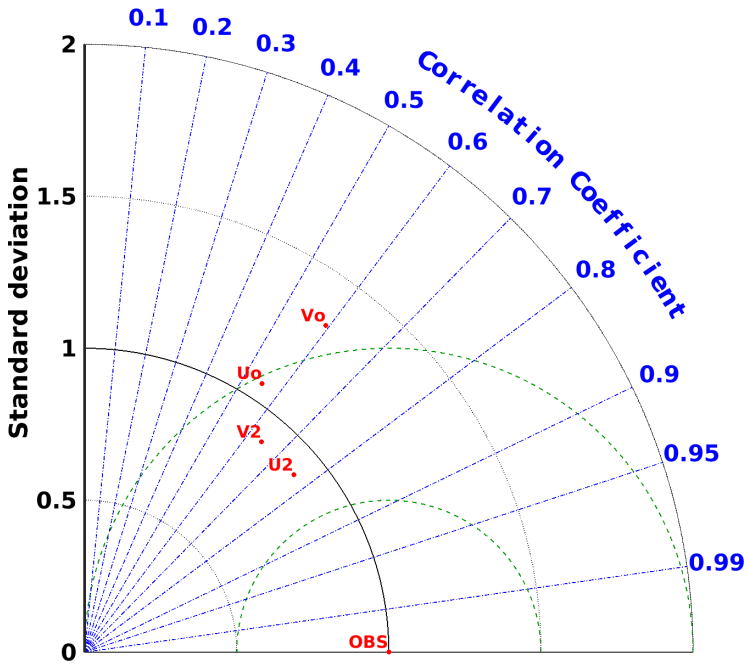

Figure 4.11: Taylor diagram for the original model velocities (Uo,Vo) and reconstructed with PC time series of the first two modes (U2,V2).

Temperature EOF analysis

After the rvEOF analysis of the surface currents, an EOF analysis of the SST is presented here. Due to the strong signature of the temperature seasonal cycle, the temperature was filtered to remove cycles of periods higher than 100 days. For that, at each grid point time series, a high pass filter was applied.

The EOF analysis of modes 1 and 2 are shown in Fig. 4.12, explaining 50% and 9.03% of the total variance, respectively. Both PC time series show larger oscillations on the months of June through September, coinciding with the period when the PC of mode 1 was in phase with alongshore winds at Silleiro buoy. On the rest of the studied period, the lower fluctuation of the temporal modes indicated that the temperature mainly followed the seasonal cycle.

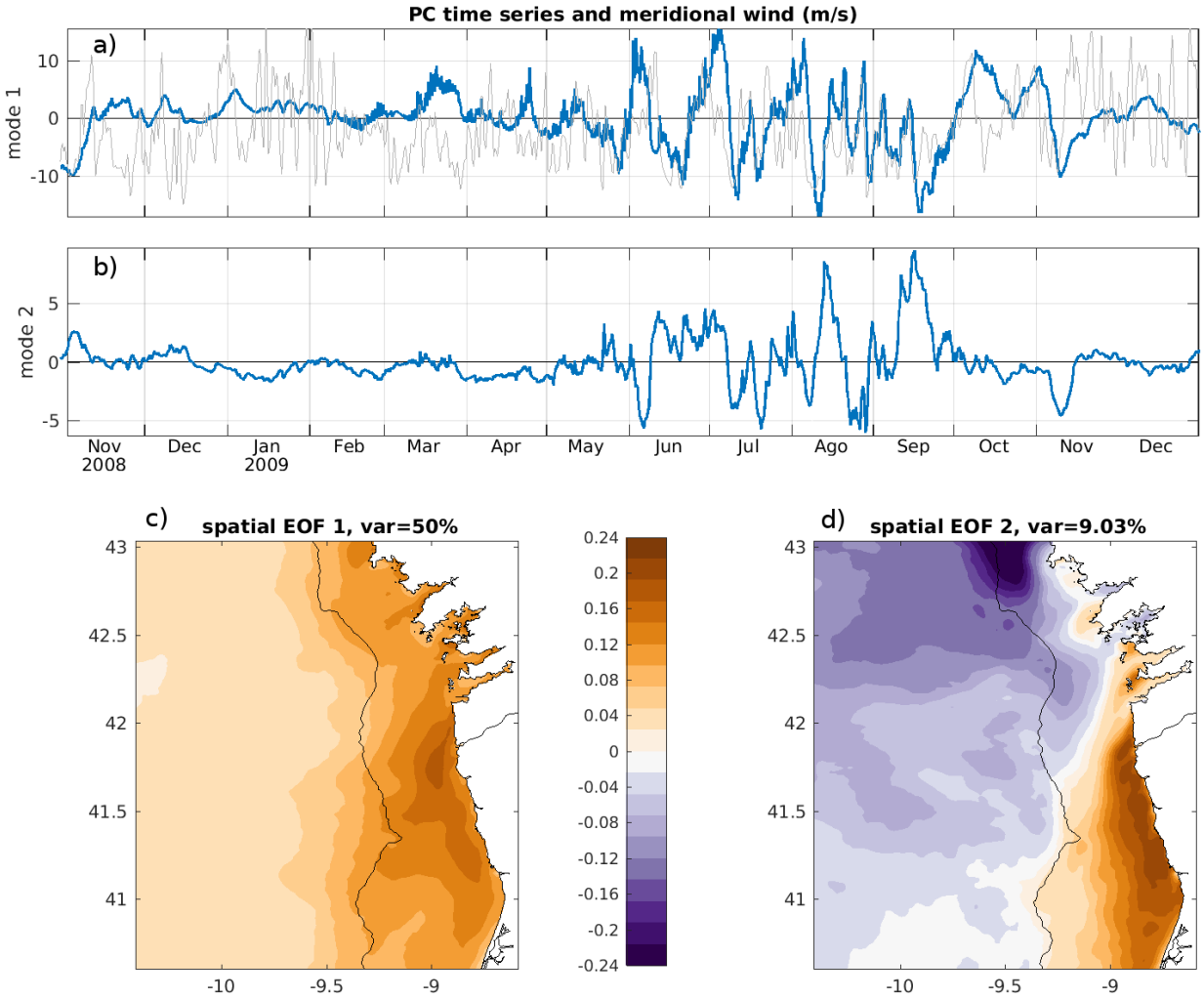

Figure 4.12: EOF of sea surface temperature. PC time series of: a) mode 1 (blue) superimposed on the WRF meridional wind at Silleiro buoy (gray), b) mode 2 (blue). Spatial EOF of (c) mode 1 and (d) mode 2. The contribution of each mode in a point is obtained (in °C) by multiplying the value of the spatial EOF in that point by the PC time series.

The spatial EOF of modes 1 and 2 (Fig. 4.12c and d) show strong signals on the shelf between around 41°N and 42°N. Although intensified here, the mode 1 is positive in all the domain. The stronger signal extends further offshore from the shelf at around 41°N, likely associated with the tendency of filament formation here. On mode 2, the shelf strong signal is opposite to the rest of the domain, with the maximum opposite signal near cape Finisterre (43°N). This way, due to mode 2, lower (higher) temperatures near cape Finisterre correspond to higher (lower) temperatures south of cape Silleiro. The upwelling center observed South of cape Silleiro in July 2009 (Chapter 3) was enhanced during the two upwelling events by the joint effect of cooling in modes 1 and 2.

Salinity EOF Analysis

The EOF analysis was also performed on the surface salinity field (Fig. 4.13). The first two modes explained 39.3% and 13.9% of the variance of the surface salinity. As was previously observed (Figs. 4.1 and 4.2), surface salinity had lower variability in the offshore region (with oscillations of about 0.2 around 35.7) than in the coastal region with dips of salinity >1. This way, the regions of higher variability were concentrated on the coast, particularly near the main river systems and inside Rías Baixas, as visible on the spatial EOF patterns. Mode 1 can also be associated with continental runoff by the correlation of its PC time series with river Minho flow (r=0.77), in which higher river outflow (January/February 2009, November/December 2009) corresponded to positive PC while lower river outflow (August/September 2009) was related to a negative PC.

The spatial EOF of mode 2 had negative signal extending offshore in front of the river mouths, representing the extension of river plumes across the shelf. The oscillations of the PC time series of mode 2 were larger in periods of high river flow, although being mostly negative under downwelling periods, and positive on upwelling periods. This way, mode 2 contributed to diminishing (increasing) salinity on the shelf under upwelling (downwelling) due to the plume offshore transport. Additionally, the most noticeable positive signal occurs in February/March 2009 when river discharges were decreasing, while negative signals appear in January 2009 and November 2009 when river discharges were increasing.

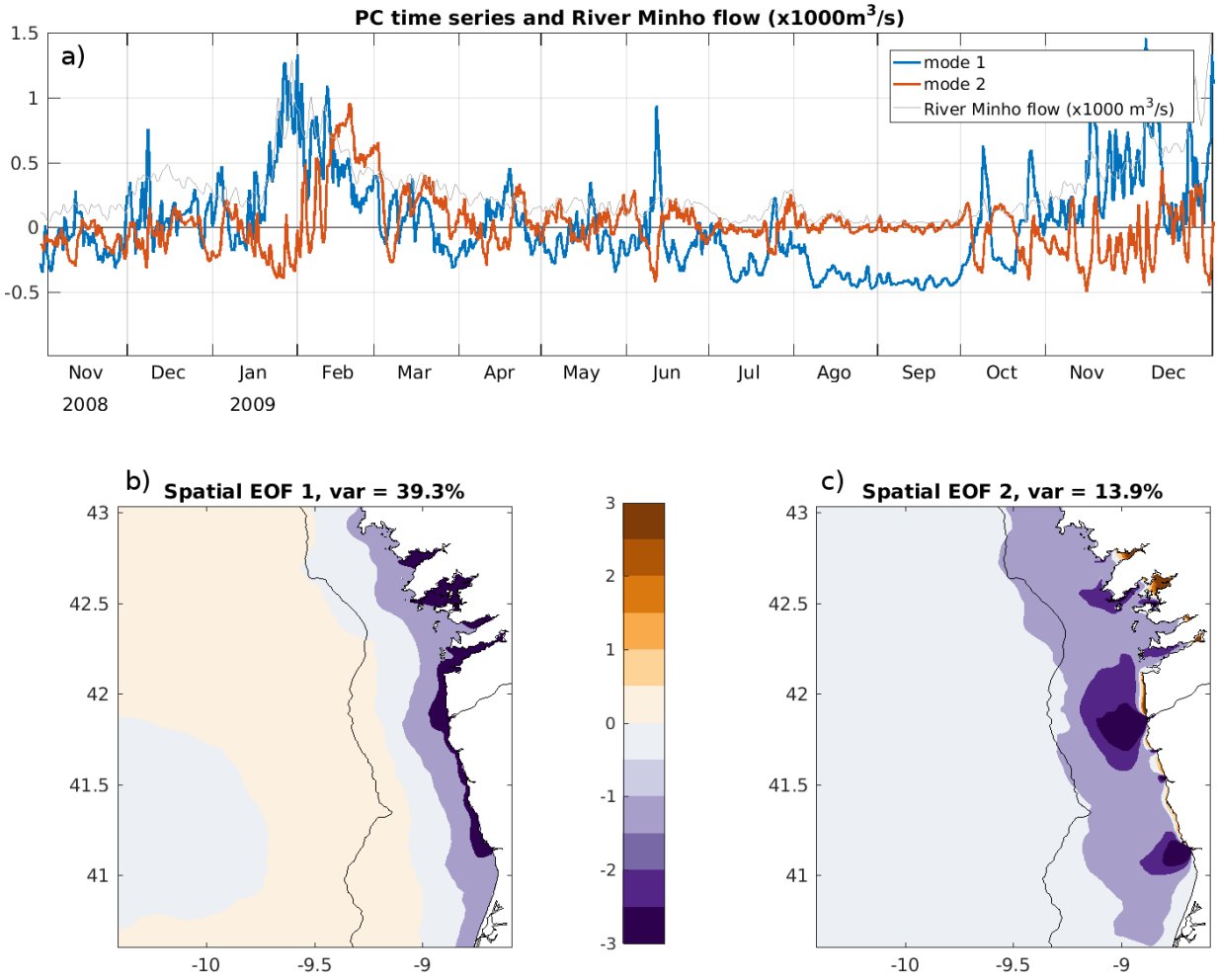

Figure 4.13: EOF of the surface salinity. PC time series of: a) mode 1 (blue), mode 2 (red) superimposed on the River Minho flow (gray). Spatial EOF of (b) mode 1 and (c) mode 2. The contribution of each mode in a point is obtained by multiplying the value of the spatial EOF in that point by the PC time series.

4.4 Discussion

A full seasonal cycle of the Northwestern Iberian shelf hydrography was studied based on a set of observations, consisting on an ADCP deployment (mADCP) and quasi-monthly across shelf transects. On the other hand, a numerical modeling configuration was specifically designed to complement the observational information, providing the three dimensional evolution of the hydrography and currents through the seasonal cycle.

4.4.1 Modeling Considerations

Regional models, such as ROMS-AGRIF, need boundary and initial conditions from observations (typically oceanic climatologies, such as World Ocean Atlas) or from other models with larger domains. In the case of the configuration developed for this chapter (NWIc), the model used was the IBI-MFC reanalysis by CMEMS with 1/12° horizontal resolution. This is a model reinitialized every week that uses assimilation of Argo floats and satellite products (*Aznar et al.*, 2016), providing realistic hydrographic conditions with reasonably correct large scale distribution of water masses.

The applied ROMS-AGRIF technique provides an improvement of resolution, through a first offline nesting from the large domain (IBI-MFC reanalysis) to the NWIc domain. Another higher resolution domain (NWIc-1) was coupled in an online two-way nesting, achieving a final horizontal resolution of 1/150° (about 550 m). This configuration was able to reproduce the several processes occurring in the period of study (November 2008 to December 2009). The validation of the model results was made by a comparison with the observational data set, providing confidence in the model results to study the hydrography and dynamics of this region.

In the absence of observational data, non-assimilated regional models, like NWIc, are suitable tools to obtain continuous hydrographic and dynamical fields in a limited region. Although, since those models are forced through the lateral boundaries, internal variability inside the domain is allowed, specifically affecting the mesoscale eddy field (*Peliz et al.*, 2007, 2009). The internal variability degrades the direct comparison with respect to observations, as eddies are not always located at the same time, place and shape as the real oceanic eddies. Consequently, in the case of the NWIc, the skill between model and Silleiro buoy improved when the first two rvEOF modes for surface velocities were taken into consideration (Fig. 4.10). Similarly to the NWIc, the rvEOF analysis applied to surface currents on the Eastern North-American shelf (*Kaihatu et al.*, 1998) separated the unidirectional shelfwide flows in the first two modes from the mesoscale eddy-like features

of the higher modes.

Resolving the wind stress curl at the shelf is important for the correct simulation of the circulation in this region (*Torres et al.*, 2003). For this reason, a 3 km resolution atmospheric model, previously validated (Section 1.4.4), provided a reliable wind field to be used as forcing on the oceanographic model NWIc.

The main simplification of the NWIc was the absence of tidal forcing, which induces significant periodic currents shelfwide in the near inertial band (*Marta-Almeida and Dubert*, 2006; *Herrera et al.*, 2008; *Quaresma and Pichon*, 2013). Even though tides contribute to the mixing of the water column on the shelf, tidal effects were left out of the analysis, as high frequency phenomena was not the scope of this thesis and the residual currents are weak in the region (*Quaresma and Pichon*, 2013).

The seasonal cycle in the mADCP location and the Silleiro buoy showed in general a good correspondence between observations and the modeling results. It should be stressed out that in both locations the bathymetry slopes steeply and had to be smoothed to be introduced in the model. Specifically, the Silleiro buoy is located on the slope region and, in the mADCP location (72 m depth), the bathymetry slopes from the coast to 100 m depth in 7 km distance in the cross-shelf direction.

The bias of the surface temperature observed in the Silleiro buoy during the summer (Fig. 4.2) was likely associated with the position of the upwelling front, more inshore in model than observations, as is shown in the surface SST of the *summer upwelling* event (Fig. 4.8). In the near shore bottom layers, a bias was also present during the *spring upwelling* (Fig. 4.1).

The modeled velocity field matched reasonably the observed one near shore at the mADCP location and offshore at the Silleiro buoy. Generally the model reproduced equatorward flows during upwelling events and poleward flows during relaxation periods, with some exceptions, such as the under-prediction of poleward flows in July 2009. The circulation reversals during relaxation of upwelling favorable winds are known to be under-predicted by numerical models (*Kuebel Cervantes and Allen*, 2006).

In general, the model had the ability to generate and advect freshwater plumes from the main river systems, whose flows were available daily. The modeled plume spread offshore with similar salinity to observations across the Silleiro transect (Fig. 4.4), although not always exactly on the same day. The spreading of a freshwater plume on the shelf is mainly controlled by the offshore/equatorward and onshore/poleward directions in response to upwelling/downwelling favorable winds (*Otero et al.*, 2013). This way, buoyant plumes behave in a certain way as lagrangian objects, and so are naturally difficult to simulate for long periods after their generation on the river mouths.

4.4.2 Processes of the Shelf Circulation

The region in front of cape Silleiro, where the transects were performed, has its own particularities within the NWIM. It is located between Rías Baixas (north of the section) and the southern smooth coastline, characterized by the presence of rivers with high inflow (particularly river Minho and Douro). Alongshore flows on this coast are mainly wind driven. Downwelling events promote northward transport of coastal waters (such as the WIBP) through the Silleiro transect into the Rías Baixas (*Otero et al.*, 2008; *Sousa et al.*, 2014). On the other hand, under upwelling, the waters exported from Rías Baixas are transported equatorward by the upwelling jet, crossing the Silleiro transect. The main oceanographic aspects of the four season are highlighted below.

Autumn

In a typical autumn, the hydrographic features on the shelf results from the IPC presence on the slope/shelf, bringing southern oceanic warm and saline waters into the shelf and eroding the thermal stratification. This occurs in association with the increasing frequency of atmospheric low pressure systems passage during this time of the year, contributing to the prevalence of southerly winds. However, the autumn of 2008 was a clear exception to this situation, as in November and December northerly winds ruled, generating coastal upwelling of colder and fresher deep waters. The colder than usual temperatures for the months of November 2008 and December 2008 were evident in the SST anomalies with respect to the period 2001-2016 (Fig. 4.14) with anomalies of -2°C. The observed IPC during this autumn was weak (*Teles-Machado et al.*, 2015) and its influence on the shelf surface waters was limited to an increase of salinity in the outer shelf in a few downwelling events (Fig. 4.4). A consequence of the persistent upwelling was the presence of filaments throughout November and December, which are rare for these months in the NWIM, and hence usually not studied (Chapter 2,*Haynes et al.*, 1993a). The exceptionality of this autumn had consequences on the distribution of marine species (*Moita et al.*, 2016), giving rise to the flushing out from the region of species of phytoplankton (*Dynophisis Acuta*) and being almost undetectable for several years. The autumn of the following year (in 2009), was more typical, even in the presence of cold anomalies of October-December in relation to the SST mean of 2001-2016 (Fig. 4.14).

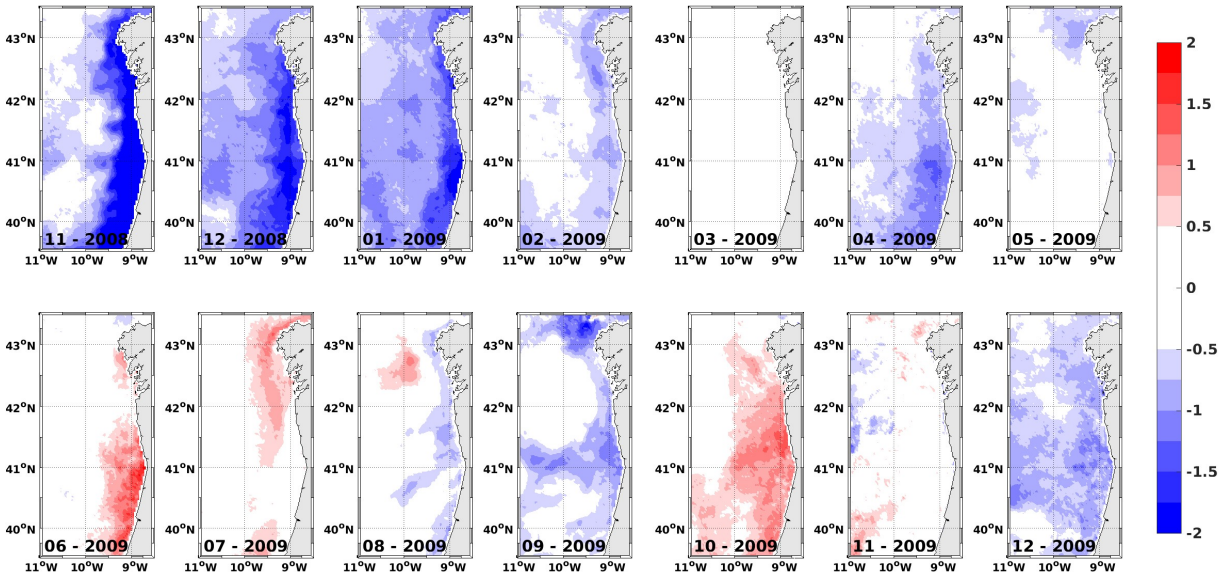

Figure 4.14: SST anomalies with respect to the 2001-2016 monthly climatologies. Number of the month and year represented in the bottom of each panel

Another typical feature of the autumn is the generation of the WIBP, as a result of the increasing river inflow. Such feature was absent through almost all autumn 2008, being only generated in late December, while in 2009 the WIBP appeared in the cape Silleiro region from early October onward (Fig. 4.4). This is so for two reasons, on one hand in 2008 the river flows were lower than in 2009. On the other hand, in autumn 2008, the fresh waters from the continental runoff were rapidly exported offshore (through the surface Ekman layer), while in 2009, the prevalence of southerly winds constrained these waters to the coastal region.

Further south, in the Gulf of Cádiz, *Garel et al.* (2016) observed prevalence of equatorward flows on the inner-shelf during the November-December 2008 period, in concordance with the tendency for equatorward flows on the WIM, reported above.

In the Northern coast of the Iberian Peninsula, in Bay of Biscay, observations of alongshore currents on the inner-shelf, concurrent with the autumn 2009, were described by *Kersalé et al.* (2016). Poleward events ruled their observations in November, specifically between 31-October and 11-November associated with strong westerly winds over the Bay of Biscay (downwelling favorable), coinciding with the strong upwelling event off cape Silleiro (Fig. 4.9). Such pattern, of opposing upwelling and downwelling in the northern and western Iberian coasts, respectively, was reported to occur in the summer (*Torres et al.*, 2003).

The break of stratification, as consequence of the erosion of the seasonal thermocline, occurred in both autumn 2008 and 2009, after events of upwelling. In 2008, the stratification was reduced in late October, suggested by the sudden surface temperature decrease across the shelf in Fig. 4.4. In 2009, the upwelling event of early November marked the end of the stratification off cape Silleiro, as well as in Bay of Biscay (*Kersalé et al.*, 2016).

Winter

Associated with the winter season, highly variable winds in which events of strong southerlies (downwelling favorable) are interleaved with short periods of northerlies (upwelling favorable). As consequence, deep (around 200 m depth) mixed layers are generated, homogenizing the shelf waters. High river inflow is responsible for the presence of fresh water plumes on the surface (WIBP, *Peliz et al.*, 2002), restricted to the coastal region due to the mainly downwelling favorable winds. This general description applies to the denominated "high variability winter" period of January 2009 to mid February 2009. Similarly, after mid November 2009 can be considered a highly variable winds period with prevalence of downwelling occurred, giving rise to the documented strong WIBP of the winter 2009/2010 (*Otero et al.*, 2013; *Mendes et al.*, 2016).

During downwelling favorable winds, buoyant plumes accumulate in the coastal region due to the convergent surface Ekman layer (*Lentz and Largier*, 2006). As a consequence, the plumes deepen near the coast and the halocline separating the plumes fresh waters from oceanic waters becomes nearly vertical (Fig. 4.9). Poleward flow is associated with horizontal across-shore density gradients and is reinforced by wind driven dynamics, hence the plume flows in the poleward direction with its highest intensity (velocities >0.2 m/s in Fig. 4.6), and has been documented to reach 1 m/s on extreme scenarios (*Mendes et al.*, 2016). Consequently a continuity of the plume between river Douro and the northern part of the NWIM can be observed, as the poleward flowing WIBP is originated in the southern rivers and tends to flow into the Rías Baixas (*Sousa et al.*, 2014).

In periods of downwelling relaxation or upwelling, the plumes are exported offshore and become thinner (*Lentz and Largier*, 2006). These episodes occurred sporadically in the winter season, in which the plumes were uplifted taking the shape of a surface lense (26 January 2009 in Fig. 4.6), although they were retained trapped to the coast at 9°W near cape Silleiro (Fig. 4.4).

From February 2009 until the end of this month, the relaxation of downwelling favorable winds contributed to the offshore expansion of the fresh waters, previously accumulated in the coastal region and the Rías Baixas. The plume extended across the shelf, reaching the

Silleiro buoy (with salinity <35.4 in Fig. 4.2c), until suddenly disappearing early March, under a strong northwesterly winds event (Fig. 4.2a). An observational evidence of the early stage of the plume expansion on 13 February 2009 in front of cape Silleiro was documented by *Curros et al.* (2009) with surface salinity <35.7, found offshore at 9.25°W. *Varela et al.* (2005), *Nieto-Cid et al.* (2004) and *Otero et al.* (2010) also observed decrease of salinity on the outer shelf as consequence of upwelling periods in the end of the winter season. The offshore extension of the plumes in front of river mouths, in the form of bulges, are seen in the spatial EOF pattern of the second mode in the salinity EOF analysis (Fig. 4.13), with the corresponding PC intensified in February 2009.

In the salinity EOF analysis, the spatial EOF pattern of the first mode resembles the prototypical river plumes (*Horner-Devine et al.*, 2015), most notably bulging in front of river Minho and river Douro, and elongated near shore in the poleward direction. This structure prevailed in the January 2009 and early February 2009 with the highest values of the PC time series of the first mode. The offshore extension of the plumes in front of the river mouths was present on the spatial EOF patterns of the second mode, which became the prevalent feature after mid February as the PC time series of the second mode was high (Fig. 4.13). In *Otero et al.* (2008) similar spatial fields of the plumes in the NWIM were documented in the gradual transition from the confinement by downwelling favorable winds to the offshore expansion during their relaxation.

Spring

Starting in March 2009, stronger and longer upwelling events were observed, as is typical for a spring season. The SST anomalies in the months of March through June were weak in relation to the mean of the same months for the years 2001-2016 (Fig. 4.14).

Associated with the seasonal cycle of warming during spring, a gradual increase in temperature occurred at the surface (Fig. 4.2) promoting the increase in the stratification. Once the stratification was set up, a strong downwelling event occurring early June 2009 promoted convergence on the coast, increasing the temperature of the bottom inner-shelf layers (Fig. 4.1) and generating coastally trapped poleward currents. This event affected other parts of the WIM, as was observed with a thermistor chain moored further south (40.6°N) on the inner-shelf (30 m depth) (Dubert, personal communication). In that data set, the bottom temperature was observed to increase 4°C during the downwelling event as a result of the warming of all the water column and poleward velocities were above 0.25m/s. Unfortunatelly, this event was not observed in the Silleiro region (happening while the mADCP was on maintenance), but that temperature increase observed further

south, provide more confidence on the 3°C increase gave by the model here. These events of poleward currents transporting warm waters along the inner-shelf have been associated with the end of the upwelling season, when convergence of the waters above the seasonal thermocline occur (*Sordo et al.*, 2001; *Herrera et al.*, 2008). Additionally, these warm inner shelf poleward currents have not been extensively studied before the establishment of upwelling. However, the occurrence of downwelling pulses in June was documented by *Álvarez-Salgado et al.* (2002) and associated it with the increase of the bottom temperatures inside Ría de Vigo during the years 1987 to 1999.

Besides this event, poleward currents (>0.4m/s) were observed at the surface during other three downwelling periods (Fig. 4.1d), interleaved with the longer periods of upwelling but generating lower velocities (<0.2m/s). Although the stratification of the earlier events was low, poleward flows were in the form of baroclinic jets associated with vertical shear. Each of these events produced poleward transports in the order of 150 km in 5 days along the coastal region, being responsible for the exchange of biologic material between coastal regions, such as the estuaries in the south to the Rías Baixas in the north (*Moita et al.*, 2016).

The river flows were still high during spring, contributing to the existence of the WIBP. It was previously documented that plumes, generated during spring and summer, are warmed up when converged to the coastal region and Rías Baixas (*Barton et al.*, 2015). Its signature is also visible on the surface temperature fields when upwelling occurs after convergence, as the temperature of the upwelled waters is colder than the surface coastal waters. This situation was evidenced in the transect of 16 June 2009 (Fig. 4.7) with the plume of fresh waters leaving Rías Baixas being warmer than the oceanic temperature, and was previously documented by *Torres and Barton* (2007).

Summer

In the summer, upwelling events are prevalent and stratification of the water column due to the seasonal thermocline result in the formation of a surface front, separating cold recently upwelled waters onshore from warm offshore waters. This front outcrops near the coast, and under sustained upwelling, reaches the slope or goes even offshore. The early stages of the summer 2009 were documented in Chapter 3 and occurred in July, when the development of the front rapidly responded to cycles of upwelling and relaxation. The EOF analysis of the SST showed that the main surface temperature variability, at scales of days to weeks, was related to the upwelling/downwelling cycles when the seasonal thermocline was developed, during summer (Fig. 4.12). In August and September 2009 the frontal

region was located offshore near the shelf edge (Fig. 4.4), while filaments developed in the region (Fig. A.1).

In the NWIM, in association with upwelling favorable winds, an equatorward jet transports cold water along the slope from the lee of cape Finisterre. This equatorward jet, continues along the Rías Baixas region, which is strongly influenced by the presence of estuarine circulation (*Barton et al.*, 2015). Near cape Silleiro, the equatorward jet is deflected offshore (*Haynes et al.*, 1993b; *Barton et al.*, 2001; *Torres et al.*, 2003) and another coastal equatorward flow is developed on the inner shelf, associated with the upwelling center that extends South to the Porto region (41°N), already discussed in Chapter 3. This upwelling center was more prominent under northwesterly winds as it was seen in other periods, such as in the events of 16 June 2009 (Fig.4.7f) and 10 November 2009 (Fig.4.9e), suggesting that the enhancement of upwelling here occurs because winds become paralel to the coastline orientation (NNW-SSE, 348°T). South of Porto, reduced upwelling under northwesterly winds could be caused by the change in orientation of the coastline (NNE-SSW, 12°T). Under northerly or northeasterly winds, the upwelling was distributed more evenly along the NWIM, such as in the event of 17 September 2009 (Fig.4.8). A comparative study between the upwelling center and the southern region would contribute to explain the origin of the observed upwelling center. Another possible mechanism to explain upwelling centers was identified by *Pringle* (2002), claiming that equatorward flow in the presence of a poleward narrowing shelf induces additional upwelling. This is the case of the upwelling center of NW Iberia, in which the inner shelf narrows from Porto to cape Silleiro.

Upwelling and downwelling cycles also affect the region of Rías Baixas as studied by *Barton et al.* (2015, 2016). Upwelling of central waters occur inside these embayments and are exported to the shelf after thermohaline modifications (*Álvarez-Salgado et al.*, 2000). As a result, the warmer waters are flushed out in the SW direction, crossing the Silleiro transect above the locally upwelled waters, masking the SST signal (Fig. 4.8c).

On the EOF of the surface salinity, the negative PC time series of the first mode in the summer upwelling season is not only related to the lower river runoff generating less intense plumes, but also is suggestive of the surfacing of more saline central waters on the coast replacing the surface fresher waters exported to the region of the upwelling front (Chapter 3, *Rossi et al.*, 2013). The presence of fresh waters (salinity$<$35.6) on the shelf along summer was observed in 2002 (*Herrera et al.*, 2008) and was associated with an exceptionally high river inflow earlier that year. The aforementioned equatorward jet flowing along the slope, from cape Finisterre, transports fresher waters with northern origin, which could also explain the lower salinity on the frontal region.

In the upwelling season, events of poleward currents occurred on the shelf, either from wind relaxations (with the mechanism proposed by *Pringle and Dever*, 2009) or directly forced by southerly winds (as in July 2009). Apart from the coastal region, the development of poleward currents was also observed in slope during summer (for example in September 2009, Fig. 4.8c,d). Such currents have been associated with the previously documented IPC (*Frouin et al.*, 1990; *Peliz et al.*, 2003a), developing in late summer when winds become mainly southerly.

4.5 Conclusions

The main purpose of this chapter was to study, from the perspective of both observational and numerical modeling techniques, the NW Iberian upwelling system, characterized by the presence of cape effects (cape Finisterre), coastal embayments (Rías Baixas) and a rather straight coastline (south of cape Silleiro) with high inflow rivers (mostly Minho and Douro).

The realistic configuration developed here (NWIc) took into account different drivers of the local circulation (large scale circulation, river inflow, topography and atmosphere-ocean interactions), reproducing the complexity of the circulation at the different scales. On the other hand, the availability of observations of a full annual cycle in front of cape Silleiro, allowed the validation of the modeling results for this specific year (November 2008 - December 2009). The main validation procedure consisted in the comparison of measured and modeled time series of temperature, salinity and currents velocity, in a point near the coast (mADCP location) and offshore (Silleiro buoy). This was done by visually analyzing and inspecting of the time series, summarized with a Taylor diagram, showing spread results between different variables and locations, with better temperature all around and worse currents offshore. The comparison with data was also performed at the level of the vertical transects from the monthly cruises providing continuity across the shelf.

An analysis of different periods and particular events of the seasonal cycle was done, from which 5 were considered:

- November-December 2008: Cooling of the surface waters in the autumn season provided conditions for low stratification. With prevailing upwelling, the shelf circulation was mainly equatorward and waters remained cold.

- January-mid February 2009: In the midst of winter, the mixed-layer was deep enough to vertically homogenize the shelf waters. On the inner-shelf, the WIBP developed and remained trapped by coastal convergence, reaching the bottom and flowing poleward.

- mid February-June 2009: In the spring, continental runoff waters, accumulated during previous winter, were exported offshore through the surface during upwelling events. The prevailing upwelling periods were interleaved with short but strong downwelling events. At the same period, stratification of the surface layer increased, which resulted in warming of the bottom layer during downwelling, due to convergence of the warmer surface waters.

- August-September 2009: In the summer, the seasonal thermocline was established and coastal upwelling of cold subsurface waters contributed to the formation of a frontal region extending to the outer shelf

- October-December 2009: The transport of warm and saline waters into the shelf by the IPC offset the surface cooling, while the seasonal thermocline was gradually breaking. Concurrently, increasing river inflow and coastal convergence contributed to the generation of the WIBP.

Comparison of this year with existing knowledge of the seasonal variability highlighted the anomalous upwelling of autumn 2008 and the late upwelling season of 2009 (stronger upwelling in August-September instead of July-August). Additionally, convergence events of surface warm waters promoted the increase in temperature of the bottom layers, when the seasonal thermocline was developed, not only in the end of the upwelling season but also before the coastal upwelling front was established (June and July).

The modeling with two-way nesting provided a way to solve simultaneously the circulation from the large scales of the open ocean to the shelf scale. The main focus was done on the shelf circulation near cape Silleiro, but the present configuration solved the general patterns of Rías Baixas, and its influence on the shelf circulation. Although this study focused on one year period centered in 2009, this kind of realistic modeling approach could be reliably applied to other periods.

Chapter 5

Conclusions and Perspectives

An overview of the main results of this thesis is made here. Suggestions for future works are also given, including the possible applications of the developed tools and research perspectives.

The main objective of this thesis was to study particular processes of the hydrography and circulation on the WIM, with special emphasis in the northern region. With that in mind, *in-situ* data from the CAIBEX project provided a solid observational basis for the period between November 2008 and December 2009.

Before delving into the northern region, a numerical simulation of the full WIM was applied in a statistical study of filaments for the upwelling seasons of the years 2001-2010. The method for the filament detection was based on the visual representation of SST fields of the model and satellite imagery, with promising results. Like the similar study two decades before (*Haynes et al.*, 1993a), filaments were more abundant south of 40°N and anchored to the main coastal features, while on the smoother coast north of it, their locations were often variable. Although the association of filament locations with topographic irregularities is evident, the formation mechanism of filaments appearing in regions with smoother topography is still not fully understood. The influence of the eddy field on filaments location and direction is also still unknown and should be further investigated. Here, a visual comparison of eddy and filament fields provided evidence of the enhanced eddy-filament interactions during relaxation periods. Nevertheless, the monthly number of filaments was associated with the mean along shore winds from June to September, regardless of region. Filaments were more prevalent in July and August with low interannual variability in the southern region. In the northern region, filaments were more prevalent in July, August and September, although with high interannual variability (monthly number of filaments <20 in some years and >80 in others). The manual methodology for filament

detection is valuable when physical inconsistencies appear in the SST images, although the decision to mark filaments depends on the subjectivity of the user. The development of automatic algorithms to filament detection, such as the one proposed by *Nieto et al.* (2012), would reduce significantly the time spent when applied to large sets of data and contribute to more objective results depending on parameters defined by the user.

The CAIBEX project included the surveying of the upwelling filaments existing on the NWIM. This survey was scheduled for July 2009, but in this period, the upwelling was still not fully established, so the cruise focus became the study of the early stages of an upwelling season and the transient responses on shelf circulation to the wind. The cruise consisted on the sampling of the shelf and offshore through zonal transects of hydrographic and velocity data. Two regimes of circulation were identified in the transects: one associated with northerly winds and the other associated with downwelling and relaxation of upwelling. In both regimes the IPC was prevalent on the offshore region and an equatorward current was observed on the upper slope. The difference between regimes occurred on the shelf, where the circulation responded rapidly in the southward (northward) direction under northerly (southerly) winds. Upwelling of cold waters was more intense between Porto and cape Silleiro, while when northerly winds relaxed, warm waters flow through the inner-shelf from South. The mechanisms proposed by *Pringle* (2002) and *Pringle and Dever* (2009) for the existence of an upwelling center and counter flows in an equatorward widening shelf region of the Californian upwelling system, are possible explanations for the enhanced upwelling and the inner-shelf counter flows in the Porto-Silleiro region, as the bathymetry is similar.

The seasonal cycle of the NWI shelf hydrography and circulation was analyzed through observational data and the development of a realistic numerical model (NWIc). Between November 2008 and December 2009, distinct periods were identified in respect to the underlying processes. Comparing the November and December of 2008 and 2009 revealed distinct autumn conditions, one exceptionally ruled by upwelling in 2008 and other by downwelling in 2009, but both showed weak stratification on the inner-shelf. The seasonal thermocline gradually developed in spring 2009 and persisted from June 2009 until early November 2009. In this period, events of downwelling favorable winds promoted coastal convergence of the warmer surface waters, which extended down to the bottom layers and were associated with inner-shelf poleward currents. Fresh water plumes were originated with high river runoff, flowing poleward and accumulating in the coastal region, including Rías Baixas, under downwelling (most notably January-February 2009 and October-December 2009). Their expansion offshore occurred with the relaxation of these downwelling periods, and under upwelling, the equatorward jet deflected them in the southwestward direction

on the shelf. The freshwater plume could extend as far as the shelf edge, in the end of the winter season.

In order to locally study an upwelling system, with exchanges between complex estuarine systems and the shelf, such as in the NWIM, the use of a modeling configuration capable of resolving, for long periods of time, the multi-scale approximations is recommended. This way, the modeling systems can keep up with the increasing availability of observations, which still are limited to identify the physical processes of the ocean.

The linkage between the set of observations and modeling results proved to be valuable on the identification of the NWI shelf processes. The modeling configuration developed in this study helped to complement and successfully explain the main events characteristic of each season. As a result, the present configuration can be reliably applied to study this region shelf circulation to other periods, even when observational data is scarce.

The present configuration is not designed to solve the circulation inside the narrow estuaries, south of Rías Baixas (with dimensions of O(1) km). In this way, the salinity and temperature fields have to be imposed at the mouth of those estuaries. Otherwise, a configuration to solve the estuary coupled with the present configuration should be used. Although limited in this aspect, the present configuration was able to accurately reproduce the plumes on the shelf region, either by their behaviours in response to the local currents or by the salinity values at the surface.

Tidal forcing was not imposed on the developed configuration. Although it could have been easily introduced, previous experience shows that tidal dynamics have no strong impact to the subinertial current field on the shelf.

Two of the processes that are described in this thesis deserve a dedicated study. One is the existence of an upwelling center in the Porto-Silleiro region, and the other is the formation of counter-flows on the inner-shelf during periods of upwelling relaxation. Although this modeling configuration provided evidences of the occurrence of these processes, an idealized configuration, isolating parameters such as the bathymetry or wind forcing, would be able to identify the relative importance of those processes.

The developed modeling configuration contributes to multidisciplinary studies that depend on the physical aspects of the ocean. The implementation of biogeochemical modules and sediment modules is possible within this modeling system. Also, the modeling results could be applied in lagrangian modules to simulate particle transport in diverse areas of study, such as marine biology (larvae transport) and environmental issues (microplastics and oil patches). The applications above could also be used in the framework of regional studies of climate change. Another kind of application would be the use of numerical modeling to the forecasting of HAB events, which is a threat to the production of bivalves in

the region. This is a particular problem in the Rías Baixas, where the local economy depends highly on bivalve production. Finally, it is possible to run this model configuration in operational mode, providing online results for hydrography and velocity fields, as a tool to develop different applications to forecast the above mentioned issues.

Appendix A

Summer 2009

In Chapter 2, the filament field was only shown for the year 2002 but the analysis was made for all years from 2001 to 2010. Since Chapters 3 and 4 refer to the year 2009, it is worthwhile to have an idea of the filament field of that year. In general, the presence of filaments on the NWIM can be associated with the period of stronger northerly winds in August and September. The absence of filaments near cape Silleiro in July 2009 suggests a locally unformed upwelling front (Chapter 3). Care should be taken that the model used in the filament detection (WIc) was distinct from the one in Chapter 4 (NWIc).

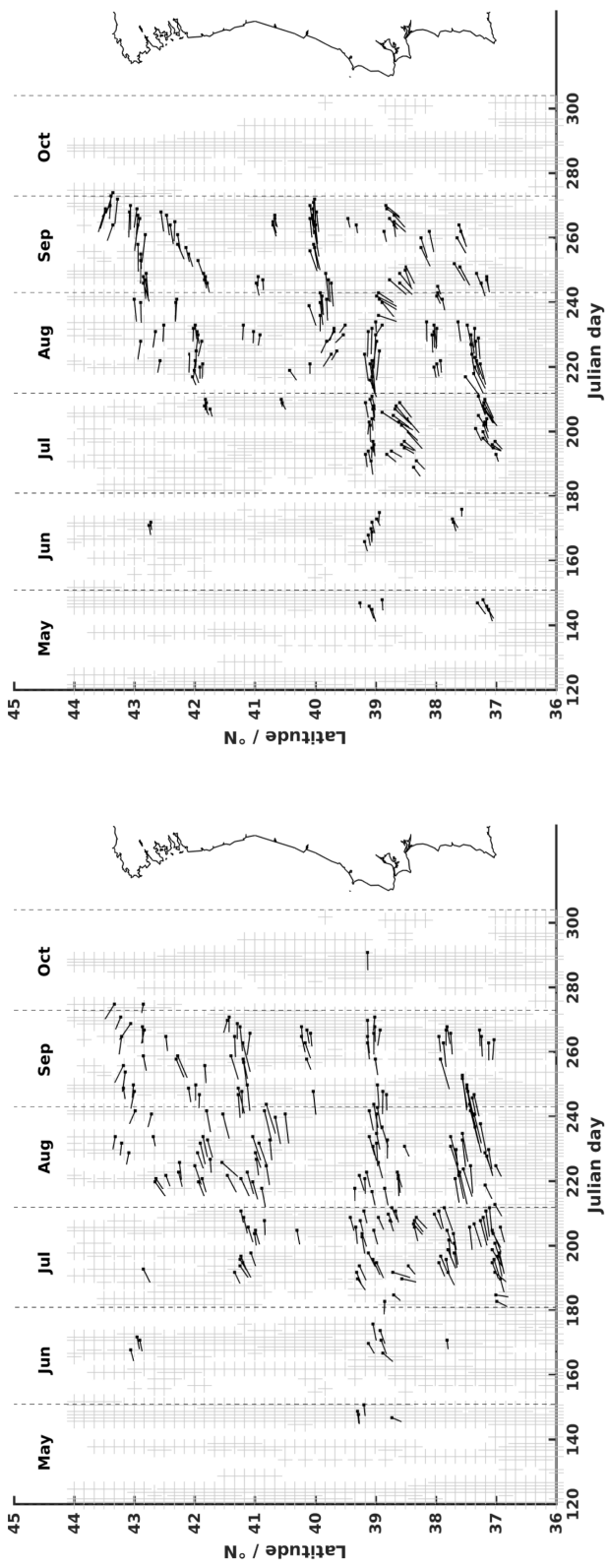

Figure A.1: May to October 2009 time series of Filament length and direction (black lines) and latitude of their coastal origin (black dots), observed on zonal stripes with cloud coverage lower than 50% (gray plus signals), from (left) Satellite and (right) Model products.

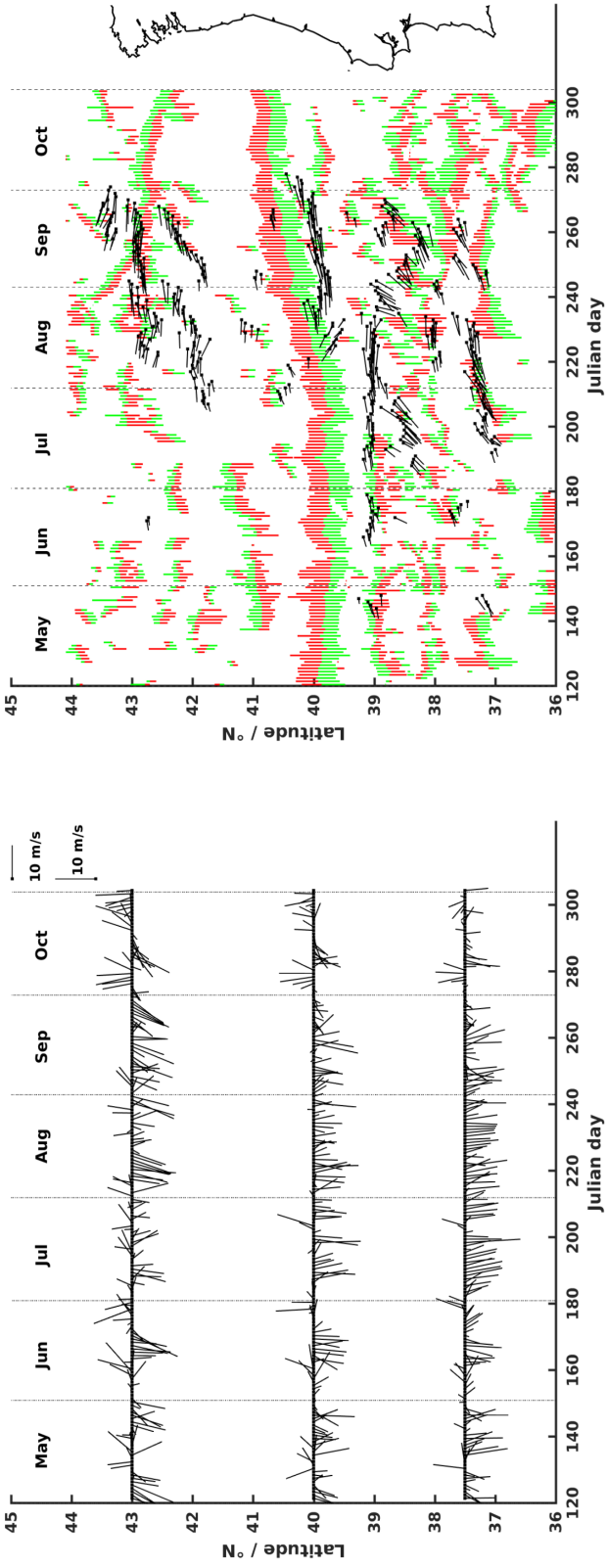

Figure A.2: Time series from May to October 2009 of: (left) QuikSCAT wind speed and direction registered in three distinct latitudes at 9.5°W; (right) Filament length and direction (black lines) and latitude of their origin (black dots) on the coast. Green (offshore current) and red (onshore current) colored lines show locations of eddies registered east of 11°W.

Appendix B

CAIBEX Transects

The transects with CTD (top) and minibat (bottom) measurements of temperature and salinity are shown in this appendix for all the cruises performed with the RV Mytilus. The along-shore (across-shore) component of currents obtained with vmADCP are superimposed in the transects of temperature (salinity) as dark contours in m/s, with positive values as continuous lines and negative as dashed. On the temperature transects, isopycnal of 26 g/m^3 is represented in white and 27 g/m^3 is gray. On the salinity transects, isolines of spiciness are represented in white (2.2) and gray (2.5).

The WRF wind at 10 m high in front of cape Silleiro (42.1°N) and the river Minho flow are represented for the 5 days before and after each cruise. Blue arrows represent the wind located offshore (9.4°W) and red arrows represent the wind located near shore (8.91°W).

The map of the CTD measurements location (top right) shows the 3-day composite SST from the satellite imagery including the day of the cruise, the previous and following days.

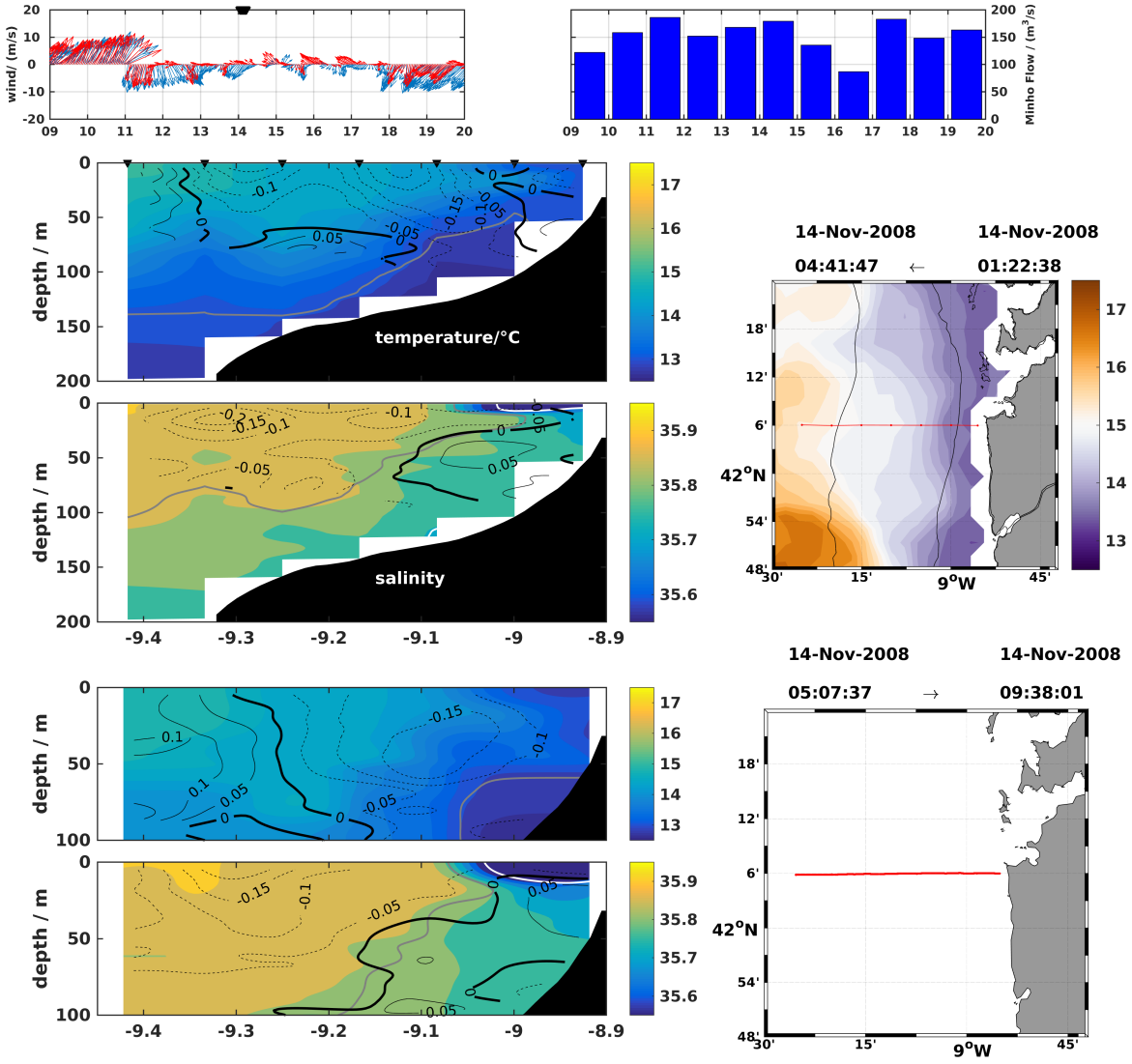

Figure B.1: Transect of 14 November 2008

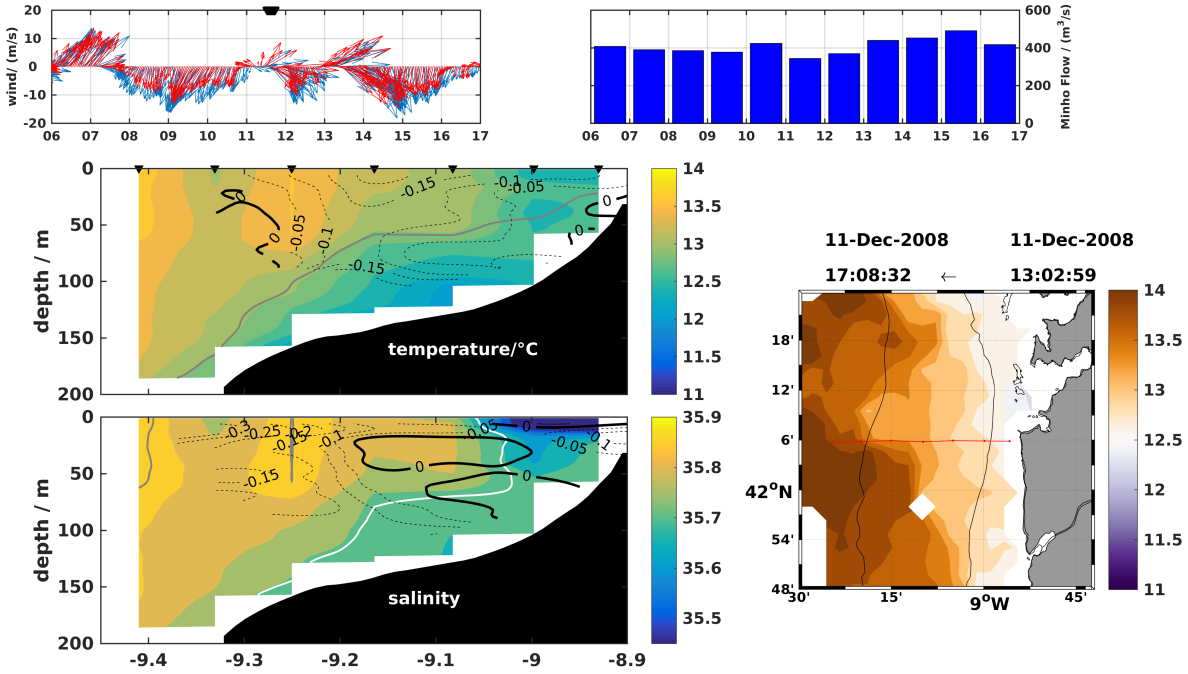

Figure B.2: Transect of 10 December 2008

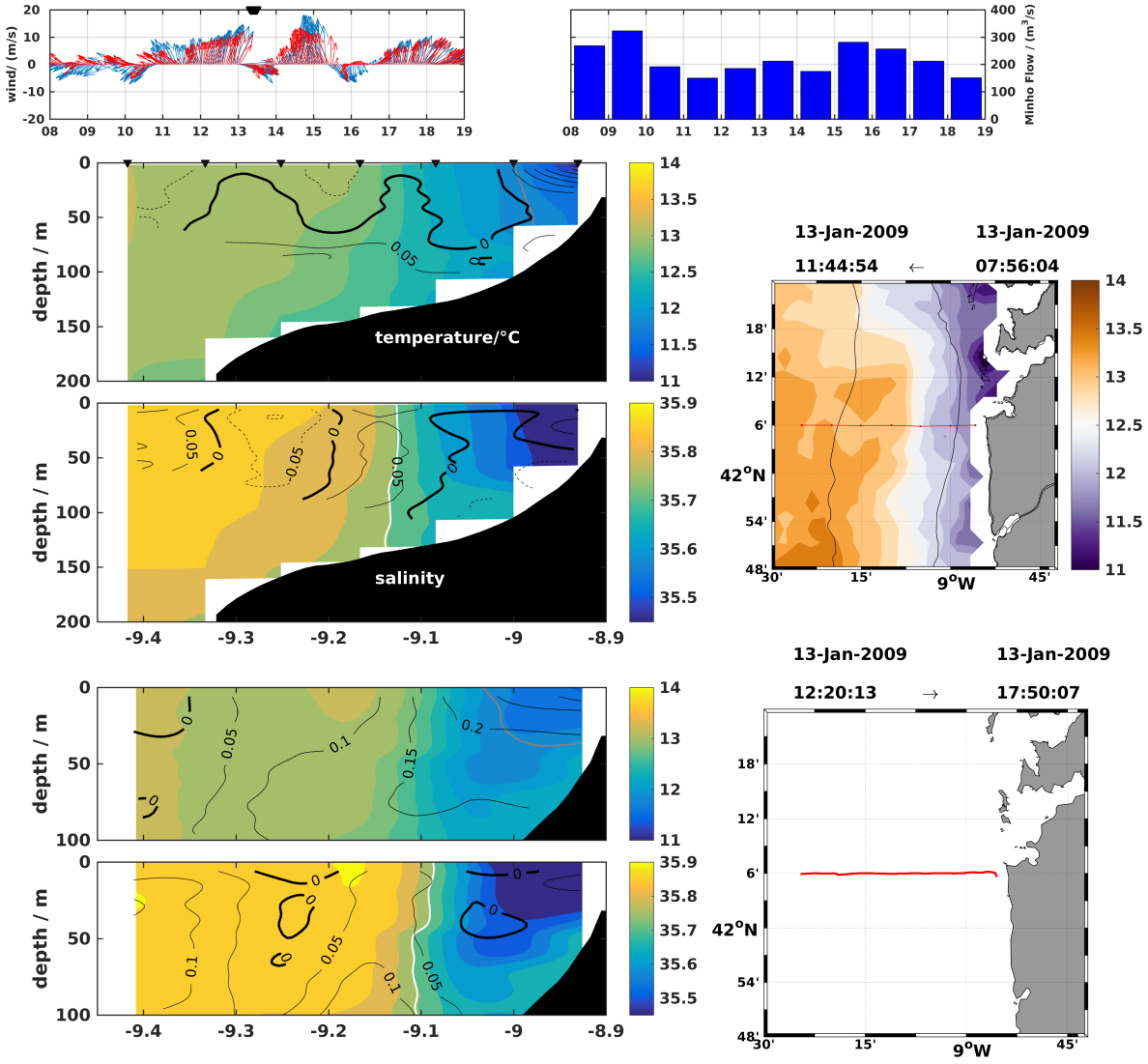

Figure B.3: Transect of 13 January 2009

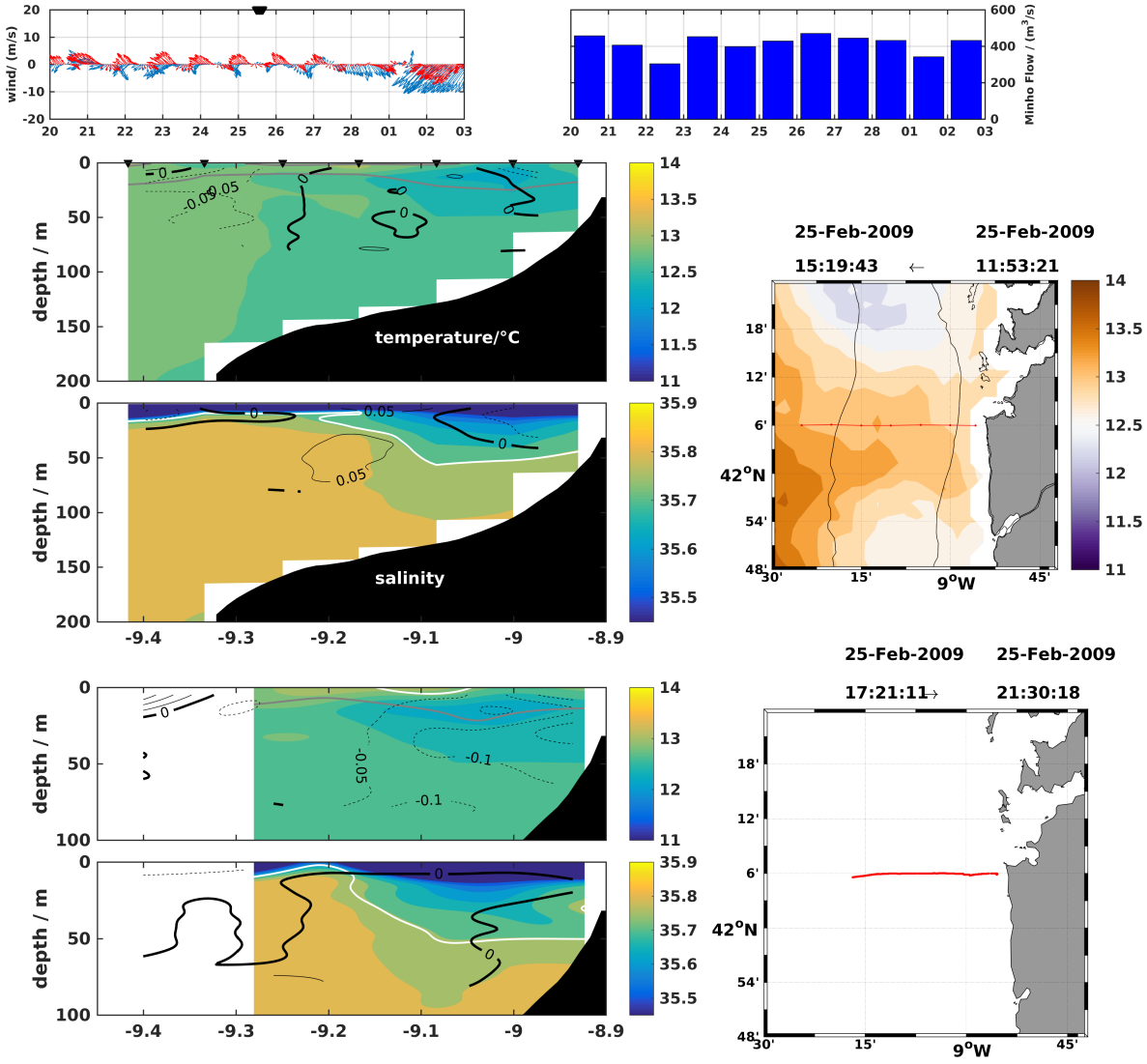

Figure B.4: Transect of 25 February 2009

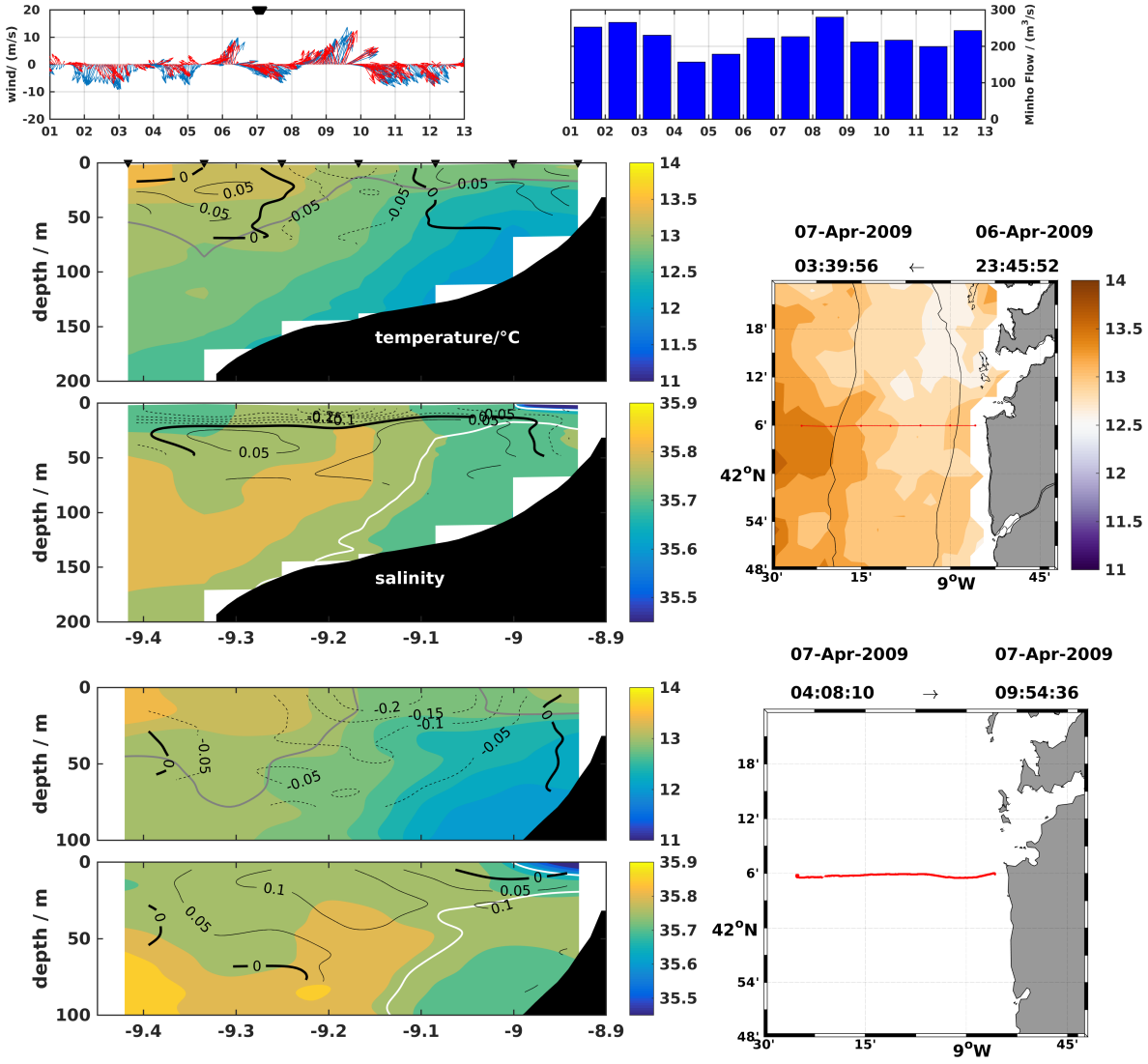

Figure B.5: Transect of 6-7 April 2009

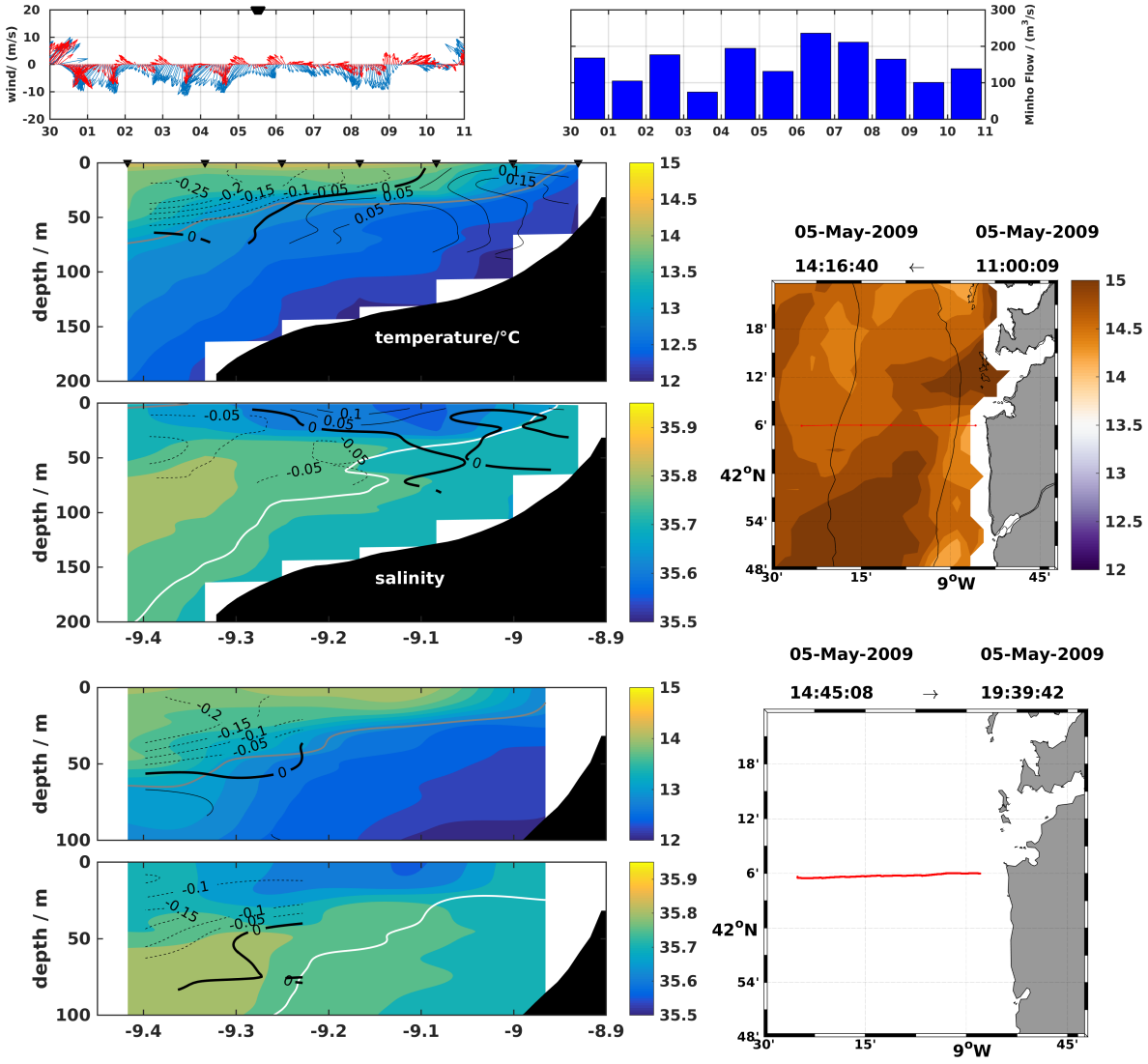

Figure B.6: Transect of 5 May 2009

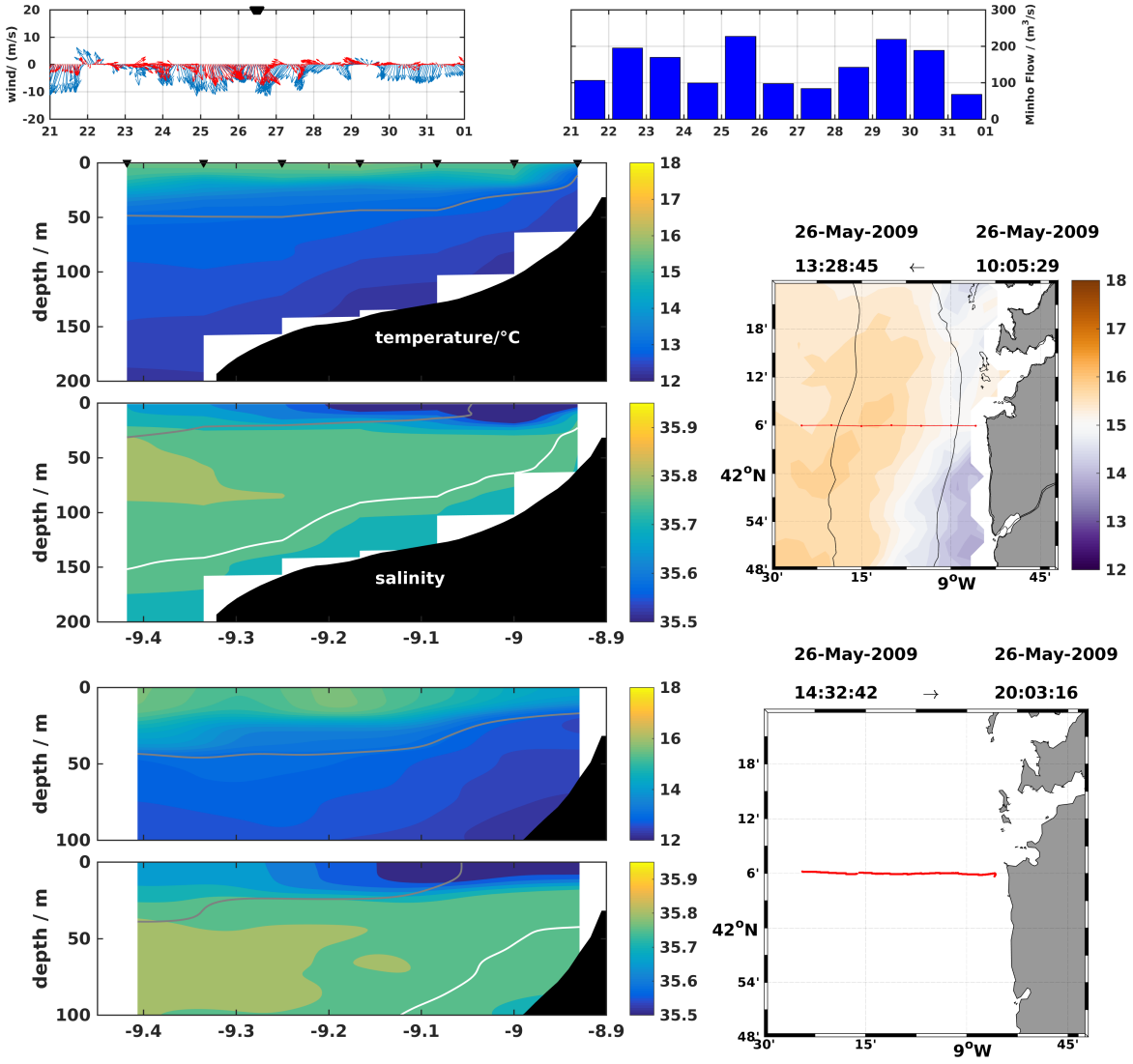

Figure B.7: Transect of 26 May 2009

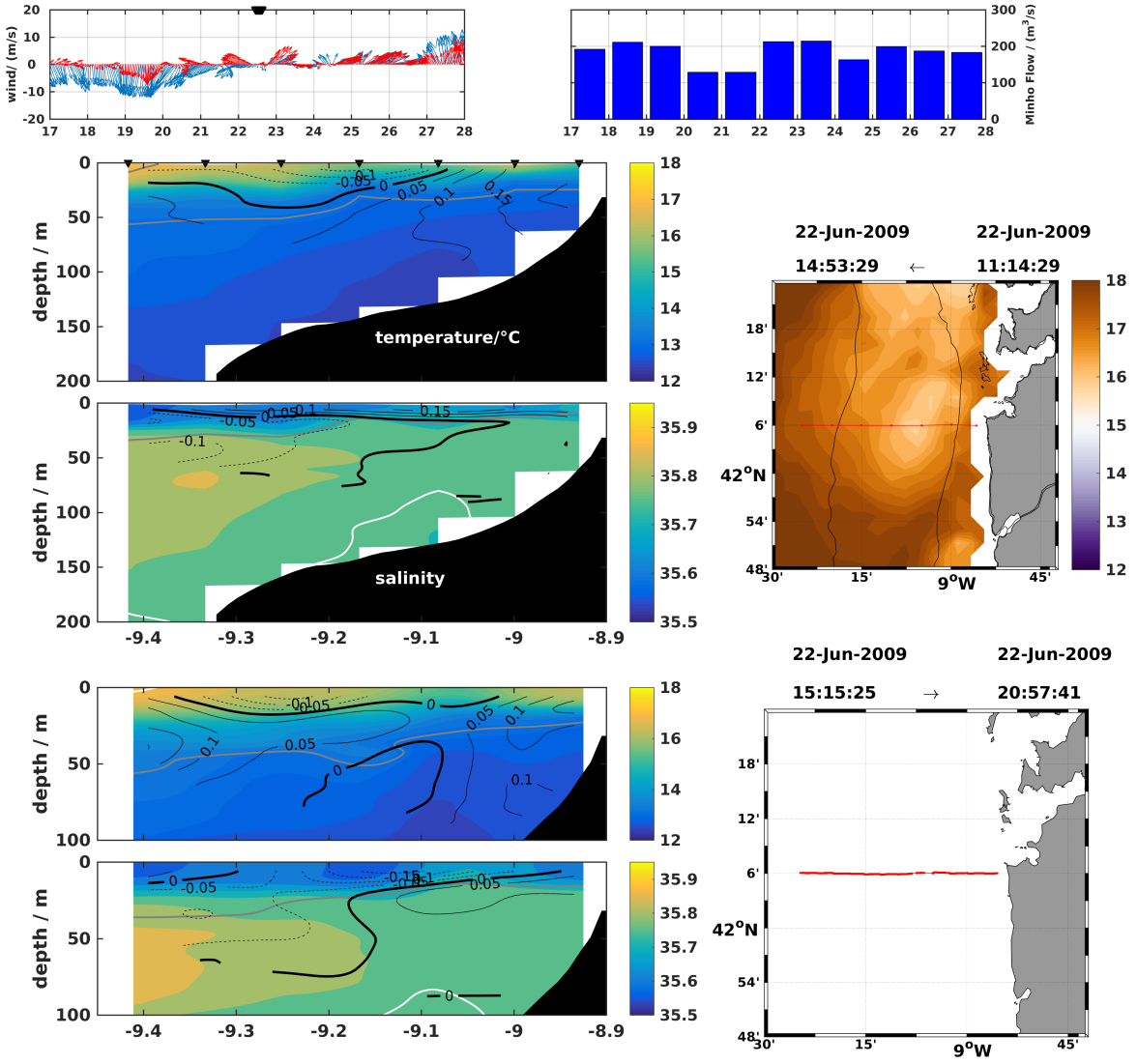

Figure B.8: Transect of 22 June 2009

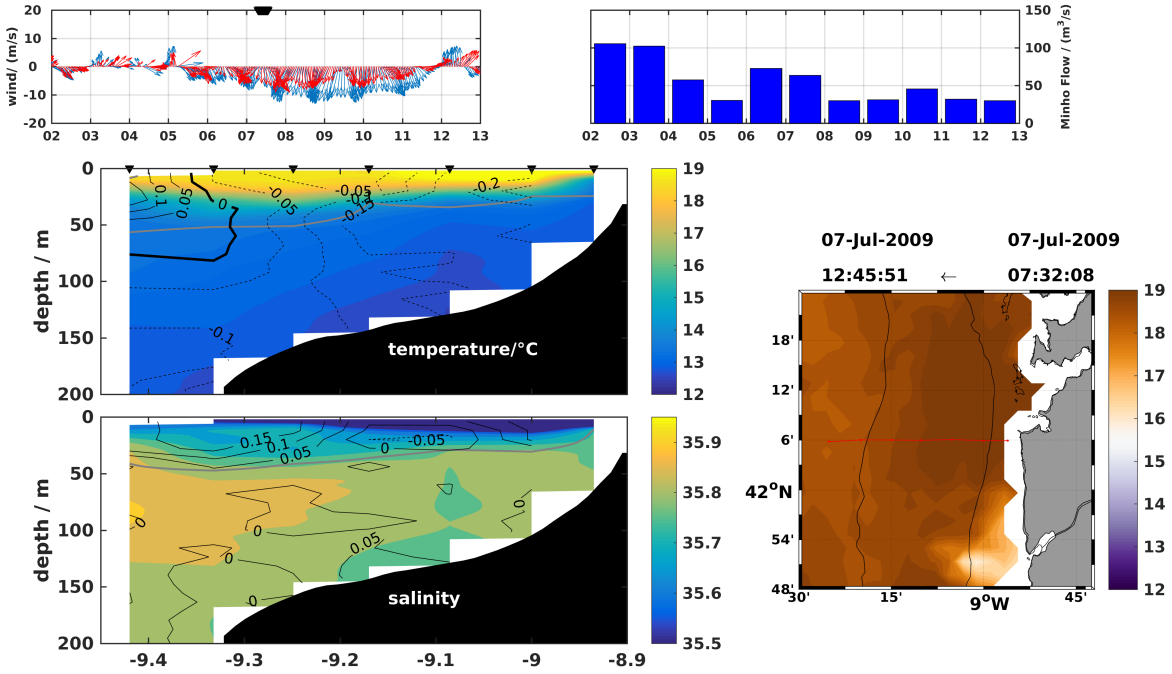

Figure B.9: Transect of 7 July 2009

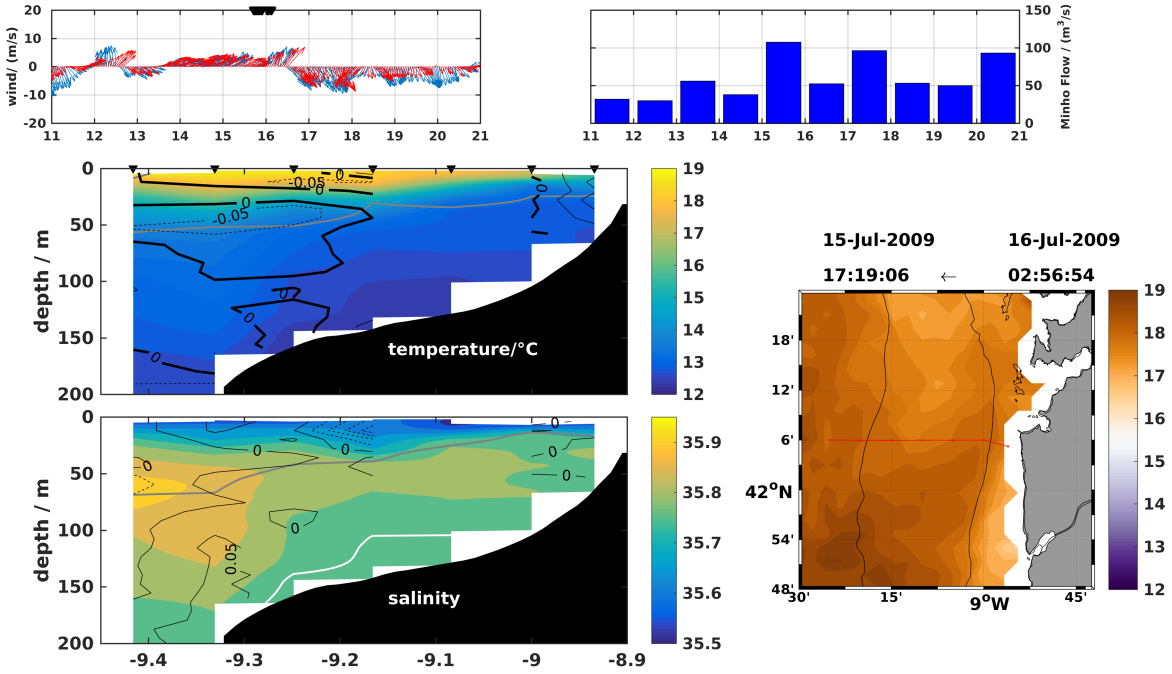

Figure B.10: Transect of 15-16 July 2009

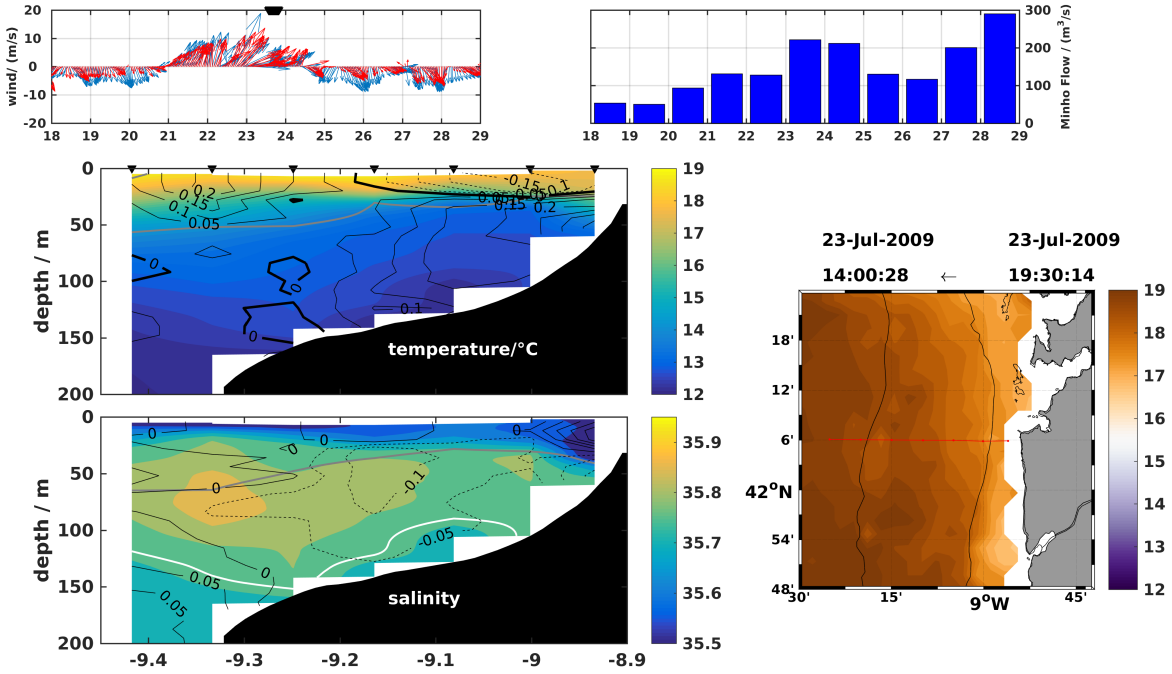

Figure B.11: Transect of 23 July 2009

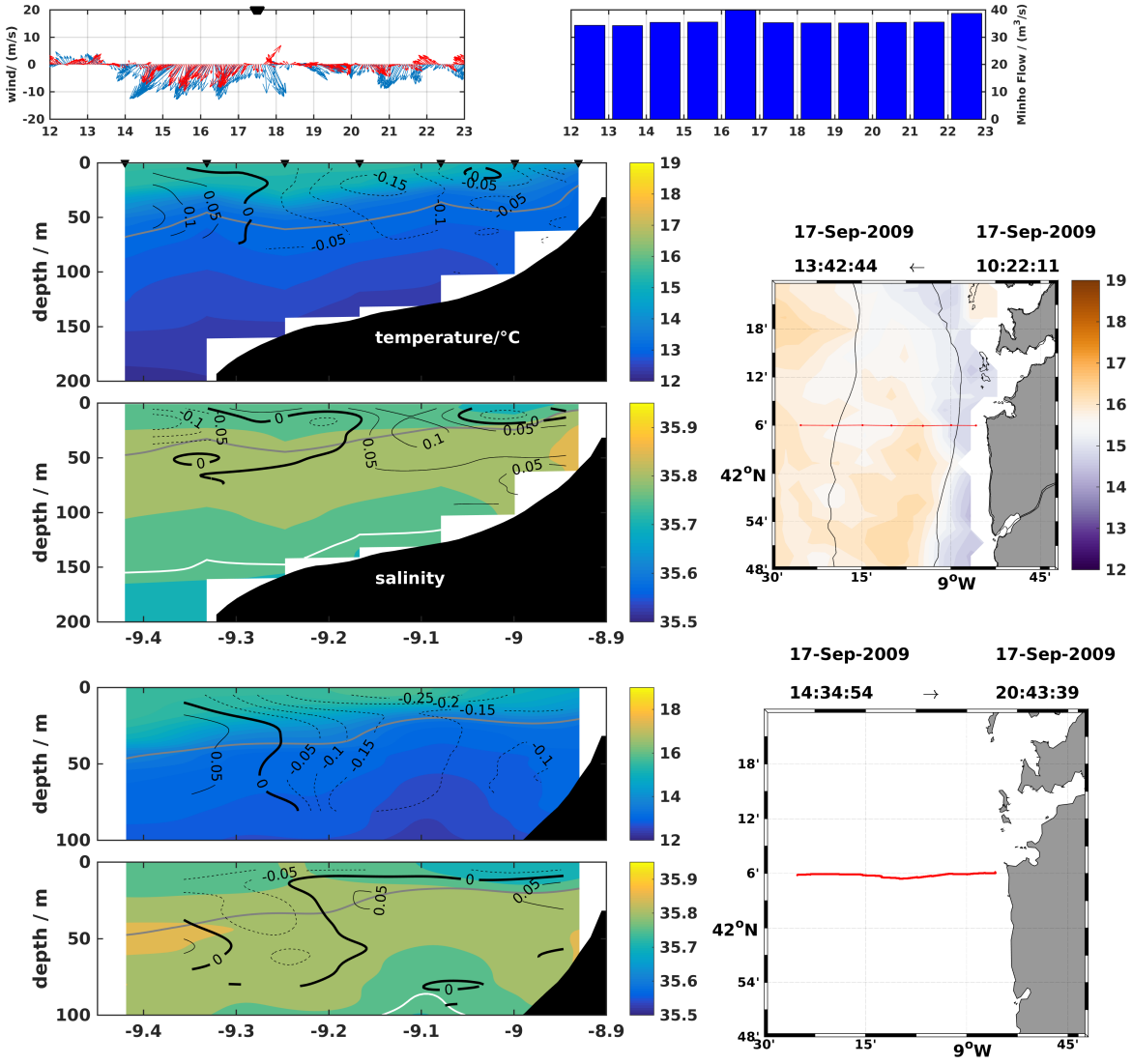

Figure B.12: Transect of 17 September 2009

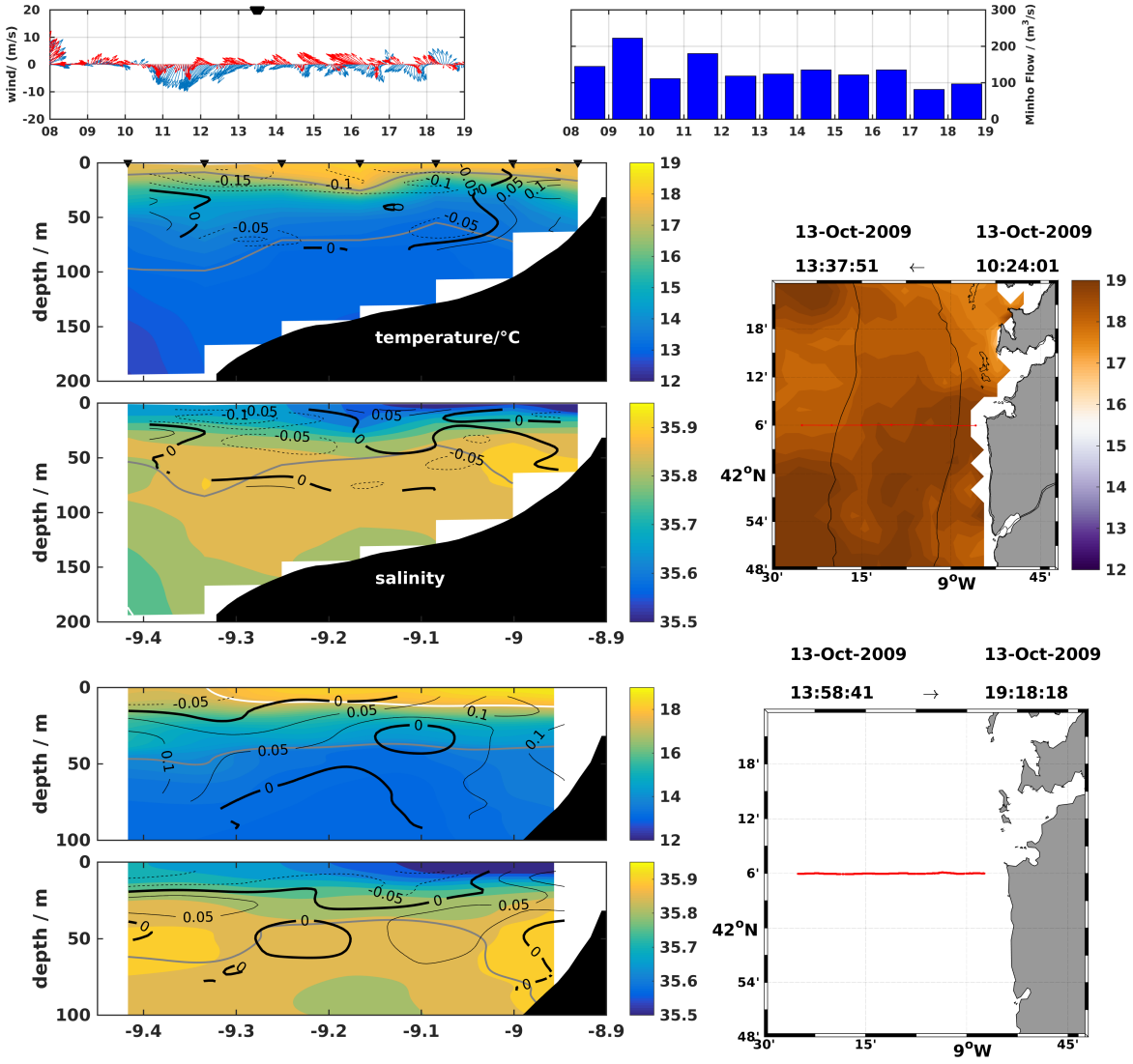

Figure B.13: Transect of 13 October 2009

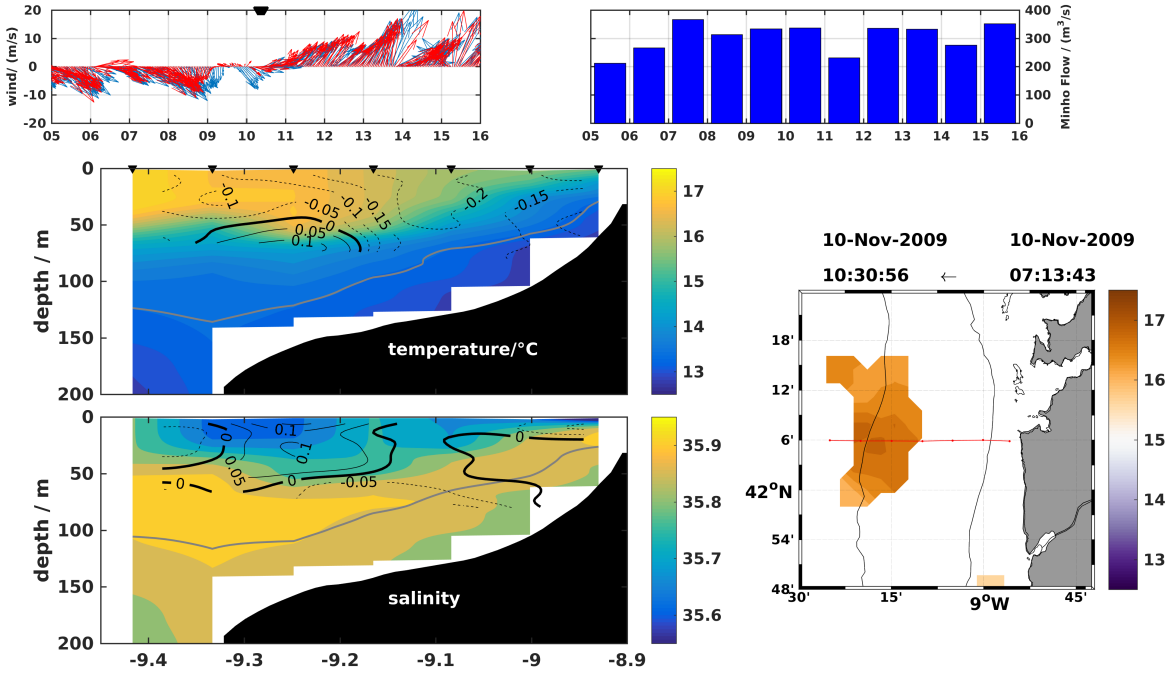

Figure B.14: Transect of 10 November 2009

Bibliography

A.G. Kostianoy, and A.G. Zatsepin (1996), The West African coastal upwelling filaments and cross-frontal water exchange conditioned by them, *Journal of Marine Systems*, *7*(2-4), 349–359, doi:10.1016/0924-7963(95)00029-1.

Álvarez-Salgado, X., C. G. Castro, F. F. Pérez, and F. Fraga (1997), Nutrient mineralization patterns in shelf waters of the Western Iberian upwelling, *Continental Shelf Research*, *17*(10), 1247–1270, doi:10.1016/S0278-4343(97)00014-9.

Álvarez-Salgado, X. A., G. Roson, F. F. Perez, and Y. Pazos (1993), Hydrographic Variability Off the Rias Baixas (NW Spain) during the Upwelling Season, *Journal of Geophysical Research-Oceans*, *98*(C8), 14,447–14,455.

Álvarez-Salgado, X. A., J. Gago, B. M. Míguez, M. Gilcoto, and F. F. Pérez (2000), Surface Waters of the NW Iberian Margin: Upwelling on the Shelf versus Outwelling of Upwelled Waters from the Rías Baixas, *Estuarine, Coastal and Shelf Science*, *51*(6), 821–837, doi:10.1006/ecss.2000.0714.

Álvarez-Salgado, X. A., S. Beloso, I. Joint, E. Nogueira, L. Chou, F. F. Perez, S. Groom, J. M. Cabanas, A. P. Rees, and M. Elskens (2002), New production of the NW Iberian shelf during the upwelling season over the period 1982-1999, *Deep-Sea Research Part I-Oceanographic Research Papers*, *49*(10), 1725–1739.

Álvarez-Salgado, X. A., F. G. Figueiras, F. F. Pérez, S. Groom, E. Nogueira, A. V. Borges, L. Chou, C. G. Castro, G. Moncoiffé, A. F. Ríos, A. E. J. Miller, M. Frankignoulle, G. Savidge, and R. Wollast (2003), The Portugal coastal counter current off NW Spain: new insights on its biogeochemical variability, *Progress in Oceanography*, *56*(2), 281–321, doi:10.1016/S0079-6611(03)00007-7.

Amante, C., and B. W. Eakins (2009), ETOPO1 1 Arc-Minute Global Relief Model: Procedures, Data Sources and Analysis., NOAA technical memorandum NESDIS NGDC-24.

Ambar, I., and A. F. G. Fiuza (1994), Some features of the Portugal current system: a poleward slope undercurrent, an upwelling-related summer southward flow and autumn-winter poleward coastal surface current, in *Proceeding of the 2nd International Conference on Air-Sea Interaction, Meteorology and Oceanography of the Coastal Zone*, edited by American Meteorological Society, p. 311.

Antonov, J. I., D. Seidov, T. P. Boyer, R. A. Baranova, A. V. Mishonov, H. E. Garcia, O. K. Baranova, M. M. Zweng, and D. R. Johnson (2010), World Ocean Atlas 2009, Volume 2: Salinity, *Tech. rep.*, S. Levitus, Ed. NOAA Atlas NESDIS 69, U.S. Government Printing Office, Washington, D.C., 184 pp.

Austin, J. a., and S. J. Lentz (2002), The Inner Shelf Response to Wind-Driven Upwelling and Downwelling, *Journal of Physical Oceanography*, *32*(7), 2171–2193, doi:10.1175/1520-0485(2002)032<2171:TISRTW>2.0.CO;2.

Aznar, R., M. G. Sotillo, S. Cailleau, P. Lorente, B. Levier, A. Amo-Baladrón, G. Reffray, and E. Álvarez-Fanjul (2016), Strengths and weaknesses of the CMEMS forecasted and reanalyzed solutions for the Iberia-Biscay-Ireland (IBI) waters, *Journal of Marine Systems*, *159*, 1–14, doi:10.1016/j.jmarsys.2016.02.007.

Barnes, S. L. (1994), Applications of the Barnes Objective Analysis Scheme. Part I: Effects of Undersampling, Wave Position, and Station Randomness, doi:10.1175/1520-0426(1994)011<1433:AOTBOA>2.0.CO;2.

Barth, J. A. (1994), Short-wavelength instabilities on coastal jets and fronts, *Journal of Geophysical Research*, *99*(C8), 16,095–16,115.

Barton, E. D., M. E. Inall, T. J. Sherwin, and R. Torres (2001), Vertical structure, turbulent mixing and fluxes during Lagrangian observations of an upwelling filament system off Northwest Iberia, *Progress in Oceanography*, *51*(2-4), 249–267, doi:10.1016/S0079-6611(01)00069-6.

Barton, E. D., J. L. Largier, R. Torres, M. Sheridan, A. Trasviña, A. Souza, Y. Pazos, and A. Valle-Levinson (2015), Coastal upwelling and downwelling forcing of circulation in a semi-enclosed bay: Ria de Vigo, *Progress in Oceanography*, *134*, 173–189, doi:10.1016/j.pocean.2015.01.014.

Barton, E. D., R. Torres, F. G. Figueiras, M. Gilcoto, and J. Largier (2016), Surface water subduction during a downwelling event in a semienclosed bay, *Journal of Geophysical Research : Oceans*, *121*, 7088–7107, doi:10.1002/2016JC0119050.

Bentamy, A., and D. C. Fillon (2012), Gridded surface wind fields from Metop/ASCAT measurements, *International Journal of Remote Sensing*, *33*(6), 1729–1754, doi:10.1080/01431161.2011.600348.

Bernstein, R. L., L. Breaker, and R. Whirtner (1977), California Current eddy formation: ship, air and satellite results, *Science*, *195*, 353–359.

Breaker, L. C., and R. P. Gilliland (1981), A Satellite Sequence on Upwelling Along the California Coast, in *Coastal Upwelling*, edited by F. A. Richards, pp. 87–94, American Geophysical Union, doi:10.1029/CO001p0087.

Carvalho, D., A. Rocha, and M. Gómez-Gesteira (2012), Ocean surface wind simulation forced by different reanalyses: Comparison with observed data along the Iberian Peninsula coast, *Ocean Modelling*, *56*, 31–42, doi:10.1016/j.ocemod.2012.08.002.

Castro, C. G. (1996), Caracterización Química del Agua Subsuperficial del Atlántico Nororiental Y su Modificación por Procesos Biogeoquímicos, PhD Thesis, Universidade de Santiago de Compostela, p. 242.

Castro, C. G., X. A. Alvarez-Salgado, F. G. Figueiras, F. F. Perez, and F. Fraga (1997), Transient hydrographic and chemical conditions affecting microplankton populations in the coastal transition zone of the {Iberian} upwelling system {(NW Spain)} in {September} 1986, *Journal of Marine Research*, *55*(2), 321–352.

Chao, S.-Y., and W. C. Boicourt (1986), Onset of Estuarine Plumes, doi:10.1175/1520-0485(1986)016<2137:OOEP>2.0.CO;2.

Coelho, H. S. (2001), Modelação de processos físicos relacionados com a circulação oceânica na Margem Continental Ibérica, PhD Thesis, Instituto Superior Técnico, Lisboa, p. 272.

Cordeiro, N. G., R. Nolasco, A. Cordeiro-Pires, E. D. Barton, and J. Dubert (2015), Filaments on the Western Iberian Margin : A modeling study, *Journal of Geophysical Research: Oceans*, *120*, 1–17, doi:10.1002/2014JC010688.

Cordeiro, N. G. F., J. Dubert, R. Nolasco, and E. D. Barton (2018), Transient response of the Northwestern Iberian upwelling regime, *PLoS ONE*, pp. 1–19, doi:10.1371/journal.pone.0197627.

Cordeiro-Pires, A. (2013), Modelação da circulação na Margem Ibérica Ocidental: presente e futuro, Ph.D. thesis, Universidade de Aveiro.

Cravo, A., P. Relvas, S. Cardeira, F. Rita, M. Madureira, and R. Sánchez (2010), An upwelling filament off southwest Iberia: Effect on the chlorophyll a and nutrient export, *Continental Shelf Research*, *30*(15), 1601–1613.

Curros, S., M. C. Martín, L. Ferrer, B. Companys, D. Carcajona, S. Santamaría, E. Spyrakos, J. Torres, and G. Rosón (2009), Winter Patterns of Hydrography and Dynamics Off Western Galicia (NW Spain), *Thalassas*, *25*(2), 47–56.

da Silva, A., C. C. Young, and S. Levitus (1994), Atlas of Surface Marine Data 1994, Vol. 1 AAlgorithm and Procedures, NOAA Atlas NESDIS 6. U.S. Gov. Printing Office, Washington, D.C., 83pp.

Debreu, L., P. Marchesiello, P. Penven, and G. Cambon (2012), Two-way nesting in split-explicit ocean models: Algorithms, implementation and validation, *Ocean Modelling*, *49-50*, 1–21, doi:10.1016/j.ocemod.2012.03.003.

Dubert, J. (1998), Dynamique du Système de Courants vers le Pole au Voisinage de la Pente Continentale a l'Ouest et au Nord de la Péninsule Ibérique, PhD Thesis, Université de Bretagne Occidentale, p. 237.

Fiedler, P. C., and R. M. Laurs (1990), Variability of the Columbia River plume observed in visible and infrared satellite imagery, *International Journal of Remote Sensing*, *11*(6), 999–1010, doi:10.1080/01431169008955072.

Firing, E., J. Ranada, and P. Caldwell (1995), Processing ADCP Data With the Codas Software System, Version 3.1, *Tech. rep.*, Joint Institute for Marine and Atmospheric Research, University of Hawaii & National Oceanographic Data Center, University of Hawaii.

Fischer, J., and M. Visbeck (1993), Deep Velocity Profiling with Self-contained ADCPs, doi:10.1175/1520-0426(1993)010<0764:DVPWSC>2.0.CO;2.

Fiuza, A. F. G. (1984), Hidrologia e dinâmica das águas costeiras de Portugal, Ph.D. thesis, Universidade de Lisboa, Portugal, p. 294.

Fiúza, A. F. G., M. E. Macedo, and M. R. Guerreiro (1982), Climatological space and time variation of the Portuguese coastal upwelling, *Oceanologica Acta*, *5*(1), 31–40.

Fiúza, A. F. G., M. Hamann, I. Ambar, G. D. del Rio, N. Gonzalez, and J. M. Cabanas (1998), Water masses and their circulation off western Iberia during May 1993, *Deep-Sea Research Part I-Oceanographic Research Papers*, *45*(7), 1127–1160.

Flament, P., L. Armi, L. Washburn, L. Armi, and L. Washburn (1985), The Evolving Structure of an Upwelling Filament, *Journal of Geophysical Research*, *90*(C6), 11,765–11,778.

Frouin, R., A. F. G. Fiúza, I. Ambar, and T. J. Boyd (1990), Observations of a poleward surface current off the coasts of Portugal and Spain during winter, *Journal of Geophysical Research*, *95*(C1), 679, doi:10.1029/JC095iC01p00679.

Gago, J., J. M. Cabanas, G. Casas, and a. Miranda (2011), Thermohaline measurements in the continental shelf zone of the NW Iberian Peninsula, 1994-2006, *Climate Research*, *48*(2-3), 219–229, doi:10.3354/cr00943.

Gan, J., and J. S. Allen (2002), A modeling study of shelf circulation off northern California in the region of the Coastal Ocean Dynamics Experiment : Response to relaxation of upwelling winds, *Journal of Geophysical Research*, *107*(July 1982), 1–31, doi:10.1029/2000JC000768.

Gan, J., A. Cheung, X. Guo, and L. Li (2009), Intensified upwelling over a widened shelf in the northeastern South China Sea, *Journal of Geophysical Research: Oceans*, *114*(9), 1–15, doi:10.1029/2007JC004660.

García-García, L. M., M. Ruiz-Villarreal, and M. Bernal (2016), A biophysical model for simulating early life stages of sardine in the Iberian Atlantic stock, *Fisheries Research*, *173*, 250–272, doi:10.1016/j.fishres.2015.10.002.

Garcia-Soto, C. (2002), Navidad development in the southern Bay of Biscay: Climate change and swoddy structure from remote sensing and in situ measurements, *Journal of Geophysical Research*, *107*(C8), 1–29, doi:10.1029/2001JC001012.

Garel, E., I. Laiz, T. Drago, and P. Relvas (2016), Characterisation of coastal counter-currents on the inner shelf of the Gulf of Cadiz, *Journal of Marine Systems*, *155*, 19–34, doi:10.1016/j.jmarsys.2015.11.001.

Graham, W. M., J. G. Field, and D. C. Potts (1992), Persistent "upwelling shadows" and their influence on zooplankton distributions, *Marine Biology*, *114*(4), 561–570, doi:10.1007/BF00357253.

Haidvogel, D., and A. Beckmann (1999), *Numerical ocean circulation modeling*, *Series on Environmental Science and Management*, vol. 2, Imperial College Press, London.

Haynes, R. (1993), Eulerian and Lagrangian observations in the Iberian coastal transition zone, PhD Thesis, Univ. of Wales, Bangor, U.K., p. 123.

Haynes, R., and E. D. Barton (1990), A Poleward Flow Along the Atlantic Coast of the Iberian Peninsula, *Journal of Geophysical Research-Oceans*, *95*(C7), 11,425–11,441.

Haynes, R., E. D. Barton, and I. Pilling (1993a), Development, persistence, and variability of upwelling filaments off the Atlantic coast of the Iberian Peninsula, *Journal of Geophysical Research: Oceans*, *98*(C12), 22,681–22,692, doi:10.1029/93JC02016.

Haynes, R., E. D. Barton, and I. Pilling (1993b), Development, persistence, and variability of upwelling filaments off the Atlantic coast of the Iberian Peninsula, *Journal of Geophysical Research*, *98*(C12), 22,681, doi:10.1029/93JC02016.

Herrera, J. L. (2008), Variabilidad de corta escala temporal de las condiciones hidrográficas y dinámicas en la plataforma continental gallega, PhD Thesis, Faculdad de Ciencias Universidad de Vigo, p. 304.

Herrera, J. L., G. Rosón, R. a. Varela, and S. Piedracoba (2008), Variability of the western Galician upwelling system (NW Spain) during an intensively sampled annual cycle. An EOF analysis approach, *Journal of Marine Systems*, *72*, 200–217, doi:10.1016/j.jmarsys.2007.07.007.

Horner-Devine, A. R., R. D. Hetland, and D. G. MacDonald (2015), Mixing and Transport in Coastal River Plumes, *Annual Review of Fluid Mechanics*, *47*(1), 569–594, doi:10.1146/annurev-fluid-010313-141408.

Huthnance, J. M., H. M. Van Aken, M. White, E. D. Barton, B. Le Cann, E. F. Coelho, E. Alvarez Fanjul, P. Miller, and J. Vitorino (2002), Ocean margin exchange–water flux estimates, *Journal of Marine Systems*, *32*(1-3), 107–137.

Ikeda, M., and W. J. Emery (1984), Satellite Observations and Modeling of Meanders in the California Current System off Oregon and Northern California, *Journal of Physical Oceanography*, *14*, 1434–1450.

Kaihatu, J. M., R. a. Handler, G. O. Marmorino, and L. K. Shay (1998), Empirical orthogonal function analysis of ocean surface currents using complex and real-vector methods, *Journal of Atmospheric and Oceanic Technology*, *15*(4), 927–941, doi:10.1175/1520-0426(1998)015<0927:EOFAOO>2.0.CO;2.

Kersalé, M., L. Marié, B. Le Cann, A. Serpette, C. Lathuilière, A. Le Boyer, A. Rubio, and P. Lazure (2016), Poleward along-shore current pulses on the inner shelf of the Bay of Biscay, *Estuarine, Coastal and Shelf Science*, *179*(September), 155–171, doi: 10.1016/j.ecss.2015.11.018.

Kuebel Cervantes, B. T., and J. S. Allen (2006), Numerical model simulations of continental shelf flows off northern California, *Deep-Sea Research Part II: Topical Studies in Oceanography*, *53*(25-26), 2956–2984, doi:10.1016/j.dsr2.2006.07.004.

Large, W. G., J. C. Mcwilliams, and S. C. Doney (1994), Oceanic Vertical Mixing - a Review and a Model with a Nonlocal Boundary-Layer Parameterization, *Reviews of Geophysics*, *32*, 363–403, doi:10.1029/94rg01872.

Lentz, S. J., and J. Largier (2006), The Influence of Wind Forcing on the Chesapeake Bay Buoyant Coastal Current, *Journal of Physical Oceanography*, *36*(7), 1305–1316, doi:10.1175/JPO2909.1.

Levier, B., M. Benkiran, G. Reffray, and M. Sotillo (2014), IBIRYS: a Regional High Resolution Reanalysis (physical and biogeochemical) over the European North East Shelf., in *EGU*.

Locarnini, R. A., A. V. Mishonov, J. I. Antonov, T. P. Boyer, H. E. Garcia, O. K. Baranova, M. M. Zweng, and D. R. Johnson (2010), World Ocean Atlas 2009, Volume 1: Temperature, *Tech. rep.*, S. Levitus, Ed., NOAA Atlas NESDIS 68, U.S. Government Printing Office, Washington, D.C, 184 pp.

Lorenzo, M. N., and J. J. Taboada (2005), Influences of atmospheric variability on freshwater input in Galician Rias in winter, *Journal of Atmospheric & Ocean Science*, *10*(4), 377–387.

M-F/CMS (2009), North Atlantic Regional Sea Surface Temperature Product manual.

Marchesiello, P., J. C. McWilliams, and A. Shchepetkin (2001), Open boundary conditions for long-term integration of regional oceanic models, *Ocean Modelling*, *3*(1), 1–20, doi: 10.1016/S1463-5003(00)00013-5.

Marchesiello, P., J. C. McWilliams, and A. Shchepetkin (2003), Equilibrium Structure and Dynamics of the California Current System, *Journal of Physical Oceanography*, *33*(4), 753–783.

Marchesiello, P., L. Debreu, and X. Couvelard (2009), Spurious diapycnal mixing in terrain-following coordinate models: The problem and a solution, *Ocean Modelling*, *26*(3-4), 156–169, doi:10.1016/j.ocemod.2008.09.004.

Marta-Almeida, M., and J. Dubert (2006), The structure of tides in the Western Iberian region, *Continental Shelf Research*, *26*(3), 385–400, doi:10.1016/j.csr.2005.11.011.

Marta-Almeida, M., R. Reboreda, C. Rocha, J. Dubert, R. Nolasco, N. Cordeiro, T. Luna, A. Rocha, J. D. e Silva, H. Queiroga, A. Peliz, M. Ruiz-Villarreal, J. D. Lencart e Silva, H. Queiroga, A. Peliz, and M. Ruiz-Villarreal (2012), Towards Operational Modeling and Forecasting of the Iberian Shelves Ecosystem, *PLoS ONE*, *7*(5), e37,343, doi:10.1371/journal.pone.0037343.

Marta-Almeida, M., M. Ruiz-Villarreal, J. Pereira, P. Otero, M. Cirano, X. Zhang, and R. D. Hetland (2013), Efficient tools for marine operational forecast and oil spill tracking, *Marine Pollution Bulletin*, *71*(1-2), 139–151, doi:10.1016/j.marpolbul.2013.03.022.

Mateus, M., G. Riflet, P. Chambel, L. Fernandes, R. Fernandes, M. Juliano, F. Campuzano, H. De Pablo, and R. Neves (2012), An operational model for the West Iberian coast: Products and services, *Ocean Science*, *8*(4), 713–732, doi:10.5194/os-8-713-2012.

Mazé, J. P. (1995), Bilan de volume dans la couche limite Est au large de la Peninsule Ibérique, PhD Thesis, Universite de Bretagne Occidentale, Brest, p. 164.

McClain, C. R., S. Y. Chao, L. P. Atkinson, J. O. Blanton, and F. Decastillejo (1986), Wind-Driven Upwelling in the Vicinity of Cape Finisterre, Spain, *Journal of Geophysical Research-Oceans*, *91*(C7), 8470–8486.

Mendes, R. (2016), The Douro estuarine plume: detection, processes and dynamics, PhD Thesis, Universidade de Aveiro, p. 220.

Mendes, R., M. C. Sousa, M. DeCastro, M. Gómez-Gesteira, and J. M. Dias (2016), New insights into the Western Iberian Buoyant Plume: Interaction between the Douro and Minho River plumes under winter conditions, *Progress in Oceanography*, *141*, 30–43, doi:10.1016/j.pocean.2015.11.006.

Meunier, T., V. Rossi, Y. Morel, and X. Carton (2010), Influence of bottom topography on an upwelling current: Generation of long trapped filaments, *Ocean Modelling*, *35*(4), 277–303, doi:10.1016/j.ocemod.2010.08.004.

Meunier, T., E. D. Barton, B. Barreiro, and R. Torres (2012), Upwelling filaments off Cap Blanc: Interaction of the NW african upwelling current and the Cape Verde frontal zone eddy field?, *Journal of Geophysical Research: Oceans*, *117*(8), 1–18, doi:10.1029/2012JC007905.

Miranda, P. M. A., F. E. S. Coelho, A. R. Tomé, M. A. Valente, A. Carvalho, C. Pires, H. O. Pires, V. C. Pires, and C. Ramalho (2002), 20 th Century Portuguese Climate and Climate Scenarios, *Climate Change in Portugal: Scenarios Impacts and Adaptation Measures (SIAM Project)*, pp. 23–83.

Moita, M. T., P. B. Oliveira, J. C. Mendes, and a. S. Palma (2003), Distribution of chlorophyll a and Gymnodinium catenatum associated with coastal upwelling plumes off central Portugal, *Acta Oecologica*, *24*(SUPPL. 1), 125–132, doi:10.1016/S1146-609X(03)00011-0.

Moita, M. T., Y. Pazos, C. Rocha, R. Nolasco, and P. B. Oliveira (2016), Toward predicting Dinophysis blooms off NW Iberia: A decade of events, *Harmful Algae*, *53*, 17–32, doi:10.1016/j.hal.2015.12.002.

Narimousa, S., and T. Maxworthy (1989), Application of a laboratory model to the interpretation of satellite and field observations of coastal upwelling, *Dynamics of Atmospheres and Oceans*, *13*(1–2), 1–46, doi:10.1016/0377-0265(89)90032-8.

Nencioli, F., C. Dong, T. Dickey, L. Washburn, and J. C. McWilliams (2010), A Vector Geometry Based Eddy Detection Algorithm and Its Application to a High-resolution Numerical Model Product and High-frequency Radar Surface Velocities in the Southern California Bight, *Journal of Atmospheric and Oceanic Technology*, *27*(3), 564–579, doi:10.1175/2009JTECHO725.1.

Nieto, K., H. Demarcq, and S. McClatchie (2012), Mesoscale frontal structures in the Canary Upwelling System: New front and filament detection algorithms applied to spatial and temporal patterns, *Remote Sensing of Environment*, *123*, 339–346, doi:10.1016/j.rse.2012.03.028.

Nieto-Cid, M., X. A. Alvarez-Salgado, S. Brea, and F. F. Perez (2004), Cycling of dissolved and particulate carbohydrates in a coastal upwelling system (NW Iberian Peninsula), *Marine Ecology-Progress Series*, *283*, 39–54.

Nolasco, R., A. C. Pires, N. Cordeiro, B. Le Cann, and J. Dubert (2013a), A high-resolution modeling study of the Western Iberian Margin mean and seasonal upper ocean circulation, *Ocean Dynamics*, *63*(9-10), 1041–1062, doi:10.1007/s10236-013-0647-8.

Nolasco, R., J. Dubert, C. P. Domingues, A. Cordeiro Pires, and H. Queiroga (2013b), Model-derived connectivity patterns along the western Iberian Peninsula: Asymmetrical larval flow and source-sink cell, *Marine Ecology Progress Series*, *485*, 123–142, doi:10.3354/meps10324.

North, G. R., T. L. Bell, R. F. Cahalan, and F. J. Moeng (1982), Sampling Errors in the Estimation of Empirical Orthogonal Funtions, *Monthly Weather Review*, *110*(7), 699–706, doi:10.1175/1520-0493(1982)110<0699:SEITEO>2.0.CO;2.

Nykjær, L., and L. Van Camp (1994), Seasonal and interannual variability of coastal upwelling along northwest Africa and Portugal from 1981 to 1991, *Journal of Geophysical Research*, *99*(C7), 14,197, doi:10.1029/94JC00814.

Oliveira, P. B., R. Nolasco, J. Dubert, T. Moita, and A. Peliz (2009), Surface temperature, chlorophyll and advection patterns during a summer upwelling event off central Portugal, *Continental Shelf Research*, *29*(5-6), 759–774.

Otero, P. (2008), Estudios numéricos de la circulación de otoño e invierno en el Noroeste de la Península Ibérica, PhD Thesis, Universidade de Vigo, p. 193.

Otero, P., M. Ruiz-Villarreal, and A. Peliz (2008), Variability of river plumes off Northwest Iberia in response to wind events, *Journal of Marine Systems*, *72*(1-4), 238–255, doi:10.1016/j.jmarsys.2007.05.016.

Otero, P., M. Ruíz-Villareal, Á. Peliz, and J. M. Cabanas (2010), Climatology and reconstruction of runoff time series in northwest Iberia: influence in the shelf buoyancy budget off Ría de Vigo, *Scientia Marina*, *74*, 247–266.

Otero, P., M. Ruiz-Villarreal, L. García-García, G. González-Nuevo, and J. M. Cabanas (2013), Coastal dynamics off Northwest Iberia during a stormy winter period Topical Collection on Multi-scale modelling of coastal, shelf and global ocean dynamics, *Ocean Dynamics*, *63*(1), 115–129, doi:10.1007/s10236-012-0585-x.

Peliz, Á. (2002), Process Study of Winter Circulation in the Western Iberia Coastal Transition Zone, PhD Thesis, Universidade de Aveiro, p. 153.

Peliz, A., T. L. Rosa, a. M. P. Santos, J. L. Pissarra, Á. Peliz, T. L. Rosa, a. M. P. Santos, and J. L. Pissarra (2002), Fronts, jets, and counter-flows in the Western Iberian upwelling system, *Journal of Marine Systems*, *35*(1-2), 61–77, doi:10.1016/S0924-7963(02)00076-3.

Peliz, A., J. Dubert, D. B. Haidvogel, and B. Le Cann (2003a), Generation and unstable evolution of a density-driven Eastern Poleward Current: The Iberian Poleward Current, *Journal of Geophysical Research-Oceans*, *108*(C8), 3268, doi:10.1029/2002JC001443.

Peliz, A., J. Dubert, and D. B. Haidvogel (2003b), Subinertial response of a density-driven eastern boundary poleward current to wind forcing, *Journal of Physical Oceanography*, *33*(8), 1633–1650.

Peliz, A., J. Dubert, A. M. P. Santos, P. B. Oliveira, and B. Le Cann (2005), Winter upper ocean circulation in the {Western Iberian Basin} - Fronts, Eddies and Poleward Flows: an overview, *Deep-Sea Research Part I-Oceanographic Research Papers*, *52*(4), 621–646, doi:10.1016/j.dsr.2004.11.005.

Peliz, A., J. Dubert, P. Marchesiello, and A. Teles-Machado (2007), Surface circulation in the Gulf of Cadiz: Model and mean flow structure, *Journal of Geophysical Research-Oceans*, *112*(C11015), doi:10.1029/2007jc004159.

Peliz, A., P. Marchesiello, A. M. P. Santos, J. Dubert, A. Teles-Machado, M. Marta-Almeida, and B. Le Cann (2009), Surface circulation in the Gulf of Cadiz: 2. Inflow-outflow coupling and the Gulf of Cadiz slope current, *Journal of Geophysical Research-Oceans*, *114*(C3), doi:10.1029/2008JC004771.

Penven, P., L. Debreu, P. Marchesiello, and J. C. McWilliams (2006), Evaluation and application of the ROMS 1-way embedding procedure to the central California upwelling system, *Ocean Modelling*, *12*(1-2), 157–187, doi:10.1016/j.ocemod.2005.05.002.

Pires, A. C. (2013), Modeling the Western Iberian Margin circulation: present and future, PhD Thesis, Universidade de Aveiro, Portugal, p. 182.

Preisendorfer, R. W. (1988), *Principal Component Analyses in Meteorology and Oceanography*, Elsevier.

Prieto, E. (2014), Deep Ocean Hydrographical Variability and Circulation in the North-West Iberia, PhD Thesis, Universidad de Oviedo, p. 107.

Pringle, J. M. (2002), Enhancement of Wind-Driven Upwelling and Downwelling by Alongshore Bathymetric Variability, *Journal of Physical Oceanography*, *32*(11), 3101–3112, doi:10.1175/1520-0485(2002)032<3101:EOWDUA>2.0.CO;2.

Pringle, J. M., and E. P. Dever (2009), Dynamics of wind-driven upwelling and relaxation between Monterey Bay and Point Arena: Local-, regional-, and gyre-scale controls, *Journal of Geophysical Research: Oceans*, *114*(7), 1–22, doi:10.1029/2008JC005016.

Quaresma, L. S., and A. Pichon (2013), Modelling the barotropic tide along the West-Iberian margin, *Journal of Marine Systems*, *109-110*(SUPPL.), S3–S25, doi:10.1016/j.jmarsys.2011.09.016.

Reboreda, R., N. G. F. Cordeiro, R. Nolasco, C. G. Castro, X. a. Álvarez-Salgado, H. Queiroga, and J. Dubert (2014), Modeling the seasonal and interannual variability (2001-2010) of chlorophyll-a in the Iberian margin, *Journal of Sea Research*, *93*, 133–149, doi:10.1016/j.seares.2014.04.003.

Relvas, P. (1999), The physiscal oceanography of the Cape São Vicente upwelling region observed from sea, land and space, PhD Thesis, Univ. of Wales, Bangor, p. 245.

Relvas, P., and E. D. Barton (2002), Mesoscale patterns in the Cape São Vicente (Iberian Peninsula) upwelling region, *Journal of Geophysical Research*, *107*(C10), 1–23, doi:10.1029/2000JC000456.

Relvas, P., and E. D. Barton (2005), A separated jet and coastal counterflow during upwelling relaxation off Cape São Vicente (Iberian Peninsula), *Continental Shelf Research*, *25*(1), 29–49, doi:10.1016/j.csr.2004.09.006.

Relvas, P., E. D. Barton, J. Dubert, P. B. Oliveira, Á. Peliz, J. C. B. da Silva, and a. M. P. Santos (2007), Physical oceanography of the western Iberia ecosystem: Latest views and challenges, *Progress in Oceanography*, *74*(2-3), 149–173, doi:10.1016/j.pocean.2007.04.021.

Ribeiro, A. C., A. Peliz, and A. M. P. Santos (2005), A study of the response of chlorophyll-a biomass to a winter upwelling event off Western Iberia using SeaWiFS and in situ data, *Journal of Marine Systems*, *53*(1-4), 87–107.

Rios, A. F., F. F. Perez, and F. Fraga (1992), Water Masses in the Upper and Middle North-Atlantic Ocean East of the Azores, *Deep-Sea Research Part a-Oceanographic Research Papers*, *39*(3-4A), 645–658.

Røed, L. P., and X. B. Shi (1999), A numerical study of the dynamics and energetics of cool filaments, jets, and eddies off the Iberian Peninsula, *Journal of Geophysical Research: Oceans*, *104*(Figure 1), 29,817–29,841, doi:10.1029/1999JC900175.

Rossi, V. (2010), Influence of mesoscale physiscal processes on planktonic ecosystems in the regional ocean: application to the Eastern Boundary Upwelling Systems, PhD Thesis, Toulouse, France, p. 286.

Rossi, V., Y. Morel, and V. Garçon (2010), Effect of the wind on the shelf dynamics: Formation of a secondary upwelling along the continental margin, *Ocean Modelling*, *31*(3–4), 51–79, doi:10.1016/j.ocemod.2009.10.002.

Rossi, V., V. Garçon, J. Tassel, J. B. Romagnan, L. Stemmann, F. Jourdin, P. Morin, and Y. Morel (2013), Cross-shelf variability in the Iberian Peninsula Upwelling System: Impact of a mesoscale filament, *Continental Shelf Research*, *59*, 97–114, doi:10.1016/j.csr.2013.04.008.

Ruiz-Villarreal, M., L. M. García-García, M. Cobas, P. A. Díaz, and B. Reguera (2016), Modelling the hydrodynamic conditions associated with Dinophysis blooms in Galicia (NW Spain), *Harmful Algae*, *53*, 40–52, doi:10.1016/j.hal.2015.12.003.

Santos, A. M., A. E. Nieblas, P. Verley, A. Teles-Machado, S. Bonhommeau, C. Lett, S. Garrido, and A. Peliz (2018), Sardine (Sardina pilchardus) larval dispersal in the Iberian upwelling system, using coupled biophysical techniques, *Progress in Oceanography*, *162*(January 2017), 83–97, doi:10.1016/j.pocean.2018.02.011.

Saunders, P. M. (1982), Circulation in the eastern North Atlantic, *Journal of Marine Research*, *40*, 641–657.

Send, U., R. C. Beardsley, and C. D. Winant (1987), Relaxation from upwelling in the Coastal Ocean Dynamics Experiment, *Journal of Geophysical Research*, *92*(C2), 1683, doi:10.1029/JC092iC02p01683.

Serra, N. (2004), Observations and Numerical Modelling of the Mediterranean Outflow, PhD Thesis, University of Lisbon, p. 234.

Serra, N., I. Ambar, and D. Boutov (2010), Surface expression of Mediterranean Water dipoles and their contribution to the shelf/slope – open ocean exchange, *Ocean Science Discussions*, *6*(3), 2579–2623, doi:10.5194/osd-6-2579-2009.

Shchepetkin, A. F. (2003), A method for computing horizontal pressure-gradient force in an oceanic model with a nonaligned vertical coordinate, *Journal of Geophysical Research*, *108*(C3), doi:10.1029/2001JC001047.

Shchepetkin, A. F., and J. C. McWilliams (2005), The regional oceanic modeling system (ROMS): a split-explicit, free-surface, topography-following-coordinate oceanic model, *Ocean Modelling*, *9*(4), 347–404, doi:10.1016/j.ocemod.2004.08.002.

Sibuet, J. C., S. Monti, B. Loubrieu, J. P. Maze, and S. Srivastava (2004), Carte bathymétrique de l'Atlantique nord-est et du Golfe de Gascogne: implications cinématiques, *Bulletin de la Société Géologique de France*, *175*(5), 429–442.

Simmons, A. J., S. M. Uppala, D. P. Dee, and S. Kobayashi (2007), ERA-Interim: New ECMWF reanalysis products from 1989 onwards, *ECMWF Newsletter*, *110*(110), 25–35, doi:ECMWFNewslettern.110.

Sordo, I., E. D. Barton, J. M. Cotos, and Y. Pazos (2001), An Inshore Poleward Current in the NW of the Iberian Peninsula Detected from Satellite Images, and its Relation withG. catenatum and D. acuminata Blooms in the Galician Rias, *Estuarine, Coastal and Shelf Science*, *53*(6), 787–799, doi:10.1006/ecss.2000.0788.

Sousa, F. M. (1995), Processos de Mesoescala ao Largo da Costa Portuguesa Utilizando Dados de Satélite e Observações In Situ, PhD Thesis, University of Lisbon, p. 167.

Sousa, M. C. (2013), Modelling the Minho River plume intrusion into the Rias Baixas, PhD Thesis, Universidade do Porto, p. 136.

Sousa, M. C., R. Mendes, I. Alvarez, N. Vaz, M. Gomez-Gesteira, and J. M. Dias (2014), Unusual Circulation Patterns of the Rias Baixas Induced by Minho Freshwater Intrusion (NW of the Iberian Peninsula), *PLoS ONE*, *9*(11), doi:10.1371/journal.pone.0112587.

Strub, P. T., P. M. Kosro, and A. Huyer (1991), The Nature of the Cold Filaments in the California Current System, *Journal of Geophysical Research*, *96*, 14,743–14,768.

Tanner, S. E., A. Teles-Machado, F. Martinho, Á. Peliz, and H. N. Cabral (2017), Modelling larval dispersal dynamics of common sole (Solea solea) along the western Iberian coast, *Progress in Oceanography*, *156*, doi:10.1016/j.pocean.2017.06.005.

Taylor, K. E. (2001), Summarizing multiple aspects of model performance in a single diagram, *Journal of Geophysical Research*, *106*(D7), 7183–7192.

Teles-Machado, A. (2014), Dynamics and Variability of the Alongshore Flows on the Northwestern Iberian Margin, PhD Thesis, Universidade de Lisboa, p. 139.

Teles-Machado, A., Á. Peliz, J. C. Mcwilliams, R. M. Cardoso, P. M. M. Soares, and P. M. A. Miranda (2015), On the year-to-year changes of the Iberian Poleward Current, *Journal of Geophysical Research : Oceans*, *120*, doi:10.1002/2015JC010758.

Teles-Machado, A., Á. Peliz, J. C. McWilliams, X. Couvelard, and I. Ambar (2016), Circulation on the Northwestern Iberian Margin: Vertical structure and seasonality of the alongshore flows, *Progress in Oceanography*, *140*(January), 134–153, doi:10.1016/j.pocean.2015.05.021.

Tilstone, G. H., F. G. Figueiras, L. M. Lorenzo, and B. Arbones (2003), Phytoplankton composition, photosynthesis and primary production during different hydrographic conditions at the Northwest Iberian upwelling system, *Marine Ecology Progress Series*, *252*, 89–104, doi:10.3354/meps252089.

Torres, R., and E. D. Barton (2006), Onset and development of the Iberian poleward flow along the Galician coast, *Continental Shelf Research*, *26*(10), 1134–1153, doi:10.1016/j.csr.2006.03.009.

Torres, R., and E. D. Barton (2007), Onset of the Iberian upwelling along the Galician coast, *Continental Shelf Research*, *27*(13), 1759–1778, doi:10.1016/j.csr.2007.02.005.

Torres, R., E. D. Barton, P. Miller, and E. Fanjul (2003), Spatial patterns of wind and sea surface temperature in the Galician upwelling region, *Journal of Geophysical Research*, *108 (C4)*, 3130.

Troupin, C., E. Mason, J. M. Beckers, and P. Sagrá (2012), Generation of the Cape Ghir upwelling filament: A numerical study, *Ocean Modelling*, *41*, 1–15.

Valdés, L., A. Lavín, M. L. Fernández de Puelles, M. Varela, R. Anadón, A. Miranda, J. Camiñas, and J. Mas (2002), Spanish ocean observation system. IEO core project: Studies on time series of oceanographic data, in *Operational Oceanography: Implementation at the European and Regional Scales.*, vol. 66, edited by N. Fleming, S. Vallerga, N. Pinardi, H. Behrens, G. Manzella, D. Prandle, and J. Stel, pp. 99–105, Elsevier Oceanography Series, doi:10.1016/S0422-9894(02)80014-9.

Varela, R. A., G. Roson, J. L. Herrera, S. Torres-Lopez, and A. Fernandez-Romero (2005), A general view of the hydrographic and dynamical patterns of the Rias Baixas adjacent sea area, *Journal of Marine Systems*, *54* (1-4), 97–113.

Veitch, J., P. Penven, and F. Shillington (2010), Modeling Equilibrium Dynamics of the Benguela Current System, *Journal of Physical Oceanography*, *40*(9), 1942–1964, doi: 10.1175/2010JPO4382.1.

Visbeck, M. (2002), Deep velocity profiling using lowered acoustic Doppler current profilers: Bottom track and inverse solutions, *Journal of Atmospheric and Oceanic Technology*, *19*(5), 794–807, doi:10.1175/1520-0426(2002)019<0794:DVPULA>2.0.CO;2.

Vitorino, J., a. Oliveira, J. M. Jouanneau, and T. Drago (2002), Winter dynamics on the northern portuguese shelf. Part 1: Physical processes, *Progress in Oceanography*, *52*(2-4), 129–153, doi:10.1016/S0079-6611(02)00003-4.

Washburn, L., M. R. Fewings, C. Melton, and C. Gotschalk (2011), The propagating response of coastal circulation due to wind relaxations along the central California coast, *Journal of Geophysical Research*, *116*(12), 1–16, doi:10.1029/2011JC007502.

Wooster, W. S., A. Bakun, and D. R. Mclain (1976), Seasonal Upwelling Cycle Along the Eastern Boundary of the North-Atlantic, *Journal of Marine Research*, *34* (2), 131–141.